Elastocapillary Self-folding of Micro-machined Structures

Capillary Origami

The graduation committee

Prof. dr. Peter M.G. Apers	University of Twente (chairman and secretary)
Prof. dr. ir. Leon Abelmann	University of Twente (promotor)
Dr. ir. Niels R. Tas	University of Twente (assistant promotor)
Prof. dr. Jurriaan Schmitz	University of Twente
Prof. dr. Jan C.T. Eijkel	University of Twente
Prof. dr. ir. Fred van Keulen	Delft University of Technology
Dr. ir. José Bico	ESPCI, Paris, France

Paranymphs

Dr. Jean-Philippe Frimat
Susan Janse

UNIVERSITY OF TWENTE.

MESA+
INSTITUTE FOR NANOTECHNOLOGY

The research described in this dissertation was carried out at the Transducers Science and Technology group, part of MESA+ institute for Nanotechnology at the University of Twente, Enschede, the Netherlands.

Printed by Gildeprint Drukkerijen, Enschede, the Netherlands

Electronic mail address: a.b.h.legrain@utwente.nl

ISBN 978-90-365-3759-9
DOI 10.3990/1.9789036537599

Elastocapillary Self-folding of Micro-machined Structures
Capillary Origami

DISSERTATION

to obtain
the degree of doctor at the University of Twente,
on the authority of the rector magnificus,
prof. dr. H. Brinksma,
on account of the decision of the graduation committee,
to be publicly defended
on Thursday, 13 November 2014 at 16:45

by

Antoine Bernard Henri Legrain

born on 9 February, 1988
in Vire, France

This dissertation is approved by

Prof. dr. ir. Leon Abelmann	University of Twente (promotor)
Dr. ir. Niels R. Tas	University of Twente (assistant promotor)

Abstract

Standard lithographic techniques have proven to be inadequate at machining true 3D micro-structures - structures with similar dimensions in all directions or with large height to width ratio. New fabrication paradigms are necessary. Combining the assets of mask-based techniques with self-assembly, self-folding is a proven and still promising approach to bring micro-structures to the third dimension. Pre-tethered parts are assembled using an external stimuli such as magnetic forces, pre-stressed layers, thermal shrinking... The work presented in this thesis deals with the self-folding of micro-machined three-dimensional silicon nitride structures using the surface tension of water, method termed elastocapillary folding or capillary origami.

A technique for the controllable capillary folding of 3D micro-structures by means of through-wafer liquid application was developed. For the first time hydro-mechanical, repeatable, actuation of capillary folded structures via the addition or retraction of water on demand has been demonstrated. Silicon nitride objects made of thick flaps inter-connected by flexible hinges were machined with a central through-wafer tube and connected to a dedicated pumping system to enable assembly. When remaining wetted, structures can be assembled and reopened up to several dozens of times and still reach the same final folding angle. Objects were actuated up to 60 times without signs of wear. Extracted curves from the self-folding experiments are in agreement with a two-dimensional elastocapillary folding model. When structures are allowed to dry in between foldings, an increase in the bending stiffness of the hinges is observed, by a factor 50 % after first folding and subsequent drying. This stiffening causes a decrease of the finally achieved angle. Residue from the fabrication process found on the structures after folding is suspected to be the cause of the stiffening.

Using the same type of structures, Platinum electrodes running from the substrate to the plates via the bendable hinges were introduced. The fabrication yield was as high as (77 ± 2) % for hinges with a length less than 75 µm. The yield reduced to (18 ± 2) % when the length increased above 100 µm. Most of the failures in conductivity were due to evaporation of metal during the plasma cleaning step at the end of the fabrication. The bi-layer hinges survived the capillary folding process, even for extremely small bending radii of 5 µm, nor does the bending have any impact on the conductivity. Once assembled, the conductive hinges can withstand a current density of $(1.6 \pm 0.4) \times 10^6$ A/cm^2. Stress in the different layers caused apparent deformation of the hinges. This introduction of conductive electrodes to elastocapillary self-folded silicon based micro-objects extends the range of possible applications by allowing electronic functionality on the folded parts.

Elastocapillary folding of silicon nitride objects with accurate folding angle

between flaps of $(70.6 \pm 0.1)°$ was shown and the feasibility of such accurate micro-assembly with a final folding angle of 90° was demonstrated. The folding angle is defined by stop-programmable hinges that are fabricated starting from silicon molds thanks to accurate three-dimensional corner lithography. This nano-patterning method exploits the conformal deposition and the subsequent timed isotropic etching of a thin film in a 3D shaped silicon template. The technique leaves a residue of the thin film in sharp concave corners which can be used as an inversion mask in subsequent steps. Hinges designed to stop folding at 70.6° were fabricated batch-wise by machining V-grooves obtained by KOH etching in (110) silicon wafers ; 90° stop-programmable hinges were obtained starting from silicon molds obtained by dry etching on (100) wafers. The technique we present here is applicable to any folding angles. It opens a new route towards creating structures with increased complexity, which will ultimately lead to a novel method for device fabrication.

The assembly of side by side ribbons under the action of surface forces was demonstrated. The beams - which are anchored on both sides - rotate and bend to form a highly symmetric three dimensional structures with a central joined part and two opposite opened parts. Wafer-scale assembly of silicon nitride beams was demonstrated and control experiments with macro-sized mylar ribbons were carried out. A model that connects ribbons dimensions, pulling tension and surface forces was developed and compared to the experiments at both scales. The found opening length is conformed to the macro-experiments and is found to be linear with the width of the beams, the separation between them and more than proportional to the applied tension. The opening is independent of the ribbons length. For micro-ribbons, the induced stress by deformation cause the opening length to increase with the width and the separation and to decrease with the length. The theoretical model does not represent the trends well, probably because it does not capture the 3D aspects of the assembly.

Samenvatting

Microtechnologie heeft ons leven ingrijpend veranderd. Dat geldt niet alleen voor geminiaturiseerde electronica (computers) maar ook voor mechanica. Succesvolle voorbeelden zijn de airbag sensor in auto's, of de accelerometer in smartphones. De microtechnologie die we nu gebruiken is echter sterk tweedimensionaal. Alles gebeurt in een uiterst dun laagje op een silicum of glas drager. Het zou een enorme stap vooruit zijn als we ook in de microwereld in drie dimensies kunnen ontwerpen. Zo kunnen we bijvoorbeeld veel meer transistors in een behuizing onderbrengen, zodat we meer geheugen of snellere processors krijgen. Naast electronica kunnen we dan ook drie-dimensionale mechanische objecten uit de macro-wereld miniaturiseren.

Een van de meest elegante manieren om drie-dimensionale structuren te maken is door te vouwen. Het summum van die techniek is de Japanse vouwkunst *origami*. Op de microschaal kunnen we natuurlijk niet met onze vingers vouwen, en zijn truuks nodig. We kunnen bijvoorbeeld electrische of magnetische krachten gebruiken, laagjes met ingebouwde spanningen of de oppervlaktespanning van vloeistoffen. In dit proefschrift gebruiken we de laatste techniek door kleine druppels water te laten verdampen. De druppels worden aangebracht op flexibele structuren, die daardoor samenvouwen. Als we het goed ontwerpen, blijft na verdampen de structuur gevouwen doordat onderdelen tegen elkaar blijven plakken.

De meest eenvoudige methode om kleine druppels aan te brengen is met een holle injectienaald. Die methode is minder geschikt voor massa-productie. Daarom hebben we onderzocht of het mogelijk is om de druppel door een klein kanaaltje aan de achterkant van de te vouwen structuur te persen. Dit is gelukt, alhoewel het massaal vouwen van duizenden structuren tegelijkertijd nog ver weg is.

Bij het vouwen van drie-dimensionale structuren, moeten we voorkomen dat de structuren helemaal plat vouwen. Dat kan eenvoudig door de volgorde van vouwen goed te kiezen, of door speciale aanslagen te gebruiken. In dit proefschrift laten we van de laatste techniek verschillende voorbeelden zien. Aanslagen hebben als voordeel dat we fragiele structuren ver boven het oppervlak van de drager kunnen tillen, met een nauwkeurig gedefinieerde hoek.

Gevouwen mechanische structuren zijn op zich interessant, maar hebben een beperkte toepassing. Daarom hebben we in dit proefschrift onderzocht of we electrische verbindingen kunnen maken naar de beweegbare delen. Dat kan als de verbindingen goed zijn ontworpen, en het blijkt dat die verbindingen niet lijden onder het vouwen.

Voor massaproductie is het noodzakelijk dat structuren met duizenden tegelijkertijd gevouwen kunnen worden. In dit proefschrift laten we zien dat dit lukt met kleine linten. Door het complete substraat onder te dompelen

in water en te laten drogen, kunnen we alle structuren in een keer vouwen. We denken dat het mogelijk is op dezelfde manier complexere structuren te vouwen, maar dit vergt nog veel vervolgonderzoek.

Het werk in dit proefschrift toont overtuigend aan dat microstructuren gevouwen kunnen vouwen door gebruik te maken van oppervlaktespanning. Deze techniek kan de basis zijn van een nieuwe drie-dimensionale productietechniek die de beperkingen van de huidige twee-dimensionale microtechniek achter zich laat.

Résumé

Auto-pliage élastocapillaire de structures micro-fabriquées

Origami Capillaire

La micro-technologie est partout dans notre vie. Téléphones, ordinateurs, minuscules clés USB mais aussi airbags, GPS, pacemakers sont autant d'exemples de technologies qui ont profité de la miniaturisation des composants fabriqués en salle blanche. Malgré des résultats impressionnants, la microfabrication est cependant cantonnée à fabriquer des objets en deux dimensions. Les puces sont fabriquées sur des très fines galettes de silicium qui ne permettent pas de fabriquer d'objets en trois dimensions. Sur les bases actuelles, la miniaturisation aura d'ici dix ou vingt ans atteint ses limites. Afin de dépasser ce stade, la nécessité d'inventer de nouvelles techniques de fabrication s'avère incontournable. Si nous parvenons à fabriquer des objets en trois dimensions à de très faibles échelles, alors nous pourrons continuer à améliorer nos appareils électroniques et pourquoi pas faire progresser des instruments de précision, tels les outils chirurgicaux, vers un monde beaucoup plus miniaturisé.

Il ne s'agit cependant pas de tout réinventer, mais d'utiliser certaines techniques déjà existantes et incontournables. Origami, l'art Japonais de pliage, est peut-être la manière la plus simple et élégante de faire émerger une forme en trois-dimensions à partir d'une feuille de papier en deux-dimensions. Dans cette thèse, nous proposons d'utiliser ce simple concept en combinaison avec les techniques bien connues de micro-fabrication pour fabriquer des objets microscopiques en trois dimensions. Il est évidemment impossible de plier manuellement de si petites structures, l'usage d'une force extérieure est nécessaire. Nous parlons alors d'auto-pliage : des matériaux intelligents sont "programmés" pour se plier sans interventions humaines. Des exemples d'auto-pliage, qui utilisent les forces magnétiques, existent par exemple. La manière avec laquelle les protéines s'assemblent naturellement est aussi proche de l'auto-pliage. Dans cette thèse, nous proposons d'utiliser les forces capillaires, ces mêmes forces qui font que les cheveux collent entre eux à la sortie de la douche ou qui permettent à la sève de monter dans les arbres, pour plier des matériaux micro-fabriqués : l'origami capillaire.

Plus facile à dire qu'à réaliser. Le concept est relativement nouveau et beaucoup d'interrogations subsistent. Comment délivrer l'eau nécessaires au pliage ? Comment s'assurer de la forme finale de l'objet en trois dimensions ? Quel est le coût de fabrication ? Quelles applications pour de telles structures ?

Le travail présenté dans cette thèse vise à apporter des éléments de réponse à ces questions.

Déposer manuellement une goutte d'eau est la méthode la plus simple, mais loin d'être la plus adaptée. Il est alors impossible de plier plusieurs structures simultanément ou de les déplier. Nous avons alors fabriqué et étudié des objets avec un tube central via lequel l'eau est pompée et permet d'actionner l'auto-pliage. Cette technique nous permet de plier et déplier les structures à souhait, mais une recherche plus poussée s'avère nécessaire pour permettre le pliage en masse.

Les objets pliés restent fermés après pliage grâce aux parties qui se touchent et adhérent entre elles, une conséquence des petites dimensions. Sans contact avec une autre partie, il est impossible que le pliage s'arrête. Pour résoudre ce problème nous avons développé la micro-fabrication de charnières intelligentes. Ces charnières permettent de sélectionner l'angle auquel les objets terminent leur pliage.

En termes d'applications, il est primordial que l'électronique puisse être intégrés dans les objets que nous plions. Pour cela, nous avons développé des structures avec des charnières métalliques. Ces charnières ne souffrent pas du pliage et un courant électrique peut y circuler. Elles représentent une première étape nécessaire vers l'électronique en trois dimensions.

Enfin, nous nous sommes intéressés à l'auto pliage de rubans microscopiques. Pour ceux-ci, la fabrication et l'assemblage sont très simples : plongez les rubans dans l'eau, laissez sécher et les milliers de rubans s'assemblent en trois dimensions. Nous avons démontré et quantifié le principe, des applications pourraient suivre.

Les résultats présentés dans cette thèse prouvent que l'origami capillaire présente une technique nouvelle et adaptée pour la fabrication en trois dimension d'objets micro-fabriqués, opération impossible avec les techniques actuelles. Le caractère novateur de cette recherche nous donne espoir de voir de nombreuses applications relatives à ce domaines apparaître dans un futur proche.

Contents

1 Introduction

1.1 3D micro-fabrication: top-down machining limitations

This thesis is about the fabrication of three-dimensional (3D) micro-structures: structures whose lengths in all directions are similar, or with large height to width ratio. Three dimensional fabrication at the human scale is commonplace, but as the dimensions decrease, handling of building parts becomes challenging and finally even impossible. Stacking of parts, milling or screwing are processes that can hardly be transposed to the sub-millimeter scale, or at enormous price. The "most expensive dice in the world", made of brass with 300 µm long edges, is an example of extreme miniaturization of milling [1]. Each tiny dice however takes hours to fabricate and costs as much as 800 $: although impressive, the technique is clearly not economically viable. Advances in microscopy technology now enables the handling of micro/nano parts such as micro-spheres or similar structures [2], or cutting nano-tubes [3]. These accurate techniques are necessarily localized and therefore limited to niche applications. As structure sizes continue to decrease, new paradigms of 3D micro-fabrication are necessary such as micro-machining.

1.2 Micro-machining

Pushed by the semiconductor industry, lithography-based fabrication techniques now include new methods other than UV illumination: mask-less projection of laser light, electrons and ions beams, etc. Extremely precise, these methods are nevertheless inherently 2D. They essentially consist on patterning one single layer after the other. Precise 3D shapes can be obtained using anisotropic etching of silicon, but they are constrained in depth or height because of a limited substrate thickness. Consequently, high aspect-ratio structures are difficult to fabricate using techniques based on lithography and etching [4, 5].

Stacking or bonding of wafers is a way to overcome these limitations [6], but fabrication remains time-consuming and complex. X-Ray LIGA (German acronym for Lithography, Electroplating and Molding) was developed for the

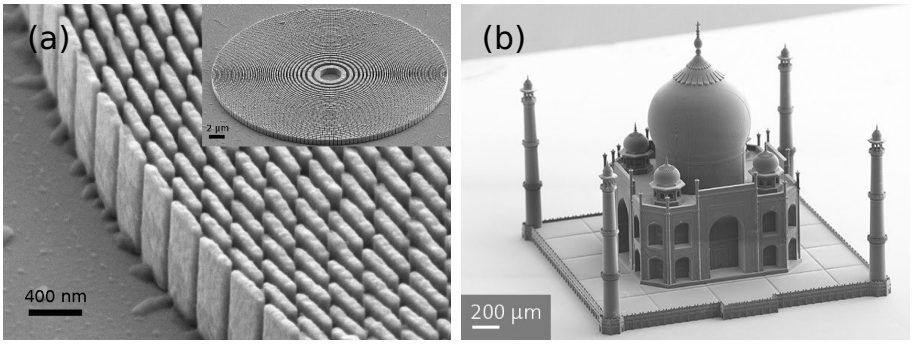

Figure 1.1 – Examples of 3D micro-machining techniques. (a): Gold structures, electroplated in a PMMA mold obtained by the X-Ray LIGA process (from Paul Scherrer Institut, Switzerland). The technique offers high aspect-ratio and nanometer resolution, but lacks the possibility for vertical patterning. (b): Fine replica of the Taj-Mahal made by 3D micro-printing (from Nanoscribe GmBH, Germany).

fabrication of structures with aspect ratios in the order of 100:1 [7]. This technique requires a synchotron X-ray source and is therefore not readily accessible. Its cousin, UV-LIGA in combination with thick photoresists like SU-8, is more available. In combination with dry etching techniques (Deep Reactive Ion Etching in particular), this method can yield structures with aspect ratio up to 50:1. However, substrate thickness limitations cannot be overcome, and patterning of vertical sidewalls is impossible as shown in Figure 1.1.

Micro-fabrication techniques exist that do not require masks, but directly fabricate the layers instead. Three dimensional micro-printing (two-photon polymerization) is a trendy technique, promising for 3D fabrication at small scales with breathtaking resolution and speed [8, 9]. Still at its infancy, efforts are now made to extend the versatility of the technique with the development of new printable materials and applications, such as 3D batteries [10] or biomaterials [11].

There are many more micro-machining techniques that allow pseudo 3D fabrication. Electron beam (EB) and focused ion beam (FIB) lithographies use particles beams that are focused on sensitive substrates and can achieve nm resolutions [12]. Coupled with chemical vapor deposition, these two techniques allow the deposition of solid residues with identical resolution (EB-CVD, FIB-CVD) [13]. UV laser writing is capable of direct fabrication of 3D suspended structures [14]. Beyond these few, many more examples exist. All these methods have their pros and cons. A comprehensive review of these methods is

offered by Gracias *et al.* [5]. Despite the demonstrated ability to fabricate 3D-patterned objects, these lithographic methods are in general still serial, time consuming and usually inadequate for mass production. They are often used to create master templates that are subsequently used to mass-produce daughter structures, in order to reduce fabrication time. However, mostly polymers, such as PDMS, can be printed this way. Applications are therefore limited, and vertical patterning is still complicated.

1.3 From self-assembly to self-folding

An approach opposite to top-down fabrication is to use bottom-up self assembly. Self-assembly is the process by which order emerges from a set of disordered components. Everything in nature, from galaxies to salts and cells, is self-assembled with astonishing efficiency and accuracy. In recent years self-assembly has became a huge trend in the scientific community. Researchers dream of reproducing in the laboratory what nature has spontaneously done for billions of years. Particles in a colloidal solution are made to assemble as the solvent evaporates in a organized fashion dictated by van der Waals forces for example. 3D photonic crystals structures have been made this way [15]. DNA folding is another example of highly controllable self-assembly process [16].

A higher degree of complexity can be achieved using "smart" components. Magnetic force, surface tension or chemical bondings are used to increase intricacy of self-assembled structures. Nevertheless, such engineered components suffer from a high level of uncertainty. Interactions between driving forces and components are still under investigation and not yet fully understood. Parasitic outcomes of such complicated systems decrease the yield of desired structures.

The idea around self-folding is to combine the assets of micro-machining and self-assembly: using the accuracy and determinism of lithographic techniques together with the ease and versatility of self-assembly. That is, to self-assemble linked components obtained by lithographic techniques in order to greatly increase the control of possible outcomes. Many methods have been used to enable self-folding of 3D micro-structures and are well described in recent reviews [5, 21–23]. They mainly include magnetic forces, shrinking of polymers, thermal and shape memory alloy actuation, stressed thin films, and surface forces. Figure 1.2 gives a few examples of self-folded micro-structures.

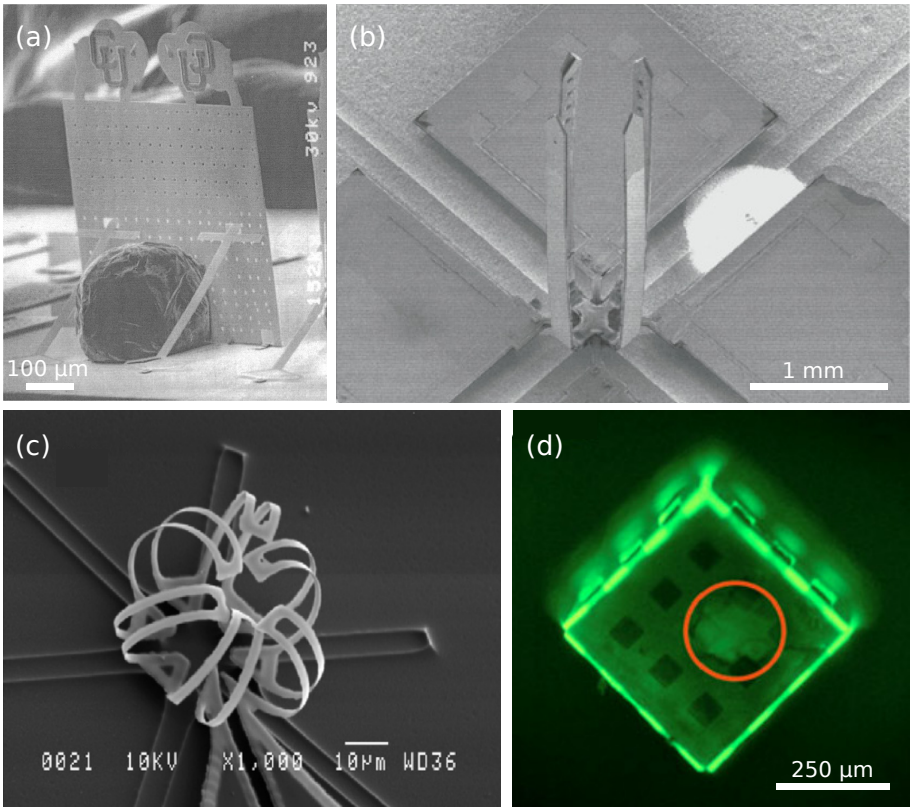

Figure 1.2 – Example of self-folded structures. (a): Polysilicon plate folded under the surface tension of melting solder [17]. (b): Micro-electrode array folded by polymer shrinking [18]. (c): Stress-based folding of a SU8/DLC micro-cage. The cage can be actuated by temperature variation [19]. (d): Fluorescence image of *Artemia* eggs (orange circle) encapsulated in a porous polymeric cube [20].

Surface forces are probably the most researched self-folding method. Liquids tend to reduce their surfaces to minimize their interfacial energy, resulting in a force called surface tension. Surface forces become predominant over bulk forces at small scales, making them a perfect candidate for 3D self-folding at millimeter scales and below. Py *et al.* elegantly described the concept of "capillary origami" (also termed elastocapillary folding) by folding millimeter PDMS sheets by simply depositing water on top of them [24]. In the micrometer world, Syms was the first to self-fold with the surface tension of melting solders to assemble 3D micro-opto-electromechanical systems (MOEMS) more than a decade ago [25]. The concept was then greatly enhanced by Gracias *et al.* with the folding of nm containers with patterned faces [26, 27]. The work

presented here is about scaling down the concept of "capillary origami": the self-folding of micro-meter structures using the surface tension of water.

1.4 Origami at all scales

From the Japanese "ori" (folded) and "gami" (paper), origami designates the folding of initially flat surfaces into three-dimensional shapes through bending only. First developed as an art, it is nowadays widely used as a engineering tool at all scales [28]. Many industrial objects are made by bending flat metal and plastic plates, deployable solar panels or lenses are launched into space and foldable robots were recently developed. Figure 1.3 gives a few examples of folded objects. Mathematicians have shown that countless numbers of shapes can be obtained by origami. Fabrication by folding has many advantages for engineering applications such as compact storage of deployable structures, active reconfiguration and reduction in manufacturing complexity.

For certain situations it is impractical to directly execute the mechanical work necessary for bending. This is especially true for micro-structures. In this case self-folding becomes essential. The folding operation is achieved via application of a non-mechanical actuation (electrical, magnetic, thermal, elastocapillary...) on active materials capable of converting these forces into mechanical work.

Capillary origami at micrometer scales is a relatively new concept, and this thesis aims at gaining insights about the technique by investigating the self-folding of silicon nitride objects. Ultimately, we wish to bring parts of an answer to the following question: can the elastocapillary folding of silicon-based micro-structures become a viable option for the future of 3D micro-fabrication?

1.5 Thesis outline

Actuation and batch folding of structures are desirable features of micro-machined self-folded 3D structures. In chapter 2 we present a technique for the controllable capillary folding of silicon nitride templates into 3D micro-structures. Pseudo two-dimensional long extruded objects with a central through-wafer tube are connected to a dedicated pumping system to enable assembly. After a theoretical part where an energy-minimization based 2D model is presented, the fabrication is described and the self-folding experi-

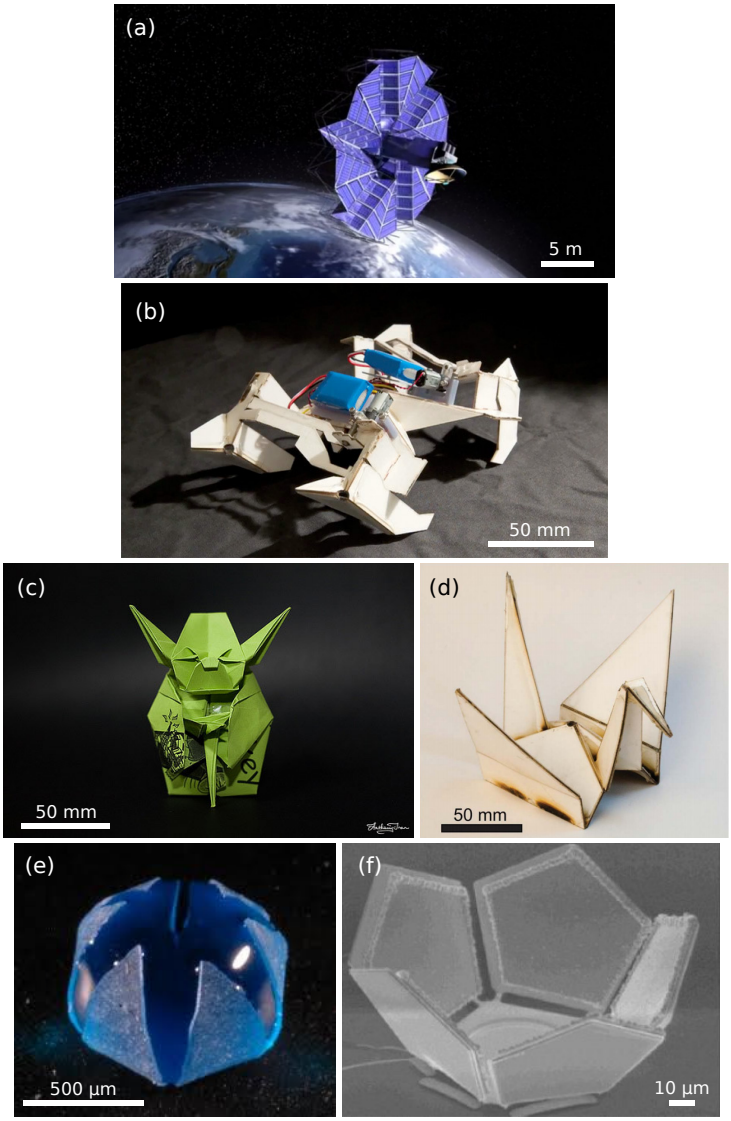

Figure 1.3 – Origami at all scales. (a): Origami inspired solar array under development. When deployed, it will expand ten times its stored size [29]. (b): Origami robot. Initially flat, the robot uses shape memory polymers that contract like muscles when heated [30]. (c): Artistic origami in its traditional meaning. Designed and folded by *Antzpantz*. (d): This crane is self-folded using shape memory polymers [31]. (e): Capillary origami. This PDMS sheet spontaneously folds when in contact with water [24]. (f): Micro-scale origami. The polysilicon flaps, coated with permalloy, are self-folded by an external magnetic field [32].

mental results are compared to the theory. Finally, the use of such through-wafer filling for batch folding is discussed.

In chapter 3 we introduce the fabrication of bi-layer conductive hinges that would allow self-folding of functional micro-objects. Using similar structures as in chapter 2 but manually depositing water, Platinum electrodes are running from the substrate to the plates via the bendable hinges. The fabrication yield, encountered stress mismatch issues between the layers and assembly are discussed.

The deformation of silicon nitride hinges is deliberately limited to the elastic regime during assembly. In consequence the final shape of 3D objects is determined by parts that meet and adhere while folding. Chapter 4 includes the fabrication procedure of stop programmable hinges that stop bending at well-defined angles. Using the nano-patterning technique known as corner lithography, we extensively describe the fabrication of these complex hinges and present the self-folding of resulting structures.

The next chapter presents a simple and batch form of elastocapillary folding with twisting ribbons. Two ribbons next to each other rotate, bend and adhere under the action of surface forces. We describe experiments carried out wafer scale with silicon nitride micro-ribbons as well as control macroscopic experiments done with mylar ribbons. A theoretical model is presented and compared to our results at both scales.

Finally, chapter 6 includes the conclusion and outlook of this thesis.

2

Controllable elastocapillary folding of 3D micro-objects by through-wafer filling

2.1 Introduction

2.1.1 Self-folding of silicon-based micro-structures

The continuous demand for smaller functional elements in micro-technology makes it essential to use all three spatial dimensions effectively. By combining the assets of mask-based fabrication and self-assembly, self-folding is a promising approach to reach the third dimension. The use of surface forces is a powerful technique to enable self-folding [5, 21–23].

The idea of silicon-based micro-structures self-folding originated two decades ago with Syms who suggested that the surface tension of melting solder could become a viable option to produce quasi-three-dimensional (3D) micro-objects [33]. Since the idea became technique and applications have been demonstrated such as out-of-plane 3D MOEMS (Micro-Opto-Electro Mechanical Systems), using melting solder as well as melting photoresist [17, 25, 34–37].

Solder assembly was also used by Gracias *et al.* who demonstrated the folding of complex structures (cubes, pyramids...) of micrometer and nanometer sizes by using standard lithography and deposition techniques [26, 27, 38, 39]. Such structures do not require hinges, as was demonstrated by Syms [40, 41], and the final achieved folding angle can either be tuned by choosing the amount of solder material [33, 38, 41] or by designing the structures such that the different parts meet during assembly and lock in [26, 34, 39, 41].

Others techniques enabling self-folding of silicon-based materials have been demonstrated, for example using the intrinsic stress of thin films [42, 43] or magnetic interactions [32, 44, 45]. It is worth nothing that nowadays self-folding of thin film materials is neither limited to previous mentioned

Published as: A. Legrain, T. G. Janson, J. W. Berenschot, L. Abelmann, and N. R. Tas, "Controllable elastocapillary folding of three-dimensional micro-objects by through-wafer filling", *Journal of Applied Physics* **115**, 214905 (2014)

techniques nor to silicon-based materials, but includes a variety of different methods at different scales from bio-inspired assembly to graphene origami with applications in many domains. For a state of the art reviews please refer to citations [5, 21–23].

2.1.2 Elastocapillary self-folding

Elastocapillary phenomena refer to the deformation of objects as a result of capillary effects of liquid droplets or films [46, 47]. The final deformation is governed by the balance between bending and capillary forces. It is helpful to define an elastocapillary length, $L_{ec} = (B/\gamma)^{1/2}$ where B is the bending stiffness [Nm] and γ the surface tension [N/m]. Typically, objects longer than the elastocapillary length are significantly deformed by capillary forces [24, 48]. Bico *et al.* offered an elegant demonstration of how elastocapillary interaction could be used to self-fold millimeter PDMS objects [24, 46, 48]. Also in the macroscopic world, the use of elastocapillary self-folded thin silicon sheets for photovoltaic cells was described [49]. More recently, the conditions for macroscopic droplets wrapping were studied [50] as well as the selection for folded structures using drop impact [51] and interactions with superhydrophobic surfaces [52].

Inspired by previously cited works, we have combined elastocapillary interactions with micro-machining to fabricate 3D silicon nitride micro-objects, starting from flat patterns. Structures made of rigid plates connected to each others by flexible elastic hinges made of the same material are self-folded into three-dimensional micro-objects using the surface tension of water – a method we term elastocapillary folding or capillary origami [53, 54]. The final achieved folding angle is either a function of initial mask design [53] or is determined by micro-machining of stop-programmable hinges [54]. This technique allows the assembly of accurate micro-objects similar to those obtained with solder assembly [26]. Moreover, it relies only on the surface tension of the applied liquid and on wetting, and therefore represents a viable alternative to solder assembly.

2.1.3 Hydro-mechanical actuation

In our previous work on elastocapillary folding, we manually deposited a droplet on the silicon nitride structures [53, 54]. This technique suffers from several disadvantages, such as difficulty in droplet application and a lack of

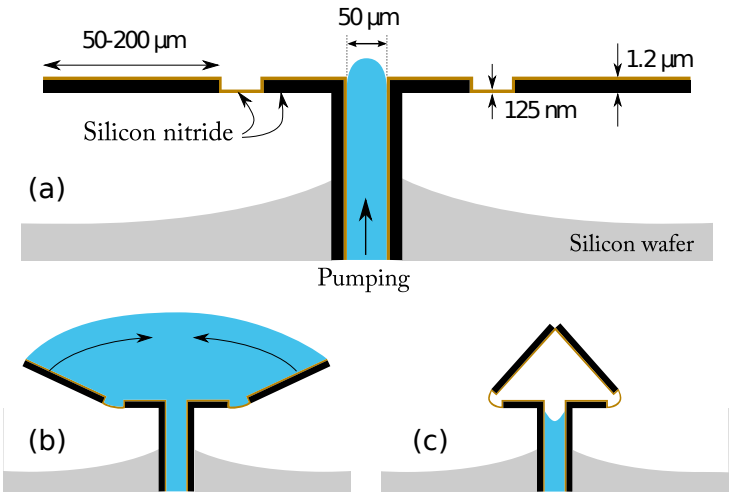

Figure 2.1 – Sketch of folding principle. (a): Water is pumped through the wafer via the central tube. The liquid flows over the silicon nitride structure and pumping is stopped. (b): The water, the contact line of which is pinned at the edge of the structure, tends to reduce its liquid-air interface and provokes the rotation of the flaps through the bending of the thin hinges. The volume of liquid decreases either by evaporation or by deliberate retraction. (c): Once the water has gone, the flaps adhere.

control over the applied volume. Moreover, the structures can be folded only once, which considerably limits their potential applications.

Although the actuation of self-folded structures by pH triggering or temperature variation has been reported (see for instance the review by Leong *et al.* [5]), not much work has been done on elastocapillary folded structures [47]. At the macro-scale, elegant control of folding by an electric field has been demonstrated [55, 56], but this method is difficult to apply to micrometer structures in which the integration of electrodes and the control of small volumes of water remain complicated.

In this paper, we present the first demonstration of folding by through-wafer filling. This technique, presented schematically in Figure 2.1, enables the three-dimensional hydro-mechanical actuation of micro-structures. Along with the technical details of the fabrication and experiments, an analytical study of the folding process is presented.

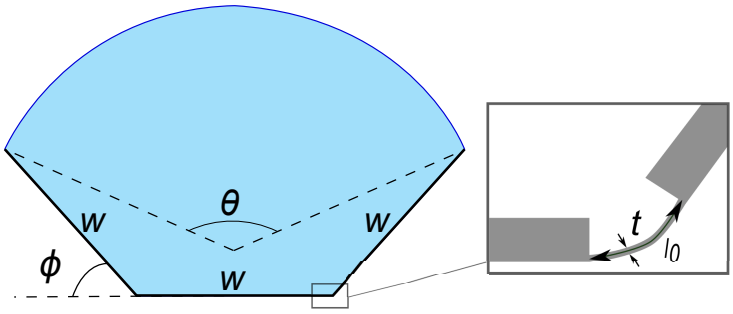

Figure 2.2 – Geometrical parameters of the two-dimensional model. We consider infinitely stiff flaps of width w connected to each other by flexible hinges of thickness t and length l_0. ϕ represents the rotation angle of the flaps ($0 < \phi < 2\pi/3$); θ is the angle of the arc formed by the air-liquid interface ($-\pi < \theta < \pi$).

2.2 Theory

2.2.1 2D elastocapillary model

The two-dimensional model presented in this paper is an extension of our earlier work [53].

We consider the simplest case of a hydrophilic structure completely covered by liquid; its contact line is strongly pinned on the edges of the outer flaps; see Figure 2.2. The liquid tends to reduce its interface in contact with air, inducing a deformation of the flexible structure. The total energy of the system is the sum of the bending energy $U_b = \phi^2 B/l_0$ [J m^{-1}] of the hinges (B bending stiffness; see next section for more information) with the surface energy of the curved interface $U_\gamma = \frac{\gamma w \theta(\cos\phi + 1/2)}{\sin(\theta/2)}$ [J m^{-1}] (with γ surface energy [J m^{-2}]). The total energy, normalized to the surface energy and taken per unit length to obtain a unit-less parameter, then becomes:

$$\bar{U} = \frac{U_\gamma + U_b}{\gamma w} = \theta \frac{\cos\phi + 1/2}{\sin\theta/2} + \beta\phi^2 \tag{2.2.1}$$

where

$$\beta = \frac{B}{l_0 \gamma w} \tag{2.2.2}$$

The parameter β characterizes the balance between mechanical bending forces and surface tension. It includes all tunable parameters of the structure, i.e. thickness t, length l_0 of the hinges and width of the flaps w. β will be used

later in part 2.4.2 as a fitting parameter to compare our experimental results with the theory.

From Figure 2.2, we can also define the normalized volume σ (in our 2D approach, $\sigma = S/w^2$ where S is the surface of the cross section):

$$\sigma = \frac{\theta}{2}\frac{(\cos\phi + 1/2)^2}{\sin^2\theta/2} - \frac{(\cos\phi + 1/2)^2}{\tan\theta/2} + \sin\phi + \frac{1}{2}\sin 2\phi \qquad (2.2.3)$$

It is now possible to compute the minimization of the total energy of the system (equation 2.2.1) with the volume constraint expressed in equation 2.2.3. Energy minimization is achieved at constant volume, meaning that the meniscus can take any shape because of the unconstrained pressure inside the liquid. Three distinct folding behaviors as a function of β emerge from the simulations, as shown in Figure 2.3.

In the case of flexible structures, i.e. for low values of β, the system allows only one minimum during the entire folding and complete closure occurs at $\sigma = 0.41$ (see the top curves in Figure 2.3).

For intermediate structures, where $0.68 < \beta < 0.80$, a metastable situation emerges as two distinct minima appear with an energy barrier between them; see middle curves in Figure 2.3. Whether the system jumps from one minimum to the other or not will determine the final state of the system. The structure will completely close if no jump occurs (case 1 in the second curve) while the structure will reopen in the second case. As an example, the energy barrier for a 800 µm long structure with 80 µm wide flaps wetted by clean water ($\gamma = 72\,\mathrm{mJ\,m^{-2}}$, $\beta = 0.75$) is approximatively $\delta U \approx 10\,\mathrm{nJ}$ (the smallest energy barrier was extracted from our simulation, it is not represented in Figure 2.3). Such an energy could be introduced to the system through, for example, vibrations. Considering the volume of water (mass $\approx 10 \times 10^{-8}\,\mathrm{kg}$) as a resonator of natural frequency 5 kHz and a vibration criterion VC-A (like in our laboratory), a first mode vibration already gives an energy of this order of magnitude. Therefore, the outcome of the assembly will depend on the experimental conditions.

For higher values of β, two minima also appear at a certain point as shown on the bottom curves in Figure 2.3. Contrary to the previous case, the reopening of the structure corresponds to the "no jump" case, while a sudden closure of the structure is expected if the system jumps from one minimum to the other.

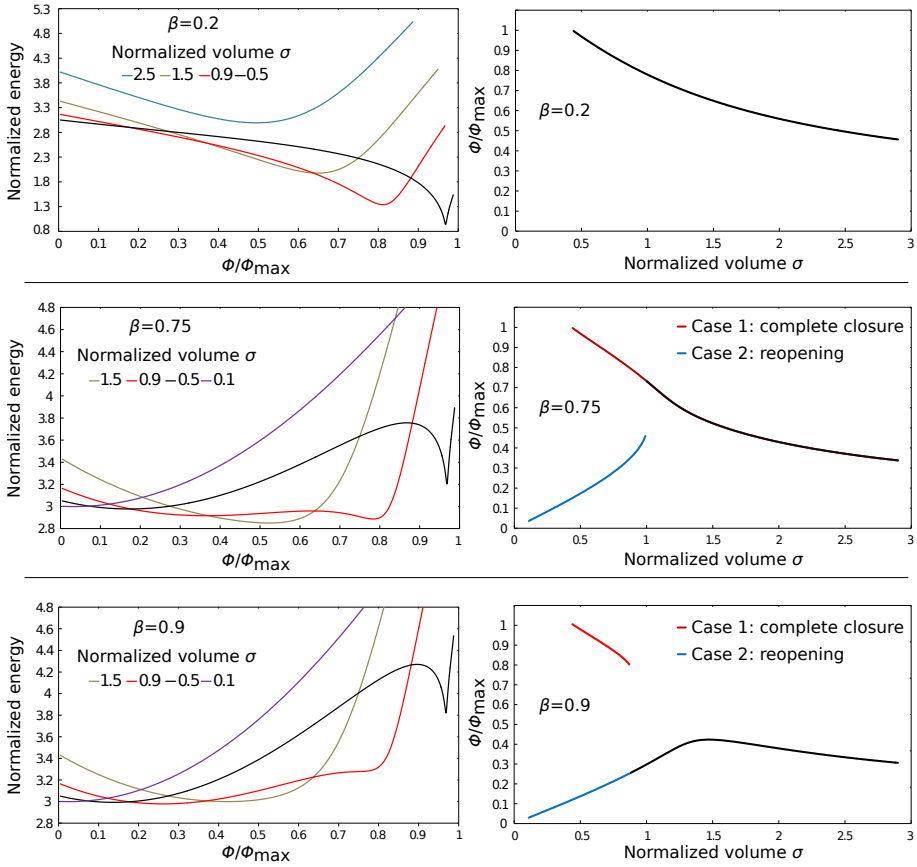

Figure 2.3 – Total energy of the elastocapillary system for several normalized volumes and folding curves for three different values of β: flexible structure ($\beta = 0.2$, top), metastable situation ($\beta = 0.75$, middle) and for a stiffer structure ($\beta = 0.9$, bottom). Folding curves should be read from right to left as the volume decreases during folding. For low β values, the system allows one minimum; the structure folds until reaching the maximal folding angle. A metastable situation appears for intermediate β values ($0.68 < \beta < 0.80$). The structure will either close or reopen depending on which minimum the system selects. For the example shown, this situation arises at $\sigma = 1.0$. For higher β values, the situation is the same except that the outcome is opposite: the structure would reopen if the system remained on the initial minimum.

2.2.2 Bending stiffness and resonance frequency

As described in the previous section, the bending stiffness B of folding structures is an important parameter since it characterizes the mechanical flexibility of the structure in equation 2.2.2. For a plate of thickness t, B is defined as the moment per unit length per unit of curvature and equals [57]:

$$B = \frac{\tilde{E} I_{y,h}}{L} = \frac{E t^3}{12(1-\nu^2)} \; [J] \tag{2.2.4}$$

where ν and E are the Poisson's ratio [.] and the Young's modulus [Pa] of the material of the plate, respectively, and L is the length of the considered structure. $\tilde{E} = E/1-\nu^2$ is the effective modulus for plates that are much wider than thick, leading to plain-strain conditions [58]. $I_{y,h}$ [m^3] is the area moment of inertia of the hinge in the y direction.

The hinge-flap system, visible on both sides in Figure 2.2, is equivalent to two constant cross-section segments that are serially connected. In the case of bending, the resonance frequency of such a system is the summation of the single-profile effective stiffness and mass properties of the individual segments [59]:

$$\omega_0 = \frac{k_h + k_f}{m_h + m_f} \tag{2.2.5}$$

where k_i and m_i are the effective spring constant and the effective mass of the members, respectively. The subscripts h and f stand for hinge and for flap, respectively. The parameters can be calculated using the Rayleigh method and are equal to:

$$\begin{aligned} k_i &= \tilde{E} I_{y,i} \int_{l_i} \left(\frac{\mathrm{d}^2 u_{z,i}(x)}{\mathrm{d}x^2} \right)^2 \mathrm{d}x \\ m_i &= \rho A_i \int_{l_i} u_{z,i}^2(x) \mathrm{d}x \end{aligned} \tag{2.2.6}$$

where ρ is density and A_i the cross-sectional area.

The function $u_{z,i}(x)$ represents the deflection of the considered segment i at any arbitrary point x of the cantilever. $u_{z,i}(x)$ is related to the maximum deflection u_z at the free end of the flap by means of a bending distribution function $f_{b,i}$:

$$u_{z,i}(x) = f_{b,i}(x) u_z \tag{2.2.7}$$

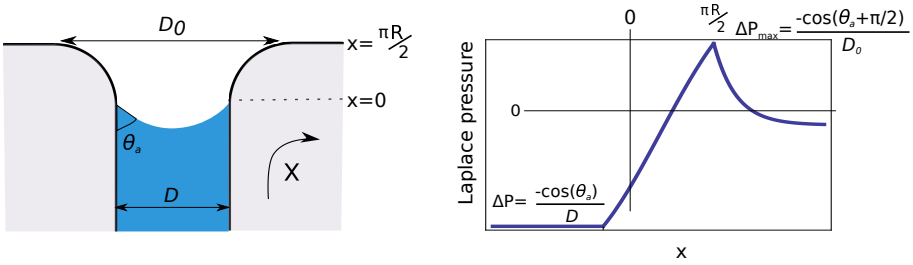

Figure 2.4 – Theoretical Laplace pressure (ΔP) inside clean water versus the position in a tube with an edge of radius of curvature R. Contact angle of water is θ_a. x represents the position of the contact line of the meniscus. Spontaneous filling of the tube happens by capillary forces (negative Laplace pressure). ΔP gradually increases as the angle that forms between the meniscus and the vertical grows from θ_a to $\theta_a + \frac{\pi}{2}$. The maximal value is only determined by the maximal diameter and not by the shape of the transition.

Functions $f_{b,i}$ are derived by applying Castigliano's displacement theorem. Calculations for a two segments micro-cantilever are well described in [59] and therefore are not specified here.

In the case of our structures, where $m_f \gg m_h$ and $k_h \gg k_f$, 2.2.5 simplifies to:

$$\omega_0 = \frac{k_h}{m_f} = \frac{\tilde{E} I_{y,h} \int_{l_h} \left[\frac{\mathrm{d}^2 f_{b,h}(x)}{\mathrm{d}x^2} \right]^2 \mathrm{d}x}{\rho A_f \int_{l_f} f_{b,m}^2(x) \mathrm{d}x} \tag{2.2.8}$$

Good agreement between resonance frequencies measurements on fabricated structures, finite elements simulation and this model has been found with an error lower than 5 %. Therefore, the model developed here can be used to relate resonance frequency measurements to the bending stiffness of the hinge through fitting of the term $\tilde{E} I_{y,h}$, which is common between equations 2.2.4 and 2.2.8.

2.2.3 Pinning effect

Once the meniscus proceeding through the tube meets the diverging section at the top of the tube, it is pinned. The overpressure needed to overcome the pinning effect in an axisymmetric micro-channel and to move the meniscus

on top of the origami pattern is given by the Young-Laplace equation:

$$\Delta P_{\max} = -\frac{4\gamma \cos\left(\theta_a + \frac{\pi}{2}\right)}{D_0} \tag{2.2.9}$$

where γ is the surface tension of water, θ_a the advancing contact angle of water on silicon nitride and D_0 the maximum diameter of the tube. The shape of the transition between the vertical tube and the horizontal structure does not influence the maximum pressure that needs to be applied, as demonstrated and experimentally verified in recent work [60, 61].

Figure 2.4 shows the theoretical pressure along a smooth tube derived from equation 2.2.9. No overpressure needs to be applied until the water reaches the position in the tube where the meniscus becomes flat. For ultra clean water (γ = 72 mN/m) in a silicon nitride tube of diameter D_0=50 µm, the maximal overpressure needed to wet the surface is approximately equal to $\Delta P_{\max}$ =3.7 kPa. For this calculation, the advancing contact angle was measured to be θ_a=(40 ± 2)° using a dynamic sessile drop method.

In case of a practical fluidic system that is not infinitely stiff, this overpressure causes a slight increase of the total amount of liquid in the system. Once the meniscus leaves the tube, the overpressure reduces. This releases additional liquid from the relaxing system resulting in an overshoot.

2.3 Experimental section

Figure 2.5 shows a concise outline of the fabrication process for the origami patterns used in the experiments along with an example of a resulting structure. Our folding experiments were carried out using the dedicated setup shown in Figure 2.6. The elasticity of the system is designed to be as small as possible to limit the amount of overshoot. Fluidic connection to the tube in the wafer is achieved by a tiny recessed o-ring in a metal part. The wafer sits on the metal part and the connecting force is predominantly transferred between metal and wafer. In this way, we aim to limit the change in expansion of the o-ring under liquid pressure variation. Other measures are the use of a Hamilton glass syringe and thick-walled PEEK tubing. Finally, the volume between the syringe plunger and the sample is kept as low as possible (around 10 µL). One top camera and one side camera with adequate magnification allow us to record the folding process.

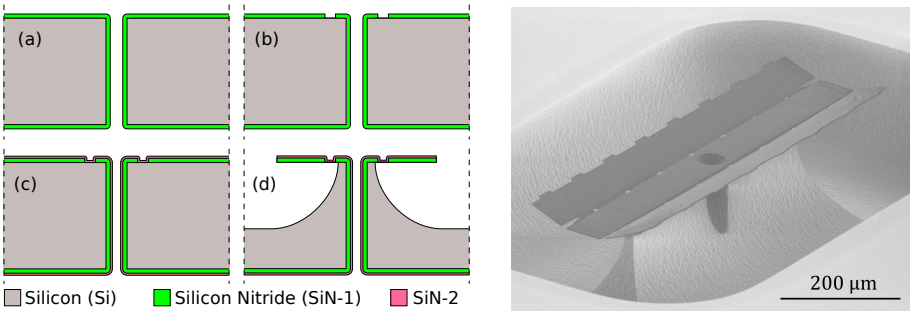

Figure 2.5 – Fabrication outline (cross-section). (a): A tube is etched all through the wafer and a 1.1 µm thick layer of silicon nitride (SiN-1) is conformally deposited. (b): Dry etching at each hinge's location. (c): A second 125 nm thin layer is deposited (SiN-2). This layer is thin enough to be deformed by surface tension (i.e. small bending stiffness B). (d): A final lithographic step is used to define the overall geometry of the structures and to release them by a semi-isotropic silicon etch. The structures are cleaned in HNO_3 just before the final lithographic step and final cleaning is done by O_2 plasma. Bottom: resulting structure. Length of the structure is 780 µm and flap width is 76 µm. The hinges are 6.8 µm wide and the diameter of the tube is 50 µm. Holes were patterned along the hinges to reduce their stiffness. Note that the flaps are initially not in the same plane as the central part.

Folding experiments are performed by first filling the syringe by opening the valve and removing the plunger. Once the syringe is filled, the plunger is put into the syringe and the valve is closed. In this way, there is no additional pressure applied on the sample by the height of the water container. Once enough pressure is applied to flow water on top of the structures, actuation of the syringe is stopped. Subsequently the volume is fixed, and the theory described in part 2.2.1 (energy minimization achieved at constant volume) holds for these experiments.

2.4 Results and discussion

2.4.1 Overshoot

The pressure that needs to be applied to wet the structures (see part 2.2.3) causes an overshoot of water on the structures. As described in the previous section, optimization of the setup was carried out in order to limit this excess of liquid.

To quantify the overshoot of the fluidic setup, the syringe pump was quasi-statically actuated, starting with water in the through-wafer tube filled by

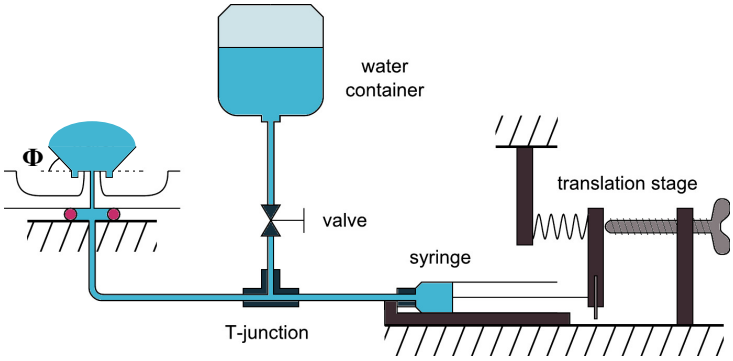

Figure 2.6 – Schematic of fluidic setup filled with ultra clean water. Fluidic connection to the wafer is made with a recessed o-ring in a metal part. Tubing is thick-walled (PEEK) and the syringe is made of glass. The angle Φ represents the rotation of the flaps, plotted in Figures 2.7 and 2.9.

capillarity (D_0=50 µm). When water exceeded the edge of the tube and wetted the surface, actuation of the pump was stopped. The water droplet volume was derived from the captured video. Measurements on geometrical features of identical structures in SEM images were used as a reference. The optimization of our experimental setup resulted in an overshoot of around (1.4 ± 0.4) nL. In comparison, a completely filled structure like the one showed in Figure 2.5 contains around 200 nL.

2.4.2 Through-wafer elastocapillary folding

The evolution of folding of 2D extruded prismatic structures (Figure 2.5 bottom) was recorded during the evaporation of water after the structures had been wetted by through-wafer filling. The angle of rotation Φ of the flaps with respect to the central part was extracted from captured videos every few seconds, along with the normalized volume of water.

Figure 2.7 shows the folding diagram of two structures with different stiffnesses. The hinges of the flexible object are patterned with holes 50% longer than in the rigid one, resulting in a stiffness 50% lower. The first object folds until reaching the maximum folding angle, $\phi_{max} = 2\pi/3$, at which point the object remained closed because of sufficiently large stiction forces between the two flaps. On the other hand, the stiffer structure 2 does not attain the maximal angle of rotation during folding. The structure then reopens and the flaps come back to their initial position.

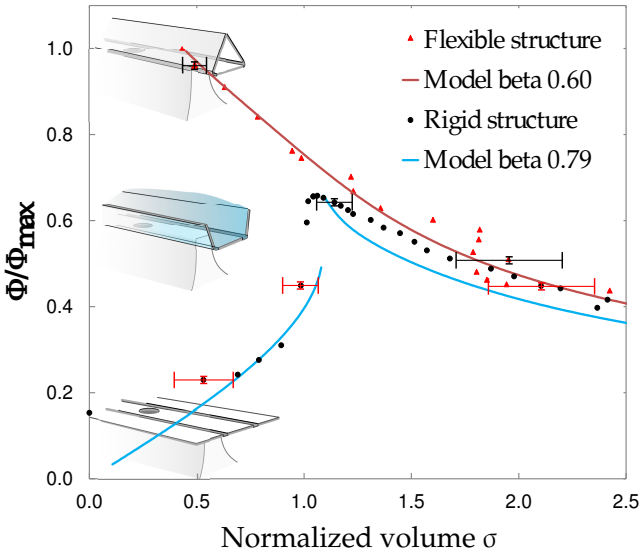

Figure 2.7 – Flap angle Φ versus liquid volume, for two elongated structures similar to the one shown in Figure 2.5 but with a different spring constant. Folding curves should be read from right to left as the volume decreases during folding. The more flexible structure (red triangles) closes completely. A stiffer object (black circles) does not attain the maximal rotation and reopens. The experimental points were extracted from videos of folding with an interval of 0.4 s. Solid lines: theoretical values from our 2D model presented in part 2.2.1, fitted by tuning parameter β. The maximal reached folding angle was used to fit the theoretical curve for the rigid case.

Solid lines in Figure 2.7 show the best fit of theoretical curves computed from our model presented in part 2.2.1. The fitted value for the flexible structure ($\beta = 0.60$) agrees well with the value of 0.59±0.09 we calculated using equation 2.2.2, considering the surface tension of clean water and using geometrical measurements from SEM images. The hinge thickness was measured with good accuracy (4 %) thanks to a focus ion beam experiment. The fitted value $\beta = 0.79$ for the rigid structure slightly differs from the calculated 0.89±0.09. Uncertainty as to the Young's modulus value could explain the deviation. In addition, the theoretical curve fitted in the case of the flexible structure corresponds to a metastable situation that is described in detail in part 2.2.1. The discontinuity that is observed corresponds to a jump from one local minimum to another, and it seems that this is what also happens experimentally. However, when approaching the maximal rotation angle, the folding slows down resulting in several data points lying just before this value. At

the same time, the shape of the meniscus changes significantly at the extremities of the structure, and therefore comparison with our 2D model should be made only with caution. On the other hand, the reopening is spontaneous and quick. Possibly, what we observe might correspond to a slightly higher β value at which the theory predicts a reopening without discontinuity (starting at $\beta = 0.80$, see bottom curve in Figure 2.3).

2.4.3 Repeatable folding

Another novelty of this through-wafer filling technique is the facility to repeatedly open and close the structures. Figure 2.8 as well as online supplementary material show the actuation of a cubic structure. Once the pinning of water at the edge of the tube is overcome, accurate addition and retraction of water is possible by using the syringe pump. Such controlled reopening of structures was impossible using the top filling method that we employed in our previous work [53, 54].

The folding of structures, which takes a few minutes when letting the water evaporate (Figure 2.8 between b and d), can be considerably sped up to times of less than a second by retracting water through the tube. As long as the structures remain wet, it is possible to fold and reopen them dozens of times without any visible signs of wear. Objects were actuated this way up to 60 times. Furthermore, the maximal folding angle that is reached for every actuation remains constant. Our results demonstrate that multiple elastocapillary folding at the micrometer scale is possible, which opens a route towards more complex structures, such as micro-actuation and possibly drug delivery.

Surprisingly, a rather different result is obtained when the water is allowed to dry in between foldings. In that case, a structure that undergoes several actuations shows a different behavior for every iteration, as shown in Figure 2.9. While the flaps reach an angle of 80° before reopening during the first actuation, the maximal angle of rotation drops to 40° during the fifth folding. Structures which close at first folding can be reopened by simply wetting them again. After a few actuations the objects do not close anymore and we observe a similar decrease in final achieved angle as presented in Figure 2.9.

A large amount of residue was observed on top of the structures after their actuation; see Figure 2.10. This residue aggregates at the level of the outer hinges, where the evaporation rate is highest during drying. Observed under a fluorescence microscope, this residue gleams. The debris can be partially

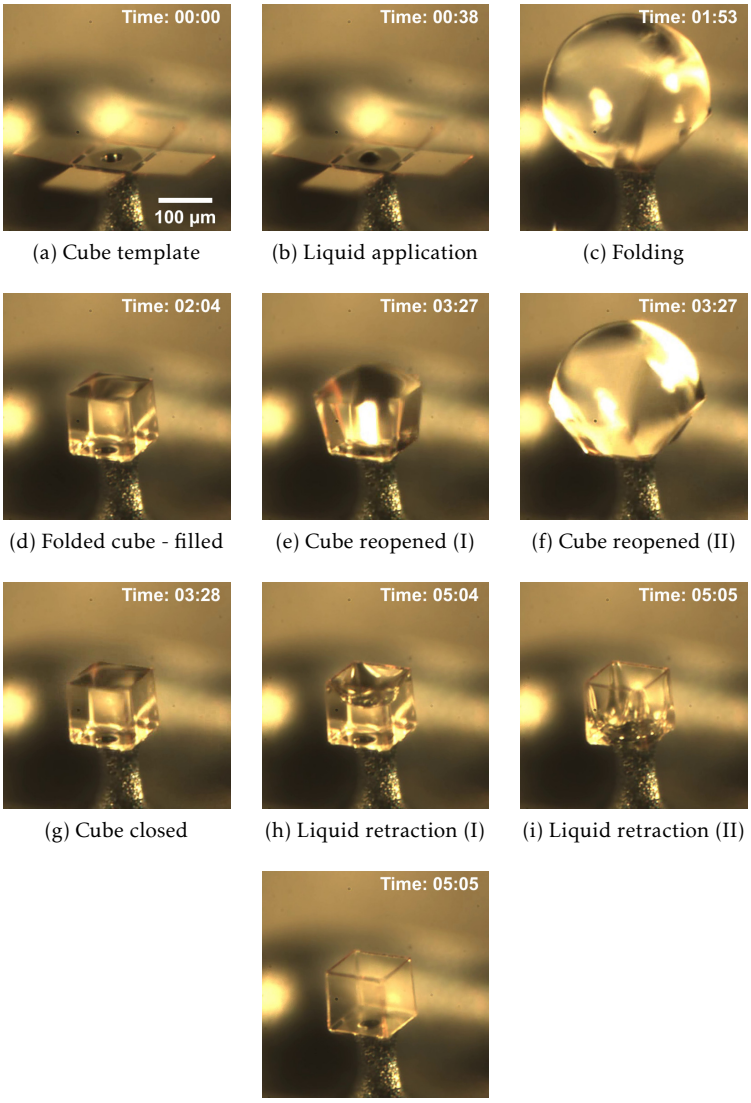

(a) Cube template (b) Liquid application (c) Folding

(d) Folded cube - filled (e) Cube reopened (I) (f) Cube reopened (II)

(g) Cube closed (h) Liquid retraction (I) (i) Liquid retraction (II)

(j) Folded cube - empty

Figure 2.8 – (a-h): Chronological sequence of images from a movie of the folding process of a five-faced cube with a rib length of 100 µm (time format: mm:ss). Between (b) and (d) the folding occurred by allowing the water to evaporate. In the time between (d) and (h), the cube was repeatedly opened and closed (20 times). One sequence of opening and closing is shown from (e) to (g).

removed by O_2 plasma, and the residue does not gleam anymore under the fluorescence microscope, accounting for organic material, such as photoresist. The remainder of debris can be washed in water, leaving a clean structure. Once released from the silicon wafer (step IV in Figure 2.5) it is impossible to clean the structures in liquid. The photoresist that is present on top of the flaps is etched away in O_2 plasma. However, some of the photoresist that is protecting the edge of tubes is likely not to be removed, and could explain the presence of residue on the final structures. Furthermore, reaction products from the under-etching step might be redeposited during the release.

To estimate the impact of this residue, several foldings of the same structures were carried out. The resonance frequency was systematically measured in between foldings to determine the bending stiffness of the structures, as described in part 2.2.2. Besides, for every iteration the folding curves were extracted and a β value was fitted using the maximum achieved folding angle. Figure 2.11 shows the obtained results for a structure that endured fifteen successive foldings. As expected, the object becomes stiffer with every iteration, the bending stiffness increasing because of the residue accumulation. Consequently, the maximum achieved folding angle decreases, resulting in an increasing fitted parameter β. A similar evolution was observed for four others structures with different stiffnesses.

The two latter parameters, bending stiffness B and β, are related to the surface tension γ through 2.2.2. Since B and β show similar evolution, we can conclude that the surface tension remains relatively constant. However, small changes over time are plausible given the large amount of residue. B is measured after folding rather than during, unlike β. B is therefore measured after residue is allowed to settle and dry. Moreover, the silicon nitride hinge endures severe deformation while bending. Even though we do not observe plastic deformation, it is possible that the bending stiffness is changing while folding, hence impacting the folding behavior.

2.5 Conclusion and outlook

We have demonstrated controllable capillary folding of planar silicon nitride templates into 3D micro-structures by means of through-wafer liquid application. For the first time, hydro-mechanical, repeatable actuation of capillary folded structures via subsequent addition and retraction of water has been achieved. While remaining wetted, structures have been folded and reopened

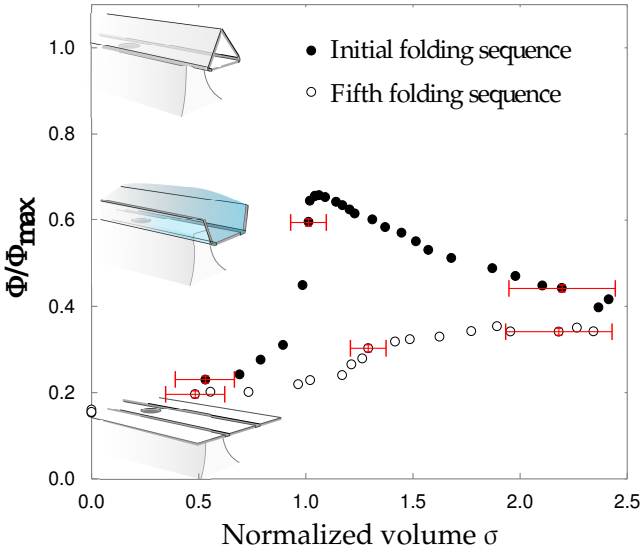

Figure 2.9 – Normalized flap angle Φ versus volume for the same structure measured for the first folding sequence (closed circles) and during the fifth sequence (open circles) when the water is allowed to completely dry in between foldings. The maximal rotation angle decreases with the number of iterations. Folding curves should be read from right to left as the volume decreases during folding.

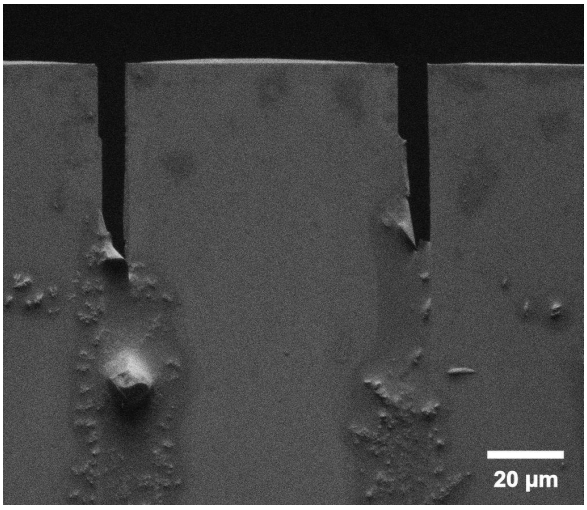

Figure 2.10 – SEM picture of the top part of the silicon nitride template after several folding sequences, showing the accumulation of residue on the hinges. The residue is probably caused by the fabrication process, which contains a final release step that cannot be followed by a liquid cleaning step (see Figure 2.5).

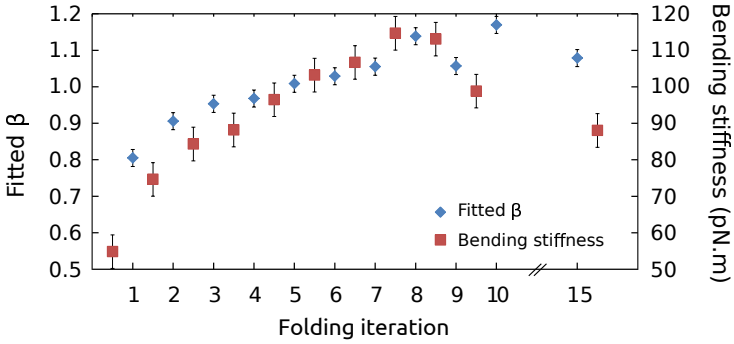

Figure 2.11 – Measurement of the bending stiffness through resonance frequency measurements and subsequent fitting of β value on folding curves extracted from experimental videos for the same structure during fifteen successive folding iterations.

up to 60 times in a row without any signs of wear, and the finally achieved angle remains constant throughout the actuation.

Through-wafer filling requires a sufficiently high pressure to overcome pinning of the liquid meniscus at the edge of the tube. Precise hydro-mechanical actuation can only be achieved by selecting rigid components for the fluidic setup. In our set-up, the volume of excess liquid could be reduced to (1.4 ± 0.4) nL.

When the structures are allowed to dry in between folding, we observe that residue is deposited on top of the hinges during the drying process which makes the structures stiffer, with an increase of bending stiffness by 50 % after the first folding. Folding of objects was monitored during several repeated cycles of filling and subsequent evaporation of water. The maximum achieved angle decreased with every cycle for all tested structures. This residue probably originates from our fabrication process, during which it is difficult to efficiently clean the structures once they are released form the substrate.

When drying, the flaps adhere and the structures remain folded. Material, similar to debris, can be observed between the flaps. It is possible to reopen the objects simply by wetting them again, indicating that the 'glue' that keeps the structures assembled can be diluted in water. The procedure (wetting - drying/adhesion - reopening) can be repeated as long as the debris do not prevent the structures from closing.

As a potential application, one could imagine a network of silicon nitride tubes that can be closed or reopened on demand through individually ad-

dressable tubes. Flaps could be patterned with electrical wires and a 3D sensor/actuator array can be formed.

Moreover, fabricated structures with tubes could be a way for large-scale batch elastocapillary folding of 3D micro-objects. It is a technical challenge since all tubes should overflow at the same pressure, but this seems a doable challenge overall.

3

Capillary origami of micro-machined micro-objects: bi-layer conductive hinges

3.1 Introduction

Self-folding broadly refers to the self-assembly of interconnected parts that fold up into predefined shapes without the need of active human control. The assembly is either triggered by external stimuli (pH or temperature variation for instance), enabled by external forces such as magnetic or by internal forces such as pre-stressed layers [5, 22, 23]. Three-dimensional assembly of micro/nano objects is possible using self-folding, where inherently two-dimensional micro-fabrication techniques have shown to be inadequate [4].

Capillary origami designates the self-folding of flexible elastic material using surface tension as enabling force [24, 41]. Capillary origami is a particularly interesting tool for micro-fabrication since surface forces dominate over bulk forces, such as gravity, at small scales [46, 62]. This technique was first employed to assemble silicon-based micro-objects by Syms *et al.* who used melting solder to assemble hingeless silicon objects with integrated metal pads in flaps [33, 40]. The scope of solder assembly was then extended by Gracias *et al.* who demonstrated the folding of complex structures (cubes, pyramids...) of micrometer and nanometer sizes fabricated using standard lithography and deposition techniques [26, 27, 38, 39]. Applications of such structures range from three-dimensional micro-opto-electro-mechanical-systems (MOEMS) [35–37] to RF nano-antennae [63].

We have used capillary origami to fold silicon nitride micro-objects. Contrary to solder assembly, the structures are necessarily hinged and their folding relies on the deformation of thin flexible silicon nitride plates, therefore the method can also be called elastocapillary folding. Folding is driven by the surface tension of water, which is simply manually deposited [53, 54] or brought to the origami pattern through a tube at its center [64]. The final objects shape

Submitted to a peer-reviewed journal. Available on *ArXiv e-prints*. Authors: A. Legrain, J. W. Berenschot, N. R. Tas and L. Abelmann.

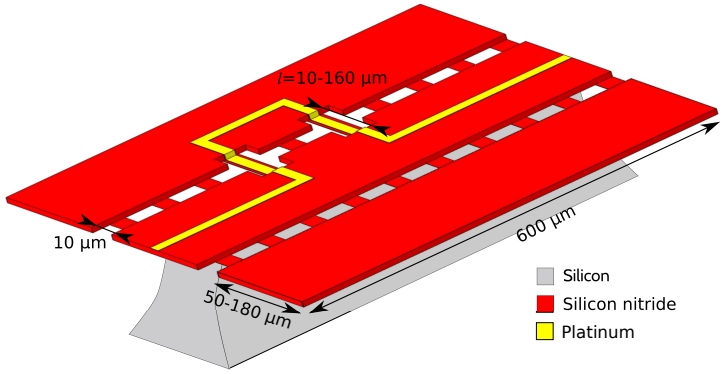

Figure 3.1 – Concept image of a typical test structure. Two free hanging silicon nitride flaps are connected to the central part by means of thin flexible silicon nitride hinges. The central part is fixed, resting on a silicon pillar. In this example, two decoupled bi-layer hinges are running at the center of the structure. The length l of the metalized junctures can be tuned while the plain SiRN hinges are always 10 µm long. The metal parts run to contact pads on the outside of the structures.

is predefined by the patterning of rigid silicon nitride plates - that form the body of the 3D object - linked to each other by hinges. Objects remain assembled due to strong stiction between flaps [53, 64] or by designing complex stop-programmable hinges [54].

The applications of this self-folding technique is limited to situations where a passive mechanical structure is required that extends far above the wafer surface. To extend the range of applications, it would be extremely useful if electrical connection can be made to the moving parts of the folding structure. Electrical conductance over hinges has been demonstrated in experiments where folding is achieved by magnetic lifting [44, 65] or stress gradients [66, 67]. In this work we combine electrical connectivity with folding by capillary forces. Figure 3.1 shows the type of structures used to prove feasibility of conductive hinges. Structures based on our previous publications [53, 64], are extended with Platinum wires that are running from the substrate towards the flap via bendable hinges. After elastocapillary folding, a three-dimensional triangular prism structure ("Toblerone") is realized that has electrical wiring on the movable parts.

In the following we will explain the fabrication process and demonstrate that conductivity can be preserved under folding. We will focus on the yield of the process and discuss various causes of failure during fabrication.

3.2 Experimental section

3.2.1 Fabrication

Figure 3.2 shows the necessary steps to micro-machine test structures such as the one depicted in Figure 3.1. Fabrication starts with the conformal deposition by low pressure chemical vapor deposition (LPCVD) of a low stress thick silicon nitride (SiRN, Figure 3.2-(a)). Three layers - 499, 797 and 1083 nm - were deposited on different samples to investigate the influence of the step height on the fabrication yield.

A first lithographic step follows to etch away the thick SiRN at the location of the future hinges. For this step, both dry and wet etching were used in order to study the impact on folding of the shape of the transition between the hinges and the flaps. Dry etching is performed after patterning only the photoresist, and yields a straight profile in the thick SiRN layer. Wet etching requires first the deposition of a thin polysilicon layer ($\simeq$ 50 nm). The polysilicon layer is patterned using dry etching, and subsequently used as a mask to etch SiRN in isotropic wet etchant, either hydrogen fluoride (HF) or phosphoric acid (H_3PO_4). The resulting shape is a smooth circular transition, inherent to isotropic etching. Once silicon is reached, the thin polysilicon layer can be stripped in tetramethylammonium hydroxide (TMAH).

The next step is the deposition of a thin flexible layer of SiRN by LPCVD, Figure 3.2-(c). A thickness of 100 nm has proven to offer both flexibility and solidity for the hinges [53, 64].

The second lithography step follows to define the geometry of the patterns, Figure 3.2-(d). In this design, combinations of different flaps widths (50-180 µm) - leading to different final folding angles - with different bi-layer hinge lengths (10-160 µm) were tried out. The location of conductive hinges was also varied, and reference structures (structures without SiRN below metal or with no metal) were included.

Next, metal is deposited and patterned on top of SiRN by a standard lift-off procedure, Figure 3.2-(e). Chromium ($\simeq$ 10 nm) is used as an adhesive layer. Two different layers of Platinum, 75 nm and 150 nm, were sputtered on different samples at a pressure of 6.6×10^{-6} bar. The thicknesses of the final metal layers were checked using a mechanical surface profiler. Lift-off was achieved by first coating and patterning a 3.5 µm thick photoresist with no post-development baking to keep the profile of the resist straight. After

metal deposition, the wafers were placed in a ultrasonic bath and immersed in sequence in acetone and in isopropanol.

Finally, a last lithography step is performed to protect the SiRN objects during their release, Figure 3.2-(f). Under-etching of silicon is performed in semi-isotropic sulfur hexafluoride (SF_6) gas etchant. Since all structures should be released simultaneously, the mask openings are designed of equal size and at the same distance from the final etch location.

Moreover, it should be noted that the etching selectivity between silicon and SiRN during this step is around 1000. The initial thickness of the SiRN layer from which the hinges are patterned (Figure 3.2-(c)) was therefore chosen accordingly thicker ($\approx 20\,\text{nm}$), to compensate for thinning during the silicon etch step.

Finally, photoresist is stripped in oxygen plasma for two hours once the objects are released from the substrate.

3.2.2 Residual stress measurements

Stress in deposited thin layers was measured using the wafer curvature method. The curvature of a dummy wafer is measured before and after deposition of the thin film by means of a surface profiler. Stress is then calculated using the Stoney equation [68]. In the case of SiRN, for which material is deposited on both sides of wafers by LPCVD, one side of the wafer is stripped before measuring the radius of curvature. The thickness of substrates is measured using a dedicated tool (Heidenhain measuring station) while the thickness of SiRN and sputtered metals are checked by ellipsometry and mechanical surface profiler, respectively. Values found in the literature are used for Young's moduli and Poisson's ratios.

3.2.3 Experimental setup

Self-folding experiments and electrical characterization are carried out in the same setup, shown in Figure 3.3. Resistivity of the structures is measured by a multimeter *in situ* during assembly by means of two metal probes placed on metal contact pads on both sides of the structures. For breakdown measurements, a voltage source was used to force a current through the bi-layer hinges.

A glass micro-pipette of 10 µm diameter is positioned on top of the micro-origami pattern by an accurate x-y translation table. A low volume syringe

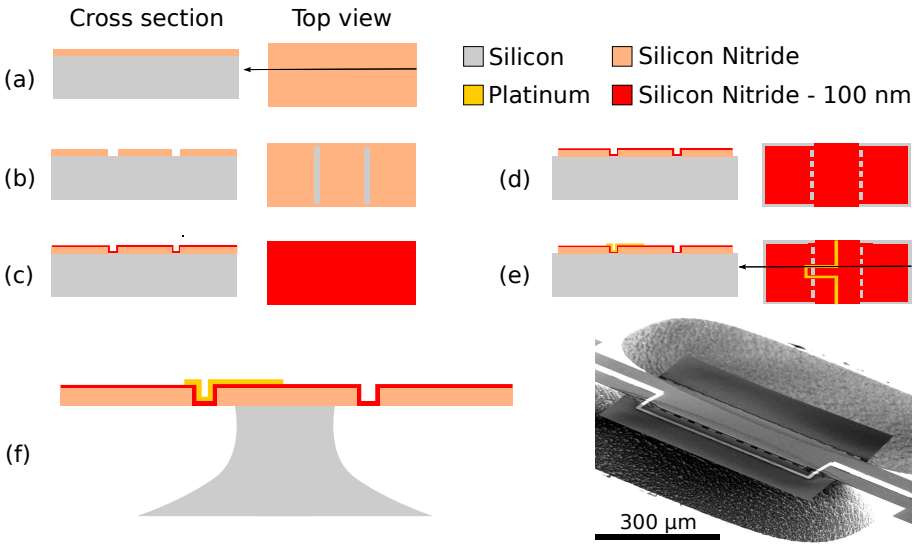

Figure 3.2 – Fabrication steps for silicon nitride (SiRN) structures with integrated conductive hinges, that can be folded out of the plane by capillary forces. (a): Deposition of SiRN by LPCVD. (b): First lithographic step; definition of the hinges. SiRN is either dry or wet etched. (c): Second deposition of SiRN. (d): Overall definition of the structures by a lithography step and subsequent dry etching. (e): Sputtering of metal followed by a standard lift-off procedure. (f): Release of the flexible objects by semi-isotropic etching of silicon. The SEM picture on the right hand side shows an example of a final structure.

(~ 10 µL), filled with ultra pure water, is used to propel a drop out of the micro-pipette. A hydrophobic polytetrafluoroethylene (teflon) coating is applied on the micro-pipette to avoid wetting of the outside of the glass pipette. Two cameras on top and on the side are used to monitor the folding process. Depending on the volume of liquid deposited, folding takes 10 to 120 s.

3.3 Results and discussion

3.3.1 Fabrication yield

As described in part 3.2.1, various combinations of metal thicknesses and step heights have been fabricated. Moreover, the transition between the hinges and the flaps was machined by dry etching, resulting in a sharp step, as well as wet etching, resulting in a smooth circular transition.

All the aforementioned parameters do not have any significant influence on the fabrication yield. The only feature that proved to have a statistically

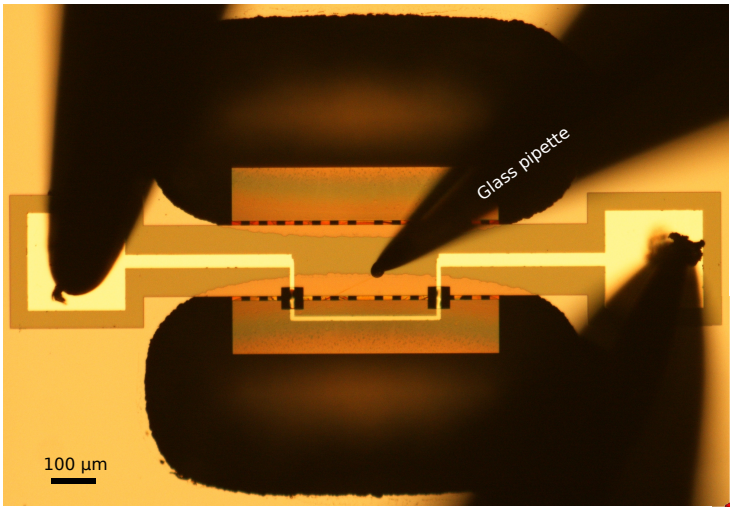

Figure 3.3 – Photograph of used experimental setup, top-view. The foldable object is placed at the center. A glass syringe is positioned on top of the structure by means of a translation table, and is used to apply water for the folding process. Metal probes are in contact with metal pads on both sides.

Hinge length			Conductivity yield	N
10	$\leq l \leq$	75 µm	(77 ± 2) %	541
75	$< l \leq$	100 µm	(26 ± 4) %	129
	$l >$	100 µm	(18 ± 2) %	391

Table 3.1 – Fabrication yield of conductive hinges as a function of hinge length, before folding. A correlation between length and conductivity is obvious. Statistics made with N structures from 7 wafers, which were fabricated with different combinations of thicknesses for the thick SiRN flaps (499, 797 or 1083 nm), thicknesses of Platinum (75 or 150 nm) and etching method for hinges (dry or wet, Figure 3.2-(b)). No significant impact from the latter parameters was observed on the resulting yield.

significant impact on the yield is the length of the composite hinges. Table 3.1 summarizes our results. Short hinges, with a length l below 75 µm, are the most robust with a yield of (77 ± 2) %. The variance on this value is calculated from the number of structures tested assuming a binomial distribution. The yield drastically drops for longer junctures, and less than one out of five structures are conductive when $l \geq 100$ µm. The reasons will be made clear in section 3.3.3. Short hinges are therefore the best option for the design of conductive bi-layer junctures.

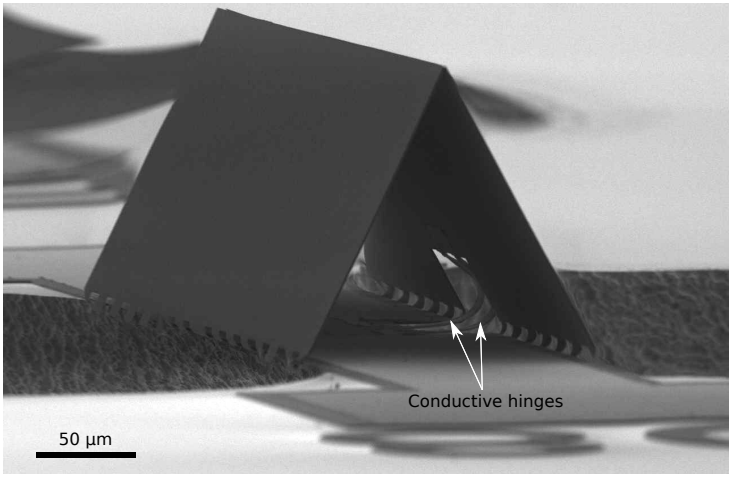

Figure 3.4 – Folded micro-object with conductive bi-layer hinges that allow for electrical connection to the folded flaps. The structure is 600 µm long and the flaps are 80 µm wide. The plain SiRN hinges are 10 µm long and 30 µm wide, while the two bi-layer hinges are 75 µm long.

3.3.2 Folding and electrical characterization of conductive hinges

Fifty structures with conductive bi-layer hinges were successfully folded and monitored using the setup presented in Figure 3.3. No breaking or change in the conductivity of the hinges was observed. Figure 3.4 shows an example of a folded micro object, with the two conductive hinges inside the right hand-side flap. Folding angle and length of the bi-layer hinges have no impact on folding. As shown in Figure 3.6 the conductive hinges do not break even when they are rotated by 180°. Picture (b) shows 10 µm bi-layer hinges that are fully rotated and yet do not break , therefore resulting in a radius of curvature $R \sim 5\,\mu m$. These are shortest that can be designed since they are as long as the plain SiRN hinges. We can therefore conclude that the folding of metalized hinges do not yield a stress higher than their failure stress, even in extreme conditions. Such extremely small radii can be found in recent publications on flexible electronics. Using ultra-thin substrates (< 2 µm), the wrapping of thin film transistors (TFT) around human hairs, $R \sim 50\,\mu m$, was demonstrated [69] and fully printed organic TFTs could be folded to very small bending radii of about $R \sim 5\,\mu m$ [70]. Bendable organic solar cells with $R \sim 10\,\mu m$ [71], as well as polymer-based LEDs with $R < 10\,\mu m$ [72] have also been reported. High flexibility can also be achieved by placing the electronics in the neutral strain

position: CMOS circuits could be bent to a radius as small as $R \simeq 85\,\mu m$ [73] and organic TFTs were folded to radii of about $R \sim 100\,\mu m$ [74].

The resistivity between the two metal probes was measured to be in the order of $110\,\Omega$ and $80\,\Omega$ for a thickness of Platinum of 75 nm and 150 nm, respectively. The value varies by 25 %, depending on the total length of metal and the exact landing position of the probes. These values are higher than theoretical values of respectively $(64 \pm 18)\,\Omega$ and $(32 \pm 5)\,\Omega$, calculated from the bulk value of resistivity of Platinum, $\rho_b = 1.06 \times 10^{-7}\,\Omega\,m$. The difference can be explained by additional contact resistances as well as the fact that the resistivity of Platinum thin films is known to be higher than the bulk value. A factor 5 is reported for 20 nm Platinum thick films [75, 76]. It seems therefore likely that the resistivity is larger than the bulk value in our situation, especially for a Platinum thickness of 75 nm.

The current running in the hinges was measured while applying an increasing potential difference at their terminals. The resistance increases at higher voltage, as is illustrated by a linear fit through the points below 1 V. It is likely that this increase is caused by an increase in temperature. The measured resistance however includes the series resistances and therefore cannot be used to estimate the temperature of the metal layers.

The bi-layer hinges lost conductivity during experiments when a current density $j = (1.6 \pm 0.4) \times 10^6\,A/cm^2$ was running through them, as shown in Figure 3.5. This value of current density is close to reported values in literature at which electromigration was observed [77, 78]. However, the failure could also be attributed to the high temperature induced by the high current density, which is linked to degradation of Platinum films [79]. In this case the dominant mechanism is agglomeration, a surface-diffusion-driven capillarity process, which effect is worsened by temperature coefficients mismatch between the different layers [80]. It is possible to limit the impact of high temperature on the hinges through annealing or depositing Platinum without an adhesion layer [81].

3.3.3 Hinge deformation

While short hinges show no deformation and are nicely curved after folding, see Figure 3.6, longer junctures are deformed, see Figure 3.7. The deformation occurs only at the level of the flaps, with the hinge section connected to the fixed central part remaining intact. In photograph (b) we can see that the flap

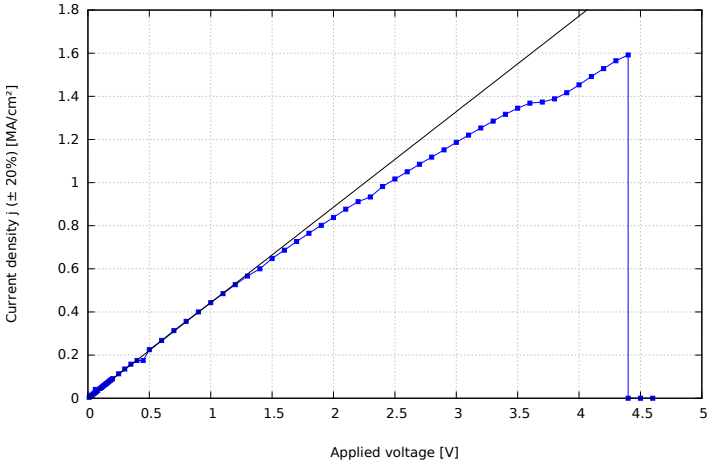

Figure 3.5 – Current-voltage characteristic of a bi-layer conductive hinges. The conductivity breaks down at $j = (1.6 \pm 0.4) \times 10^6$ A/cm^2. The solid black line is a linear fit through the points below 1 V.

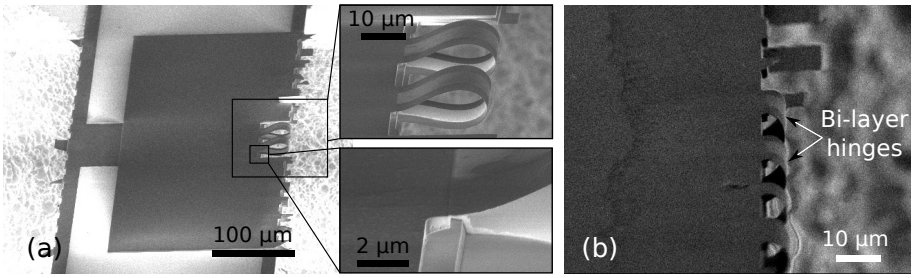

Figure 3.6 – (a): Extreme folding of 50 µm long hinges over an angle of 180°. Top inset: zoom-in on the formed loop, no deformation of the bi-layer junctures can be observed. Bottom inset: zoom-in at the transition between the flaps and the bi-layer junctures. The standard sputtering method yields a nice conformal step coverage. (b): Even the shortest hinges of 10 µm length sustain a 180° rotation.

is tilted out of the plane, which suggests that the deformation in the bi-layer junctures is due to this pre-folding. Despite the strong deformation, the hinges are still conductive.

Figure 3.8 shows similar hinges without metal top layer. These plain decoupled SiRN hinges are deformed in a similar way as the bi-layer version of Figure 3.7. As before, the section of the hinges connected to the central part remains intact. The other side, connected to the flap, remains parallel to the thick SiRN plane for a short distance before the curvature starts.

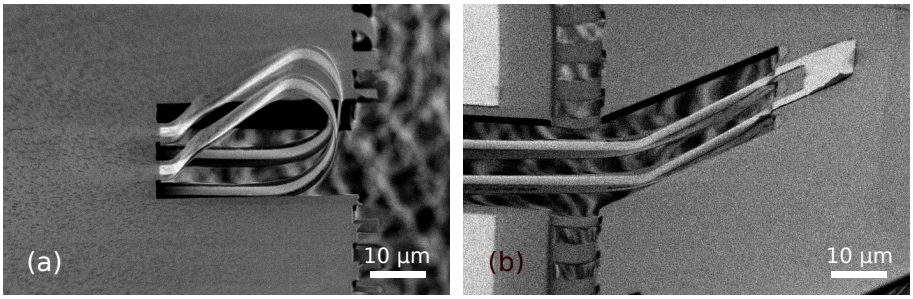

Figure 3.7 – Bi-layer hinges from two distinct structures. (a): $l = 100\,\mu m$, was folded by 180° using the setup shown in Figure 3.3. (b): $l = 105\,\mu m$, was not folded. The flap is tilted out of plane (around 30°). Both structures are still conductive but show deformation due to stress mismatch between the different layers. In both cases only the parts located at the level of the flaps are deformed.

Why this deformation occurs is unclear. We can imagine several possible explanations for this effect, none of which seem adequate. The flaps are up to ten times thicker than the hinges, and stress mismatch between the two SiRN layers could explain the plastic deformation. There is no evidence however of thickness dependency of residual stress in SiRN layers in the literature. SiO_2 layers between the two SiRN layers or under the SiRN formed as the wafers are loaded in the LPCVD equipment are also candidates. But such layers would be a few nm thick, and it is unlikely that they could be the cause of such large bending. We also observed that during stripping of photoresist in an oxygen plasma, the last step of fabrication, temperature rises and the photoresist melts, which results in folding of the flaps. As will be discussed in the next section, we observe the degradation of metal during this same step. Such degradation could be attributed to diffusion of Chromium, which starts at 300 °C. The stresses due to melting photoresist at rather high temperatures may cause permanent plastic deformation of the hinges. The correct explanation however is probably a combination of the previously described factors, coupled with the complex three-dimensional shape of the flap-hinges system.

Next to curvature along the hinges, buckling in the transverse direction is present in the case of bi-layer hinges, see Figure 3.7. This buckling is not visible in the case of plain SiRN hinges, Figure 3.8. Since we suspect that this is caused by stress gradients, we measured the residual stress using a wafer curvature method, see part 3.2.2. The SiRN shows tensile stress, $\sigma_{r-SiN} = (-169 \pm 25)\,MPa$, whereas the stress is compressive for Platinum, $\sigma_{r-Pt} = (452 \pm 70)\,MPa$. This significant mismatch causes a stress gradient

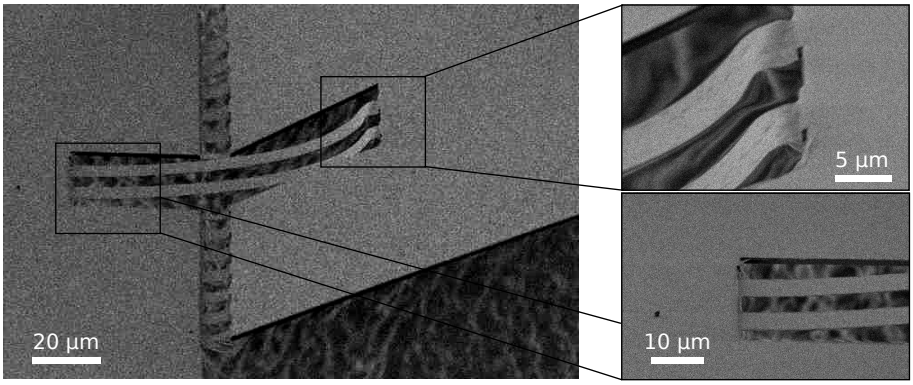

Figure 3.8 – Plain decoupled SiRN hinges. Although no metal is present on top of the junctures, the deformation already seen for bi-layer objects can be observed here. Most of the constraint seems to happen at the transition from the flap to the thin junctures.

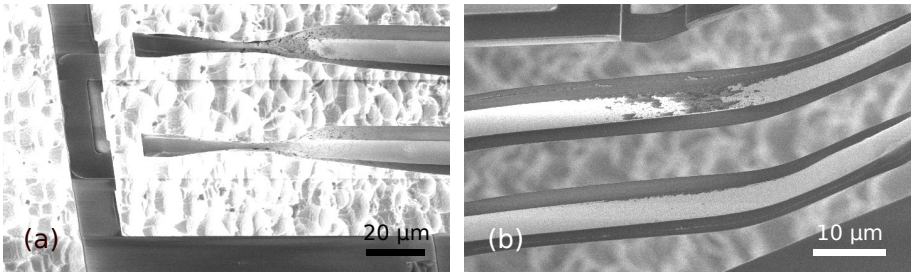

Figure 3.9 – Typical failures of long hinges that show no conductivity. (a): l = 160 µm. For very long junctures, buckling and bending can cause the hinges to break at the transition with the flaps. (b): l = 125 µm. Platinum burns at the middle of the hinges.

along the bi-layer stack, which could explain the observed deformation.

3.3.4 Failure mechanism

Deformations caused by stress can cause the bi-layer hinges to break, as shown in Figure 3.9-(a). This is however the case only for very long hinges, typically $l > 150\,\mu m$. Most of the long hinges lose conductivity because of a poor metal coverage following the final oxygen plasma cleaning step as shown in Figure 3.9-(b). Why this deterioration of Platinum happens is unclear. Electrical discharge and heating during the two hour final oxygen plasma cleaning step seems to be the only plausible explanation.

3.4 Conclusion

We have successfully fabricated free-standing silicon-nitride plates with integrated Platinum electrodes, that can be folded by elastocapillary forces into three-dimensional objects of several hundred µm in size. The electrodes are guided to the free-standing folding elements of the objects over two bi-layer silicon nitride/Platinum hinges.

The resistance of the hinges does not change during folding. A current density as high as $j = (1.6 \pm 0.4) \times 10^6\,\mathrm{A/cm^2}$ was flown through the hinges before conductivity was lost.

None of the fifty bi-layer hinges, fabricated with different lengths, broke during folding. Bending radii as small as 5 µm were achieved without mechanical failure or lost of conductivity.

If hinges break, it is during the fabrication process. Hinges with a length below 75 µm were mostly conductive with a high yield of (72 ± 2) %. The yield drops to (18 ± 2) % for bi-layer hinges with a length above 100 µm. The yield is not influenced by the thickness of the connected flaps or the Platinum layer, nor the method used to etch the hinges' molds (wet or dry).

Short hinges with a length below 50 µm are nicely curved and show no deformation or burning after folding. Mid-sized hinges, from 50 to 75 µm, do not break for most of them but show visible deformation such as buckling and bending. Similar deformations are observed even when there is no metal on top of the hinges. Although made of the same material as the hinges, the connected flap is folded out of plane by around 30°.

The failure mechanism during fabrication is either breaking or burning of the top Platinum layer. In the case of long hinges with a length over 100 µm, the stress mismatch in the layers cause the breaking of the hinges at their connection with the flaps in rare cases. The majority of failures is however due to burning of the Platinum top layer which is observed after the final oxygen plasma cleaning step, leading to loss in conductivity.

Elastocapillary folding is a powerful technique that allows the 3D assembly of silicon based objects of mm size, which is knowingly hard using inherently two-dimensional fabrication techniques. However, the self-folding method has lacked applications so far. We believe that these conductive hinges will extend the application scope of elastocapillary folded structures, with possible applications in out-of-plane sensing, high aspect ratio coils or even 3D electronics.

4

Elastocapillary folding using stop-programmable hinges fabricated by 3D micro-machining

4.1 Introduction

4.1.1 Self-folding of 3D micro-structures

The fabrication of 3D micro-structures has become an important field of interest in the scientific community over the past three decades [5]. Traditional mask-based approaches, such as photo-lithography and its developments (including X-ray lithography, electron-beam lithography and dip-pen nanolithography), have proven to be inadequate for fabricating truly 3D-patterned structures. The main limitations include: an inherent two-dimensionality, size limitations, being time-consuming, and demanding a complex fabrication [4].

Fabrication examples of 3D structures abound in nature. Salt crystallization and the folding of protein or DNA are processes that engineers dream of reproducing in a laboratory with as much precision and reproducibility as is seen in nature. The process by which disordered components are organized into patterns or structures without human intervention is known as "self-assembly" or, by analogy with the previously mentioned top–down methods, a "bottom–up" approach [82]. Although great proofs-of-concept have been published [83, 84], such engineering suffers from a too high level of uncertainty, as pointed out by Gracias *et al.* in their excellent review [5]. Therefore, they prefer the use of a more deterministic form of self-assembly known as "self-folding" or "micro-origami". Combining the strengths of both lithography and self-assembly, the final 3D structure is predetermined by the linkages between the different parts that are assembled. The obvious link with origami, the ancient Japanese art of folding paper, provided its name to this tech-

Submitted to a peer-reviewed journal. Available on *ArXiv e-prints*. Authors: A. Legrain, J. W. Berenschot, N. R. Tas and L. Abelmann.

nique [85]. While origami-like planar structures are fabricated using standard micro-machining techniques, many methods of self-folding have been investigated, some more efficient than others. These methods include ultrasonic pulse impact [86], pneumatics [87], electroactive swelling [88, 89], thermal actuation of polymer films [19, 90–92], thin-film stress-based assembly (TFSA) [42, 93–96], magnetic forces [32, 97–100], and capillary forces. Surface tension is probably the most common method of self-folding. In the micro/nanometer world, interfacial forces dominate over body forces such as gravity, making them a perfect candidate for the self-folding of micro-structures. Syms was the first to introduce this method by using solder pads which are melted to power assembly before solidification in their final state [33, 35]. More recently, this method has had great nanoscale applications as a result of the work of Gracias *et al.* [38, 39, 101]. For a complete overview of self-folding techniques, see the recent reviews [5, 21–23].

An elegant macro-scale illustration of self-folding by surface-tension is Bico *et al.* [24, 46, 48], who demonstrated the spontaneous wrapping of thin millimeter-sized polydimethylsiloxane (PDMS) sheets around a water droplet: the so-called elastocapillary folding technique. Using the same concept, our group has demonstrated the fabrication of silicon nitride 3D micro-objects by capillary forces in which the actuating liquid, in our case water, disappears as a result of its spontaneous evaporation. Final closure is assured by the strong cohesion between flaps without the need for solder, and the assembly is carried out under ambient conditions either by simply depositing water on top of the structures [53] or by providing a liquid through a tube at the centre of the objects [64].

A crucial feature of self-folded objects is to pre-determine their final shape. Some techniques require a locking mechanism, for example, some research on self-folding by magnetic interaction [97, 99], while another treatment of magnetic self-folding relies on plastic deformation [32]. Using solder assembly, the quantity of melting material determines the final folding angle [33, 38, 41]. Likewise, in TFSA, the final radius of curvature is a function of the stresses in the different layers, with curvatures ranging from a few millimeters down to nanometers [42, 93, 94]. The final shape from using self-folding polymer films can be controlled by designing several small shrinking hinges in series [23, 90, 91].

Structures folded by elasto-capillary interactions are limited in terms of their final three-dimensional shapes. Folding ceases once the moving flaps

encounter an obstacle, typically a nearby flap, and the elasticity of the hinges causes the objects to re-open if not enough stiction is present between the flaps [24, 53, 64]. The work presented here aims at extending the scope of elastocapillary folding of silicon nitride micro-objects by predefining the final assembly. The principle of these stop-programmable hinges is presented in Figure 4.1.

Made of a thick rigid part and a thin flexible part, these complex hinges are designed in such a way that the final assembly angle is predefined by their shape. After folding through evaporation of water, the two opposite thick parts meet and adhere. The final folding angle therefore depends on the initial angle between the substrate and the thick parts of these smart hinges.

4.1.2 Corner lithography and self-folding

Corner lithography is a wafer scale nano-patterning technique that offers the opportunity to form structures in sharp concave corners, independently of their orientation in space. The conformal deposition of a material layer over a patterned substrate will result in a greater effective thickness in any sharp concave corner. Isotropic etching therefore yields nano-features as presented in Figure 4.2. This technique was first developed and used in our laboratory to create silicon nitride nano-wire pyramids [102]. We then extended the scope of this technique by demonstrating the use of the structures formed by corner lithography as a mask for subsequent patterning steps [103]. In the meantime, Yu *et al.* demonstrated the fabrication of nano-ring particles and photonic crystals using corner lithography [104]. More recently, our group has continued the development of this technique and demonstrated the parallel nano-fabrication of fluidic components with cell culturing application [105], as well as the wafer-scale fabrication of nanoapertures [106] and the machining of silicon nitride 3D fractal structures [107].

In this paper, we use corner lithography to fabricate the smart hinges presented in Figure 4.1. Sharp features must be avoided when it comes to bending or folding, since they lead to an extreme concentration of stress [108, 109]. Consequently, corner lithography needs to be performed in rounded molds for our purposes. This situation leads to conditions on the radius of curvature of the mold, as well as on the thicknesses of the subsequently deposited material. In general, the total thickness of the materials that are deposited in rounded molds must be greater than their radius of curvature so as to have

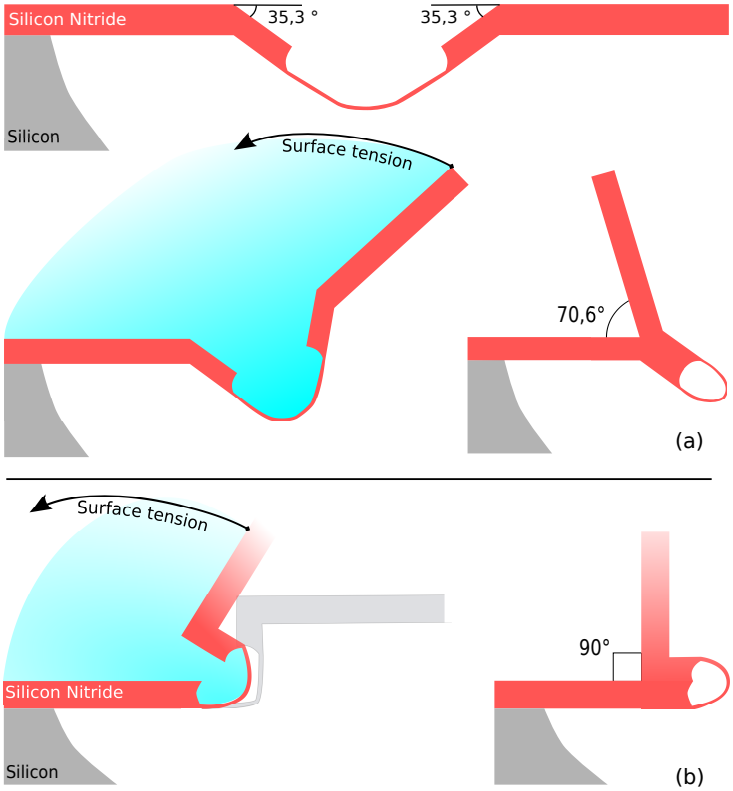

Figure 4.1 – The stop-programmable folding principle. The design of the complex hinges is such that once folded, the flap forms a predefined angle with the planar support. Self-folding of the structure is enabled through evaporation of water and decrease of the liquid–air interface of the meniscus. (a): 70.6° stop-programmable hinge. (b): 90° stop-programmable hinge. In both cases, the flaps adhere thanks to a sufficiently large stiction area and there is no need for a locking mechanism.

some material remaining after the isotropic etching, as shown in Figure 4.3.

4.2 Fabrication process flow

In this section we present the fabrication steps necessary to build the stop-programmable hinges depicted in Figure 4.1. The main steps are the same for the fabrication of both folding angles, although 90° stop-programmable hinges require the use of wet etching to pattern the vertical sidewalls, unlike the 70.6° complex hinges, for which everything can be accessed by dry etching. Moreover, methods to obtain the molds differ. The two following

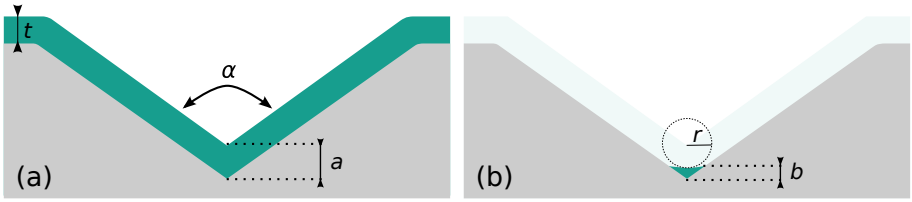

Figure 4.2 – Corner lithography in a sharp corner. (a): When a conformal layer of thickness t is deposited over a concave corner of opening α, the effective thickness of material at the corner is $a = t/\sin(\alpha/2) > t$ [102]. (b): After isotropic etching by an amount of r, material with thickness $b = a - r$ remains in the corner.

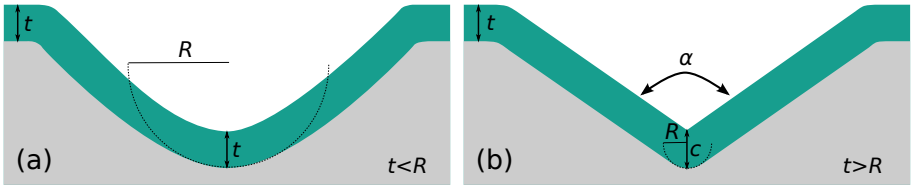

Figure 4.3 – Corner lithography in a rounded corner. (a): When a material layer of thickness t is conformally deposited over a mold with radius of curvature R that is greater than t, the thickness at the tip is unchanged. (b): On the other hand, when R is less than t, a concave corner is created and the effective thickness is $c = R + (t-R)/\sin(\alpha/2)$.

sections extensively describe the process flow, with the first part describing the whole procedure for 70.6° smart hinges, and the second part pointing out the differences when fabricating 90° stop-programmable hinges.

4.2.1 70.6° stop-programmable hinges

The strategy is similar to that presented by our lab in previous publications [103, 105]. Corner lithography is here employed to create a masking layer which will be subsequently used to etch the underlying body layer before being removed. Figure 4.4 shows the procedure step by step for machining a 70.6° stop-programmable hinge.

The initial Si (silicon) molds will define the shape of our final object. The opening angle α of the molds, see Figure 4.2 and 4.3, defines the final folding angle, β, through the relation $\beta = \pi - \alpha$. Silicon has a face-centred cubic structure with a well-defined lattice. The angle between the top <110> plane and the {111} planes is exactly 35.3°, as depicted in Figure 4.1. Etching the molds with KOH on (110) oriented wafers yields well-defined openings with the de-

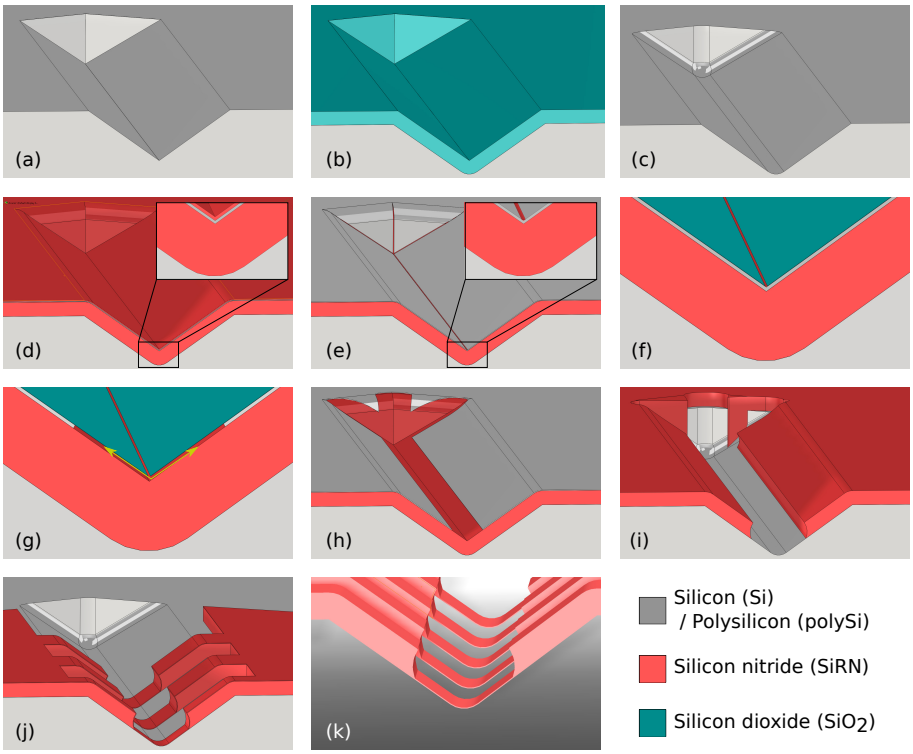

Figure 4.4 – Fabrication of a stop-programmable hinge, example of a 70.6° smart hinge. (a): On a (110) oriented silicon wafer, V-grooves are etched. (b) and (c): These grooves are rounded off by means of oxidation and subsequent etching. (d): A SiRN/polySi/SiRN stack of layers is conformally deposited. (e): The top SiRN layer is isotropically wet etched using a time stop such that material remains in the corner. SiRN wires run in all three directions. (f): This remaining SiRN nanowire is used as a protection mask during partial oxidation of the underlying polySi layer. (g): After removal of the SiRN line the polySi layer is retracted. (h): SiO_2 is stripped. (i): Using the polySi layer as a mask, an opening is etched in the SiRN layer. An oxidation and subsequent wet etching step follow to remove the polySi layer (not shown here). (j): After deposition of flexible layer of SiRN, a mask is applied through lithography and the overall geometry of the structure is determined by directive ion etching. (k): A last lithography step follows for protection of the SiRN objects during semi-isotropic etching of Si. Once released from the substrate, the smart hinge is ready to be self-folded.

sired opening angle (α=109.4°, β=70.6°) with sharp transitions between the different planes, see Figure 4.4 (a). Note that the mask pattern, consisting of rectangular openings, needs to be rotated by 54.7° with respect to the vertical <111> planes in order to get rectangular V-grooves with KOH etchant.

The bending of sharp objects is to be avoided since it leads to extreme stress concentrations [108, 109]. We therefore use an oxidation step to round off the molds, Figure 4.4 (b). Kim *et al.* showed that high temperature oxidation is an efficient method to round off sharp silicon V-grooves [110]. Linear relations between the oxidation time and the final achieved radius of curvature were experimentally found by the authors for (100) oriented wafers but not for (110) wafers. Our own oxidation experiments followed by SEM inspections allowed us to determine a similar relation for a 1150°C wet oxidation step applied to (110) wafers:

$$R = (124 \pm 72) + (94 \pm 7)\sqrt{t} \tag{4.2.1}$$

with R the final radius of curvature in nm and t the oxidation time in min. A 98 min oxidation step yields a 1 µm radius of curvature and is used for our fabrication, Figure 4.4 (b). It is difficult to use a higher radius of curvature since that would imply a deposition of a thicker material layer, as described in Figure 4.3 (a). Once SiO_2 (silicon dioxide) is stripped in HF, the molds are ready for corner lithography.

First, two layers are deposited by low-pressure chemical vapor deposition (LPCVD): first, a thick silicon rich nitride (SiRN) layer that is to be structured to form the thick part of the smart hinges, see Figure 4.1, followed by a polysilicon (polySi) layer. The total thickness of material here needs to be greater than the initial radius of curvature R as was emphasized in Figure 4.3. Typically, we deposit a 1 µm SiRN layer and a 150 nm polySi layer in a mold where the radius of curvature R is 1 µm. In any case, the following design criterion should be respected:

$$t_{\text{SiRN-1}} + t_{\text{polySi}} \geq R \tag{4.2.2}$$

where $t_{\text{SiRN-1}}$ and t_{polySi} stand for the thickness of the bottom SiRN and the polySi layers, respectively.

On top of this stack, a last conformal layer of SiRN is deposited. Provided that the design criterion has been respected, the cross section of the stack should look like Figure 4.4 (d). There are no constraints on the thickness of

the top SiRN layer, but it needs to be perfectly known since this layer will be time-etched in phosphoric acid (H_3PO_4) to form SiRN nanowires at the bottom of the grooves as shown in Figure 4.4 (e). In the case of a $\alpha = 109.4°$ opening, the material is 22 % thicker at the tip (see Figure 4.2) and over-etching of the SiRN layer is allowed within this limit. We have used a thin SiRN layer of about 100 nm to reduce the etching time.

Thanks to the newly formed nanowires running in the three dimensions, the underlying polySi layer can be partially oxidized (Figure 4.4 (f)) using SiRN nanowires as an inversion mask. Half of the polySi thickness can be consumed during this step without issues. Once the nanowires are selectively etched, the polySi layer can be retracted starting from the tips where nicely defined access points are now formed, step (g). TMAH as an etchant is a nice option here since its selectivity between SiRN and SiO_2 is high and the etching speed not too fast to be controllable, but KOH could also be used. Careful timing is necessary during the retraction, since the length of the flexible parts of the smart hinges are determined during this step, see Figure 4.1. Typically, a TMAH solution at 25 wt% at 95°C attacks polySi at a speed of 1 µm min^{-1}.

The above steps result in a patterned polySi layer on top of the thick SiRN layer, Figure 4.4 (h). Using the polySi layer as a mask, it is now possible to etch the underlying SiRN layer in HF 50 %. Due to the isotropic nature of the etchant, a retraction equal to the thickness of the material etched will occur under the polySi masking layer. Moreover, when the thickness of the SiRN layer to be etched is greater than the initial radius of curvature R, an over-etching is necessary to remove the surplus material (Figure 4.3), its thickness can be calculated by

$$c = \frac{(t - R)}{\sin(\frac{\alpha}{2})} \tag{4.2.3}$$

with t the thickness of the conformal layer and α the opening angle of the mold.

In order to remove the polySi masking layer, an oxidation step should be preferred over a wet etching step since we want to conserve the rounding of the mold. This short oxidation step will consume the polySi material and slightly increase the radius of curvature of the mold. Moreover, the oxidation of the Si substrate will yield a specific shape, known as a “bird’s beak”, at the transition between the Si and the SiRN [111]. This shape is not visible in Figure 4.4 but will be shown in the results part of the paper (Figure 4.10).

After removal of the polySi layer, Figure 4.4 (i), the flexible part of the hinges is deposited by LPCVD. The bending stiffness of the hinges is $B = {Et^3}/{12(1-\nu^2)}$ for thin plates, where E is Young's modulus and ν is Poisson's ratio [57]. It is highly dependent on the thickness t of the thin plate, and the thinner is this layer, the more flexible is the hinge. 100 nm thin hinges offer both mechanical solidity and flexibility [53, 64]. On the other hand, the final release of the foldable objects requires the etching of the Si molds in SF_6, which also slightly attacks SiRN. The thinning of the hinges during the release step should therefore be taken into account when depositing the thin SiRN layer. We measured a selectivity of around 1000 between silicon and SiRN using our etching system (Adixen AMS100 Reactive Ion Etcher).

A second lithography step follows to define the overall geometry of the smart hinges. Making holes along the length of the hinges permits reducing their stiffness and facilitates the folding. Lithography in molds up to 10 µm deep is relatively straightforward when using an appropriate photoresist. In this specific case, dry etching can be used to remove the SiRN, step (j). An extra lithography step must be performed to protect the SiRN structures by photoresist during the semi-isotropic etching of the silicon. Once released from the silicon substrate, the stop-programmable hinges are ready for assembly. When designing the masks, extra care was taken to assure that all structures were etched free from the substrate at the same time during the last step. Ideally, the mask openings should be of the same size and placed at the same distance from the stop-etching point.

The 70.6° stop-programmable hinges thus fabricated can be used to self-fold perfectly defined tetrahedrons. Since only one out of three hinges in a tetrahedron pattern lie at the right intersection between the planes in the silicon lattice, as shown in Figure 4.5, only one smart hinge can be formed in the way that was just described. The other two hinges are therefore flat junctures made by standard micro-machining. An extra lithography step followed by dry etching is therefore necessary between steps (i) and (j) in Figure 4.4.

4.2.2 90° stop-programmable hinges

The procedure to fabricate 90° stop-programmable hinges is nearly the same as for the 70.6° hinges described above, except for two important differences: making 90° molds in silicon is very difficult using wet etching—our attempts using correctly oriented (110) wafers always resulted in tiny bumps at the

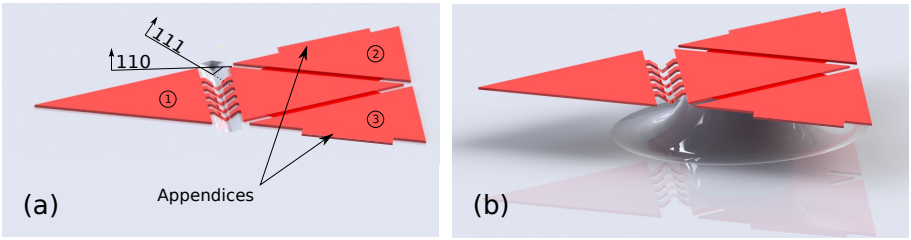

Figure 4.5 – Fabrication of a tetrahedron folding pattern, extra steps. (a): Since only one of the hinges lies on the correct intersection of the planes, standard lithography is used to define flat hinges for the other faces. Faces ② and ③ are designed with small appendices on their sides to allow them to lock onto face ① while folding. (b): Under-etching of Si by semi-isotropic etching of silicon (SF_6 etchant). Etching is stopped when the hinges are free and the central flap rests on a silicon pillar.

bottom edges of the molds—and the vertical SiRN sidewalls obtained in these molds cannot be patterned using directive dry etching. Steps (a) and (i–j) in Figure 4.4 therefore differ when it comes to the micromachining of 90° stop-programmable hinges.

Given that the depth of the molds is small, cryogenic dry etching is a good option for our purpose. Unlike the BOSCH processes, cryogenic etching yields smooth sidewalls [112], which are crucial for our sensitive corner-lithography technique. Retraction of the mask is also a well known problem in dry etching and might be an issue for corner-lithography. In general, when developing a dry etching step for the purpose of performing corner lithography later on inside the molds, any concave corners other than the ones at the bottom of the molds should be avoided. This includes potential roughness of the masking material and retraction of the mask. Moreover, the final opening angle α is highly dependent on the etching conditions (type of mask used, loading, gas flows) and requires precise tuning.

After performing the corner lithography, it is necessary to pattern the SiRN features before releasing the structures, Figure 4.4 (i–j). While reactive ion etching is a perfect option for 70.6° stop-programmable hinges, it is impossible to use it in the case of the vertical molds obtained by dry etching. The difficulties arising with upright sidewalls are twofold, as shown in Figure 4.6. One is the difficulty to etch several µm of material from the top. And the other is the vertical thick SiRN plate of the complex hinge, see Figure 4.1, that makes impossible a proper illumination of the photoresist for the subsequent litho-

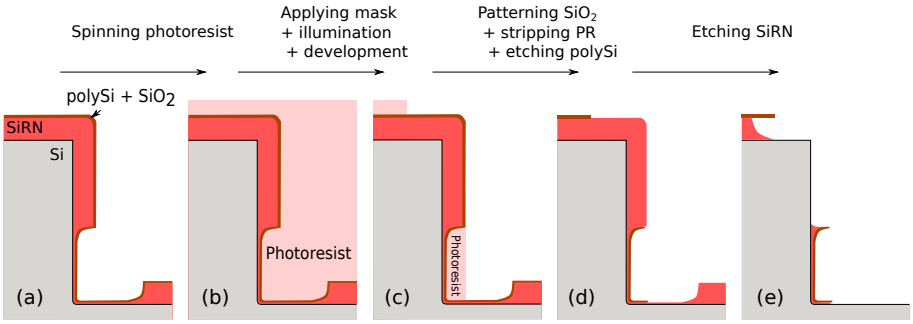

Figure 4.6 – Difficulties arising when implementing corner lithography in an upright mold. We consider the case where the process flow depicted in Figure 4.4 has been followed up to step (i) inclusive. (a): Dry etching is impossible, a wet etching strategy must be considered using a masking layer. A polySi layer is deposited followed by short oxidation. (b): Photoresist is spun over the wafer. The use of a thick photoresist dedicated to high-aspect ratio structures protection is necessary to protect the molds. (c): Directional nature of UV illumination makes impossible the proper patterning of photoresist under the thick SiRN plate. (d): Consequently, the masking layer is not etched away everywhere. (e): SiRN is still present all around the molds at their bottoms.

graphy steps. Therefore an alternative method must be considered.

We suggest here to pattern the vertical sidewalls in two main steps, which are shown in Figure 4.7. Since it is impossible to illuminate the photoresist when it is masked by the thick upright part of the hinge, both parts of the hinges cannot be simultaneously patterned. The whole thick SiRN plate must be patterned first by wet etching before depositing the flexible part. In order to avoid an extra masking layer deposition and time-consuming wet etching step, the already patterned polySi layer by means of corner lithography, Figure 4.4-(h), can be used for this purpose. A short oxidation step is performed to form a $\simeq$ 5 nm SiO_2 layer on top of the polySi. A lithography follows to define the overall geometry of the foldable objects. SiO_2 is then patterned in three dimensions in wet etchant BHF. After stripping the photoresist, TMAH is used to pattern the underlying polySi using the SiO_2 layer as a mask, Figure 4.7-(b). The thick SiRN layer is then accessible and can be selectively etched, independently of the spatial direction.

After the conformal deposition of a thin SiRN layer (150 nm, Figure 4.7-(d)) followed by a polySi layer (100 nm), the exact same procedure can be applied again: short oxidation of polySi, second lithography using the same mask, patterning of oxide and polySi etching, Figure 4.7-(e). Wet etching of

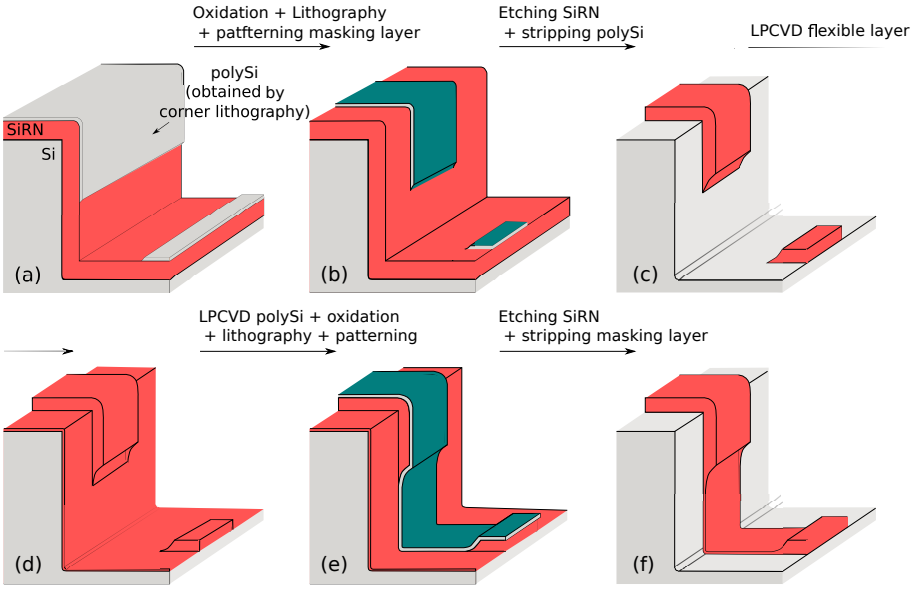

Figure 4.7 – Alternative steps to pattern upright sidewalls. (a): The thick SiRN should be patterned first. The polySi masking layer obtained thanks to corner lithography can be used. (b): A short oxidation step follows to form a thin SiO_2 layer. Unlike in Figure 4.6, lithography is possible to pattern the masking layer. (c): SiRN is wet etched using the oxidized polySi as a masking layer. PolySi is fully oxidized and stripped. (d): A flexible SiRN layer is deposited by LPCVD. (e): After LPCVD of a polySi layer followed by a short oxidation, the mask used in step (b) is applied a second time to pattern the masking layer. (f) SiRN is wet etched and the masking layer stripped. The origami patterns are now complete with no SiRN wire running anywhere around the mold as was the case in Figure 4.6.

thin SiRN and final stripping of masking polySi layer follow to complete the origami patterns, Figure 4.7-(f).

The use of wet etching induces that the SiRN layers are etched under the polySi masking layers. The structures will therefore be attacked twice from their sides, in steps (c) and (f) in Figure 4.7.

4.3 Results

4.3.1 Fabrication results—70.6° stop-programmable hinges

Figure 4.8 illustrates the design criterion introduced in Figure 4.3 and described in equation 4.2.2. By varying the oxidation time, two molds with different radii of curvature were made (Figure 4.4-(b)) and subjected to the

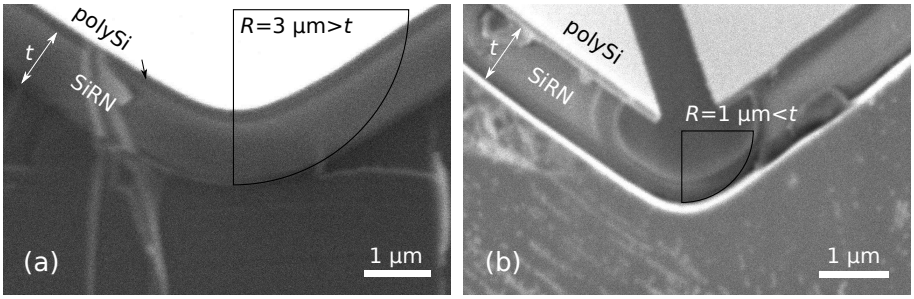

Figure 4.8 – Illustration of the design criterion described in Figure 4.3. Figs. (a) and (b) show samples with different radiis of curvature for the initial mold after performing corner lithography and partially etching the bottom SiRN layer, Figure 4.4-(i). The thickness t of the first deposited SiRN layer is 1.1 µm. (a): When $R > t$, the entire surface of the polySi layer was oxidized during step (f), consequently the retraction, step (g), had no effect. (b): For $R < t$, the polySi layer is opened and the underlying SiRN layer can be etched, Figure 4.4-(i).

exact same fabrication steps until the isotropic etching of the bottom SiRN layer (Figure 4.4-(i)). Since the thickness of the stack of the layers in the first case does not exceed R, there is no concave corner at the bottom of the groove. Consequently, the timed-etching step of the top SiRN layer (Figure 4.3-(f)) does not yield nanowires and the entire polySi layer is oxidized during the subsequent step (g). Without access points below the nanowires, no retraction can occur. Once the oxide is stripped, a non-patterned thick SiRN and polySi layer stack is obtained, as can be seen in Figure 4.8-(a).

In the correct case of Figure (b), the radius of curvature R is smaller than the thickness t of the SiRN layer. The entire etching procedure can proceed and yields a clear opening in the polySi layer through which SiRN can be etched.

Corner lithography is a powerful three-dimensional patterning technique. The trick works for concave corners of any size and spatial configuration. As an illustration, Figure 4.9 shows the result when starting from V-grooves made by anisotropic etching in KOH. The planes are organized in a well known fashion, and the use of corner lithography leads to retraction in all three dimensions.

Figure 4.10 gives an overview of the last fabrication steps of a tetrahedral pattern. The use of a thick photoresist developed for high aspect ratio features is necessary for good protection of the deep V-grooves during the dry etching of the SiRN features, Figure 4.4-(j). The result obtained with AZ® 9260 photoresist is good, as shown in photographs (a) and (b). Such planar protec-

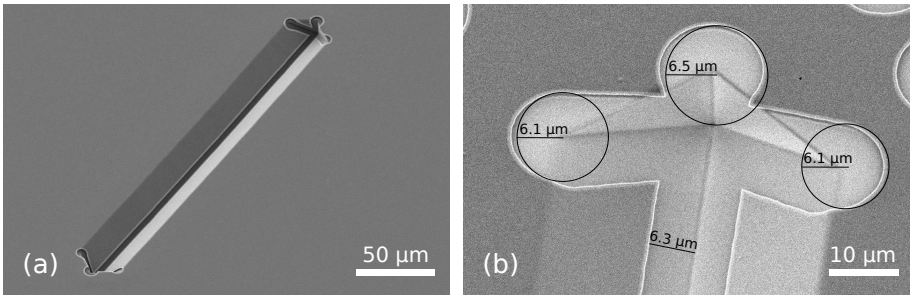

Figure 4.9 – (a): Overview of a V-groove after etching of the SiRN layer, Figure 4.4-(h). (b): Zoom in the extremity of the groove after stripping away the polySi top layer, Figure 4.4-(i). Retraction occurs in all concave corners, including the vertical planes. The retraction length is the same in every direction.

tion is obtained by coating and spinning the resist at 300 rpm for 10 s then 60 s at 2400 rpm. The resist is exposed three times for 10 s at intervals of 10 s and is developed for 7 min. As can be seen in the inset of picture (b), SiRN remains on the upright sidewalls after the dry etching step: only the top part was attacked by reactive ion etching. These small SiRN spots are, however, not a problem for our folding structures.

As is visible in pictures (a), (b) and (d), pinholes were present all over the wafer. They originate from nanoscopic defects in the bottom SiRN layer that turn into microscopic features because of the corner lithography: another proof of the extreme sensitivity of the technique. As long as the pinholes appear on the flaps and leave the hinges intact, they do not represent an issue for our folding purposes. However, the quality of the first SiRN layer should be checked at the beginning of the fabrication.

The stop-programmable hinge shown in Figure 4.10-(c) is nearly identical to the schematic presented in the process flow, Figure 4.4-(k), except for the small bumps visible at the transitions between the thin and the thick parts of the smart hinges. These transitions are called “bird’s beak” because of their characteristic shapes [111], and originate from the oxidation step necessary to remove the polySi layer between steps (h) and (i) in Figure 4.4.

A nearly released tetrahedral pattern is presented in Figure 4.10-(d). A circular protection of photoresist was present on top of it before the release step in SF_6, Figure 4.4-(k), hence the circular shape of the Si pillar.

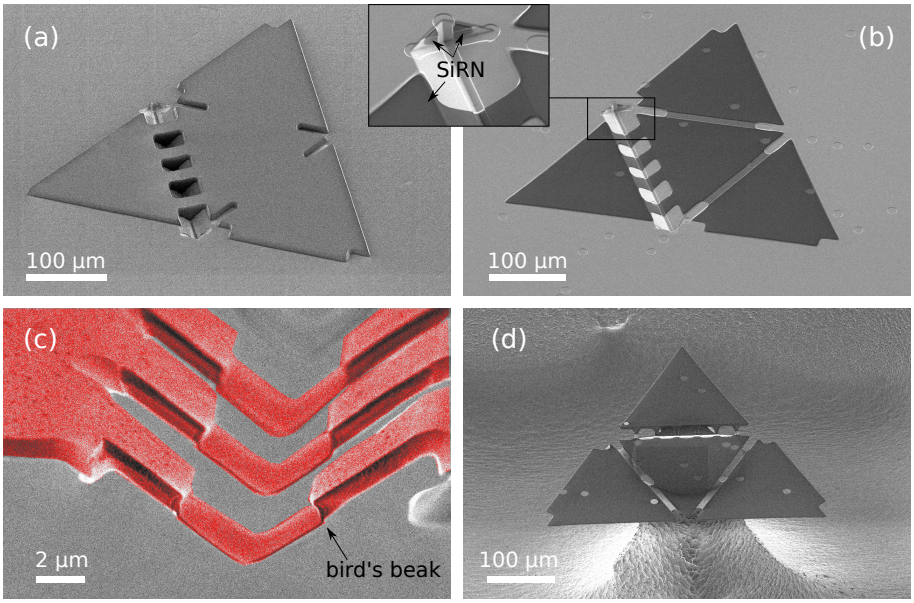

Figure 4.10 – SEM images of final fabrications steps. (a): Tetrahedral pattern of thick photoresist. (b): SiRN template after over-etching in the grooves and stripping of photoresist. The combination of a complex hinge with two flat hinges can be observed, see Figure 4.5-(a). (c): Close-up image of a complex hinge after the silicon mold was etched away in dry etching and the photoresist stripped, Figure 4.4-(k). (d): Overview of an unfolded tetrahedral structure at the end of the process. Isotropic etching of Si is stopped once the pattern comes to rest on a central pillar, Figure 4.5-(b). Note that this structure is not completely released, since Si is still present under the flaps.

4.3.2 Fabrication results—90° stop-programmable hinges

As was emphasized in Part 4.2.2, the fabrication for both stop-programmable hinges is identical except for the creation of the molds and for the final etching of the SiRN layers.

Our best results for getting molds using dry etching are presented in Figure 4.11. We used a mixture of SF_6 (200 sscm) and O_2 (15 sscm) gases at −110 °C (Adixen AMS100 Reactive Ion Etcher, pressure 1.6×10^{-2} mbar, RF 200 W, LF 20 W on/off time 25/75 ms). The dry etching step yields a rounded mold, picture (a), which reduces the oxidation time necessary to get the final desired radius of curvature. The depth of the molds was checked on six different spots spread over one dummy wafer and was found to be the same as that depicted in Figure 4.11 within an error of 5 %. Photograph (b) shows a similar mold on top of which the three layers necessary for corner lithography

were deposited, Figure 4.4-(d). Since the design criterion (equation 4.2.2) is respected, the rounding has disappeared after the conformal deposition of the first SiRN layer.

In Figure 4.11-(b), the defects of the initial mask can be observed on the vertical sidewalls. In order to avoid undesirable corner lithography starting points at that location, the over-etching of the top SiRN layer (Figure 4.4-(e)) was deliberately long. The corners formed due to irregularities of the mask have large opening angles, so the surplus of material is thinner than in the 90° corners at the bottom of the grooves. Since in a perpendicular corner the material is in theory 41 % thicker (see Figure4.2), a 25 % over-etch was performed.

Figure 4.12 shows the subsequent steps in fabricating 90° smart hinges. The successful retraction after the corner lithography is shown in photograph (a). Unlike the results presented in Figure4.9, no retraction occurred on the top or in the corners of the mold. This is a consequence of the long over-etching explained in the previous paragraph. This long over-etch of the top SiRN layer when performing corner lithography removed all unwanted material in the irregularities of the molds, as well as in their corners.

As explained in Part 4.2.2, dry etching cannot be used in the case of upright molds and a double wet etching strategy must be used. Figure 4.12-(b) shows the patterned masking layer, corresponding to step (b) in Figure 4.7. The oxidized polySi layer following the retraction shown in (a) was further shaped by oxidation and subsequent lithography steps. This way, the material at the bottom of the molds is etched and the geometry of folding patterns is defined simultaneously. Picture (c) shows the resulting structures after SiRN etching, with only the flexible part of the hinges missing, see Figure 4.7-(c). The same wet etching procedure is applied a second time after depositing a thin SiRN and polySi layer, resulting in the structures shown in photograph (d), Figure 4.7-(f). Misalignment of the mask in the second lithography step on top of the first patterned SiRN explains the staircase-like shape of the final SiRN object.

Figure 4.13 shows a self-foldable object released from the Si substrate, similar to the structure in Figure 4.12-(d). The fabrication was in principle successful, except for the fact that the length of the landing part of the complex hinge is extremely small in comparison with the flexible part, see Figure 4.1.

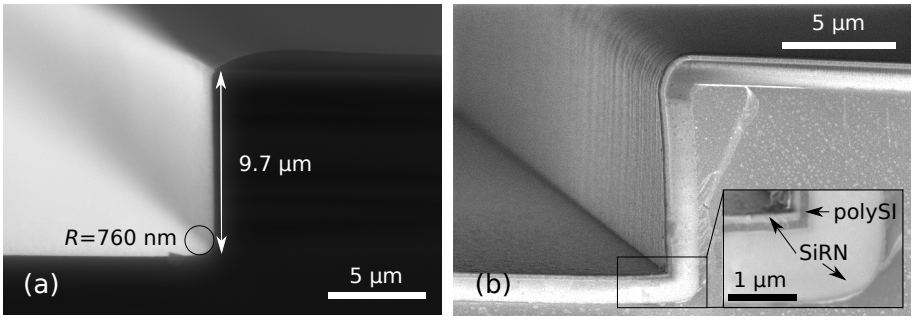

Figure 4.11 – (a): Cross section of a mold obtained by dry etching of silicon. The corner is not exactly perpendicular (measured to be 89°) and the process yields a round corner. These parameters can be modified by fine tuning the dry etching step. Note that photoresist is still present on top. (b): Stack of the three layers necessary for corner lithography: thick SiRN (1070 nm), polySi (around 150 nm) and a second layer of SiRN (146 nm).

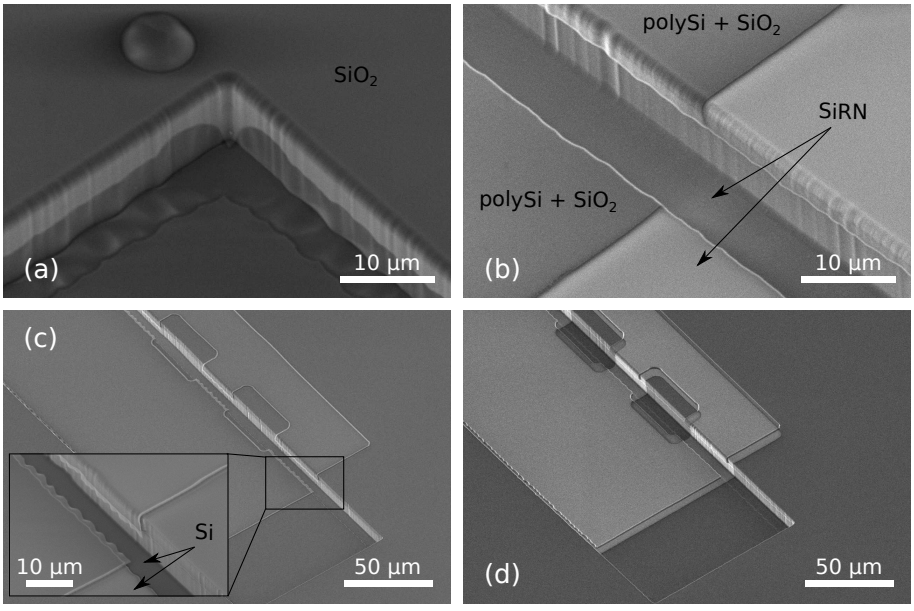

Figure 4.12 – SEM images of fabrication steps for 90° complex hinges. (a): Retraction of polySi is visible under SiO_2, Figure 4.4-(g). The polySi plate is not exactly straight. These irregularities are exact replicas of the defects of the silicon mold, which have been magnified through corner lithography. (b): Thick SiRN with patterned masking partially oxidized polySi layer on top. (c): Same as (b) right after wet etching of SiRN. Stress in SiO_2 mask causes the curtain-like overhanging thin film. (d): Final structure before release after the second wet etching procedure was applied.

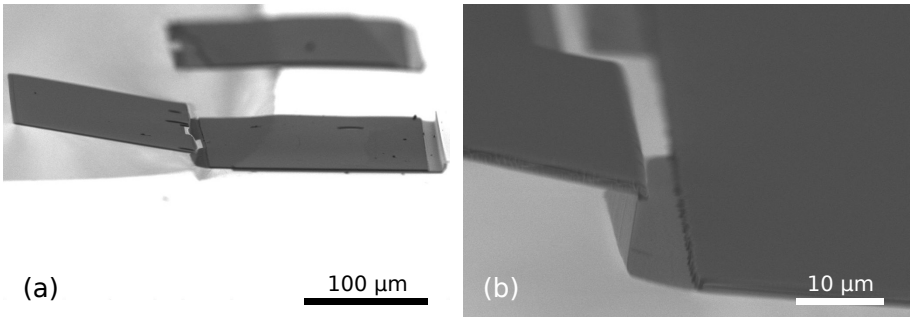

Figure 4.13 – (a): Final structure before folding. Residual stress in the thin SiRN layers provoked a slight bending upward of the flap. (b): Zoom in at a stop-programmable hinge.

4.3.3 Folding experiments

Self-folding experiments were carried out by manually depositing water droplets of 5 to 15 nL. An accurate positioning system allowed us to deposit the liquid right at the centre of the templates using a hollow fibre (50 µm diameter) connected to a high precision Hamilton glass syringe filled with ultra pure water that was manually actuated. The folding of the structures typically takes around one minute, depending on the size of the structures and the volume of liquid deposited.

Figure 4.14 shows the results of successful folding experiments. Figure (a) shows a wing folded at the designed angle of 70.6°. Figure (b) shows a tetrahedron resting on a silicon pillar. The large contact areas between the thick SiRN parts provide a good stability for the 3D objects after drying. The tetrahedral structure was folded from a similar pattern presented in Figure 4.5-(b) and Figure 4.10-(d). One stop-programmable hinge makes sure that the folding stops at 70.6° while large appendices designed on the side of the other faces allow them to lock onto the first flap.

Figure 4.15 shows the folding results when using 90° smart hinges presented in Figure 4.13. These results are less successful. A too long retraction of the polySi during the corner lithography, coupled with the wet etching steps necessary to pattern the final objects, led to wrongly shaped complex hinges. The thick parts of the hinges are too small, and the folding did not stop at all (a), or stopped too late (b). However, these results are encouraging and demonstrate that 90° stop-programmable hinges are feasible. Reducing the TMAH retraction to 2 µm, which would lead to 4 µm long flexible plates, would most

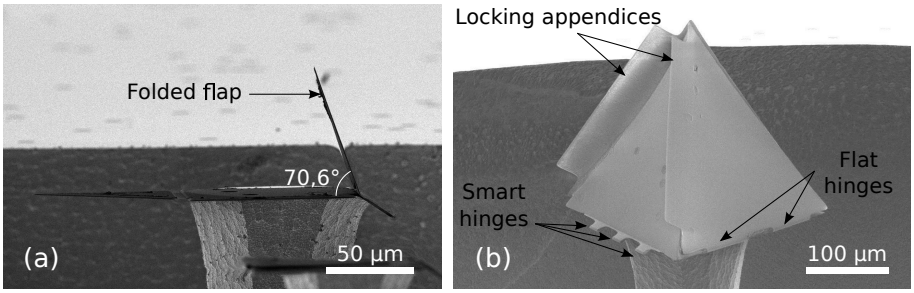

Figure 4.14 – Folded structure arrested by 70.6° stop-programmable hinges. (a): Side view of an extruded-2D structure. The flap is 100 µm wide and the complex hinge has an original width of 40 µm. The flap of the left hand side, connected with a flat hinge, reopened after folding because of an insufficient bonding area. (b): Folded tetrahedron. The faces have sides of 200 µm, the complex hinges are 20 µm wide and the flat hinges are 10 µm wide.

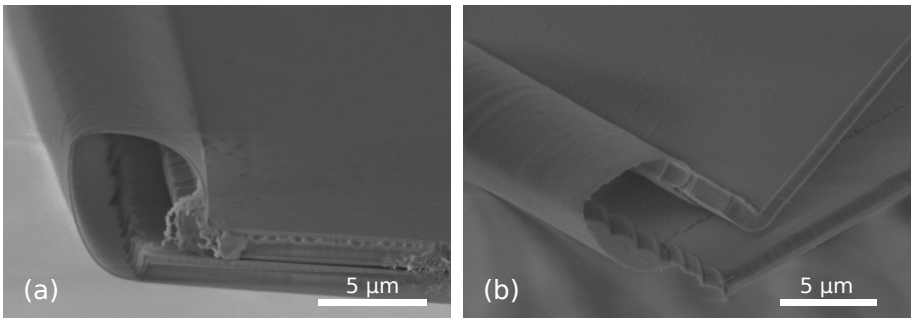

Figure 4.15 – Folding results of 90° stop-programmable hinges. (a): The thick part of the complex hinge is too short ((1.8 ± 0.2) µm) and fails to stop the folding. Consequently, the flap is 180° folded. (b): For this sample, the thick part is slightly longer ((3.2 ± 0.2) µm). This forces folding to stop at an intermediate position, but fails to stop the folding at 90° as was intended.

probably be sufficient for a successful assembly.

4.4 Discussion

The technique presented in this paper was first successfully used to fabricate 70.6° stop-programmable hinges. The same principle was then applied to upright molds, but issues were encountered during the process. Difficulties with the molds (retraction of the mask and roughness) caused our first attempt to fail. However, it became straightforward to perform corner lithography in 90° molds when a long over-etching was used. We initially used a 1.05 times

over-etching in the case of 70.6° stop-programmable hinges and increased it to 1.25 for 90° complex hinges. Later on during fabrication, difficulties in patterning upright sidewalls forced us to modify the process. Dry etching of SiRN with rotated samples, as well as a single wet etching step, were first unsuccessfully carried out before coming up with the appropriate two-step wet etching patterning strategy described here.

The results presented here are encouraging. As long as the necessary molds can be obtained in Si, the procedure that has been described in this paper is applicable to virtually any folding angle. In principle, the wet etching method for patterning SiRN onto the sidewalls should be applied for any mold opening angle $\alpha \leq 90°$, while dry etching should be preferred when $\alpha > 90°$.

Elastocapillary folding allows the assembly of relatively large structures. The characteristic capillary length, $\lambda_c = \sqrt{\gamma/\rho g}$ (here, γ is the surface tension, ρ is the density of the fluid, and g denotes the gravitational acceleration), gives an indication of the scale on which capillarity is dominant over gravity. For clean water and air at standard conditions, the transition is around 2 mm. Elastocapillary folding of several mm long silicon-based objects is therefore theoretically possible. It is known to be hard to fabricate features of this size out of the wafer plane by conventional two-dimensional micro-fabrication techniques. Indeed, 2 mm is more than four times the standard thickness of a standard silicon wafer. 90° stop-programmable hinges are especially interesting since they would permit popping up several mm long features out of the plane of the silicon wafers exactly where the hinges are designed. This technique, combining the strengths of well known standard fabrication techniques with the ease of self-folding, could have many applications, such as 3D sensing, Micro-Opto-Electro-Mechanical Systems (MOEMS), or 3D memory.

Furthermore, we have shown that the use of corner lithography leads to retraction in all three dimensions (Figure 4.9). For the purpose of self-folding, only the features at the bottom of the molds were used, the others being etched away in Figure 4.4-(j). Other features might be of interest for different purposes. For example, unique 3D membranes or channels could be obtained. Several applications have already been developed using corner lithography, such as the wafer scale fabrication of nano-apertures [106, 107], photonic crystals [104] or micro-cages in which the culture of bovine cells has been demonstrated [105].

4.5 Conclusion

Starting from a simple micrometer-sized mask, accurate stop-programmable hinges for complex elastocapillary folding were micro-machined in three dimensions using corner lithography. In order to limit the stress in the hinges while folding, it was necessary to start with round molds. Corner lithography can be performed only if the combined thicknesses of the two first deposited layers is greater than the radius of curvature of the mold. When this design criterion is respected, material can be accurately etched starting from any concave corner, independently of their spatial orientation.

The definition of the silicon molds at the start of the process determines both the locking angle and the accuracy of the stop-programmable hinges. Selective KOH etching on (110) wafers yields well defined sharp corners that, in turn, can be used to micro-machine smart hinges that stop folding at $(70.6 \pm 0.1)°$. Micrometer sized three dimensional tetrahedral structures were successfully self-folded using capillary forces, thanks to these hinges.

We demonstrated the feasibility of 90° stop-programmable hinges. Such complex hinges can be fabricated by making initial molds with dry etching at the cost of a poorer accuracy $(89 \pm 4)°$ compared to wet etching. Extra care must be taken when using dry etching to avoid any undesirable sharp corners, and a long over-etching during corner lithography must be performed to remove unwanted material. Moreover, small irregularities in the molds will be magnified by the process and will cause defects in the final shape of the flaps.

Stop-programmable hinges extend the possibilities for implementing the elasto-capillary folding of micro-structures. Using a simple filling procedure, millimeter-long silicon-based structures can be accurately popped out of the plane. We believe that the accuracy and versatility of the technique will find widespread application in 3D sensing, MOEMS, or 3D electronics, for instance.

5

Let's twist again!

5.1 Introduction

Phenomena encountered with elastic materials such as buckling, wrinkling or crumpling of thin sheets have been broadly researched and now offer comprehensive understanding [113–116]. Under control, these deformations offer reliable and efficient schemes to create functional shapes at small scales where standard micro-fabrication techniques have shown limitations [4, 5]. Eventually, using elastic deformations will lead to applications in flexible electronics [117, 118] or devices using graphene [119, 120] for instance.

Although the theoretical framework has been paved by Green decades ago [121], further investigation on twisted ribbons has only been achieved recently. Green showed that a ribbon under tension is subjected to non-uniform compressive stress, resulting in instabilities upon twisting. These results were later confirmed by numerical simulations [122, 123]. In the meantime, more interesting twisting-induced deformations were discovered, with transverse buckling and loop formations [124–127] or stress localization in the case of inextensible ribbons [128]. Chopin *et al.* finally offered a comprehensive view of these complex previously observed deformations [129, 130]. The authors showed that the distinct morphologies of twisted ribbons - helicoid, longitudinal and transverse buckling, creased helicoid and loop - are functions of applied tension and twisting angle and can be represented in a phase diagram.

In continuation of our work on elastocapillary folding [53, 64], we investigate in this effort the twisting and adhesion of pairs of ribbons under the action of surface forces. Such assemblies are carried out at both the micro and macro scale, as shown in Figure 5.1. Twisting of side by side micro-meter silicon nitride beams is carried out batch wise on silicon substrate, while similar assembly is carried out in the macro-meter scale using polyester ribbons. These two approaches allow us to investigate all parameters of assembly. The range of tension and twisting angle studied in this paper limit the ribbons

Manuscript in preparation for submission. Authors: A. Legrain, J. W. Berenschot, L. Abelmann, J. Bico and N. R. Tas.

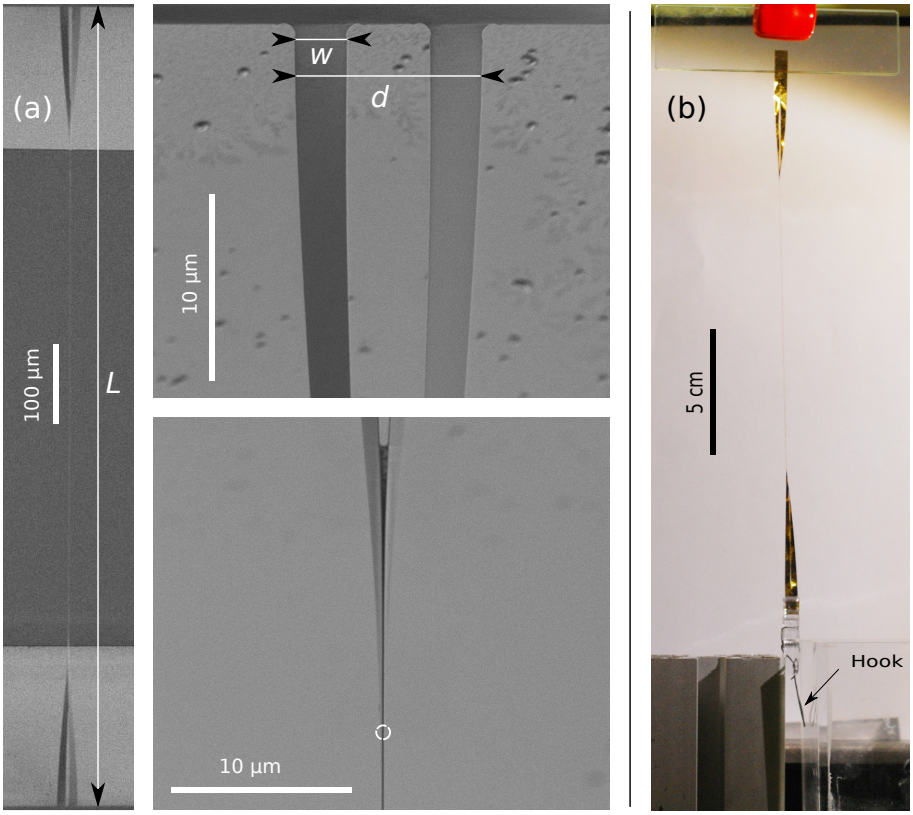

Figure 5.1 – Twisted ribbons. (a): SEM pictures of a millimeter long assembled pair of silicon nitride (SiRN) ribbons with zoom-in on extremities of the non-sticking part. The assembly is highly symmetric, and no deformation is observed at the anchors points. When rotated to 90°, the two SiRN beams fully adhere and form a single thin beam. The point at which the two ribbons completely adhere can be determined on SEM pictures with decent accuracy (white dot on the bottom right picture). (b): Macro-scale experiments setup. Two polyester ribbons are clamped on one side. A hook at the other end is used to apply tension using weights. The assembly is identical to microscopic ribbons.

morphology to helicoid shape, and creased helicoid in rare cases, see phase diagram in [129, 130]. A theoretical model is developed and compared to our experimental results.

5.2 Experimental section

5.2.1 Micro-ribbons

Fabrication and assembly

The fabrication of micrometer sized ribbons is sketched in Figure 5.2. The initial mask contains ribbons whose length L varies from 50 µm to 1 mm. For every length, all combinations of widths ($5 < w < 30\,\mu m$) and separations ($15 < d < 50\,\mu m$) were designed.

Made of low stress silicon rich nitride, the ribbons are released from the silicon substrate by anisotropic wet etching. Etched during 300 min in TMAH (25 wt%, 95 °C), ribbons of $t = (270.7 \pm 10.0)$ nm and $t = (107.0 \pm 7.5)$ nm were fabricated (initial thickness before etching $t = 300.0$ nm and $t = 124.6$ nm, respectively). The uncertainty in thicknesses are due to the fact that ribbons are also attacked from their bottom sides during an unknown amount of time, while thickness measurements by ellipsometry are carried out on planar, non-released parts.

After etching, the wafers were carefully placed in water for three days. One set of wafers of both thicknesses stayed in the same water for the entire period ("DI rinsing water"), while another set of wafers was placed in a new beaker of ultra pure millipore water every 24 h ("millipore water"). In the first case, the conductivity of water was measured using a commercial sensor to be $S = 157\,\mu S\,m^{-1}$ after three days of rising, while it was $S = 1.5\,\mu S\,m^{-1}$ when water was changed every other day. After assembly the ribbons were observed and characterized by SEM.

Residual stress measurement

Residual stress in the silicon rich nitride layer (SiRN) was measured using the wafer curvature method. The curvature of a dummy wafer is measured before and after deposition of the thin film by means of a surface profiler. The stress is estimated using the Stoney equation [68]. In the case of silicon nitride, one side of the wafer is stripped before measuring the radius of curvature since material is deposited on both sides of wafers by LPCVD. The thickness of substrates is measured using a dedicated tool (Heidenhain measuring station). For the Young's modulus and Poisson's ratios we used literature values of $E_{SiRN} = 290$ GPa and $\nu = 0.27$, respectively.

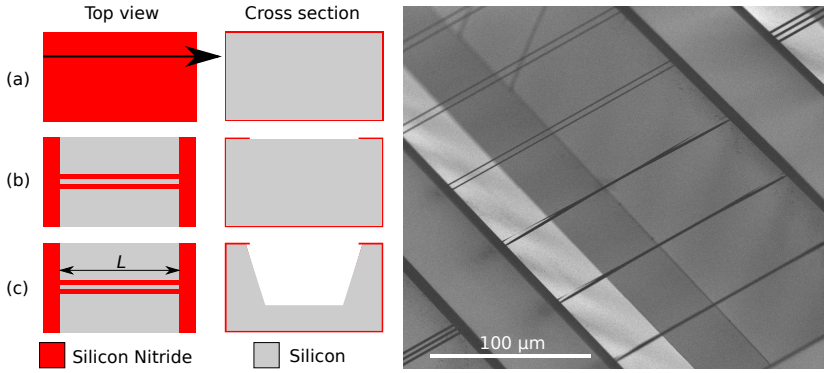

Figure 5.2 – Fabrication process of microscopic ribbons. (a): A conformal layer of SiRN is deposited on top of a silicon wafer by LPCVD. (b): Patterning of SiRN by dry etching. (c): Using SiRN as a masking layer, silicon is etched in anisotropic wet etchant and the wires are released from the substrate. After etching the wafers are placed in water during three days. The assembly takes place after letting the wafer dry in open air. Length L, width w and spacing d of the ribbons are parameters than can be tuned on the initial mask. Right hand side SEM picture: resulting structures, top view. Three pairs of ribbons are not assembled on top of the picture, the three next are.

5.2.2 Macro-ribbons

Millimeter size ribbons were cut in biaxially-oriented polyethylene terephthalate (BoPET, also known as Mylar) sheets either by a laser cutter or manually using a scalpel. The laser cutter tool burns a little material, resulting in a decrease of width w by approximatively 50 µm. An increase of the thickness t with approximatively 5 µm was observed at the edge of the ribbons using a surface profiler. The scalpel yields cleaner ribbon profiles, with a cutting space between ribbons below 10 µm and no increase of thickness.

Assembly was carried out in ambient conditions using the set-up shown in Figure 5.1 with ribbons clamped on one side. The wetting liquid, silicone oil of surface tension $\gamma_{\text{oil}} = (21.0 \pm 0.5)\,\text{mN/m}$, was manually delivered using a syringe. Silicone oil was preferred over water because of a much slower evaporation rate. The assembly was forced by bringing the top sides of the ribbons together. Different tensions were applied by placing weights on a hook at one end of the ribbons. Weights from 1.11 g to 57.14 g were used, resulting in stresses in individual ribbons σ_{BoPET} in the range 0.20 MPa to 20 MPa depending on the cross section of the beams. Photographs of the assembly were analyzed using the software ImageJ.

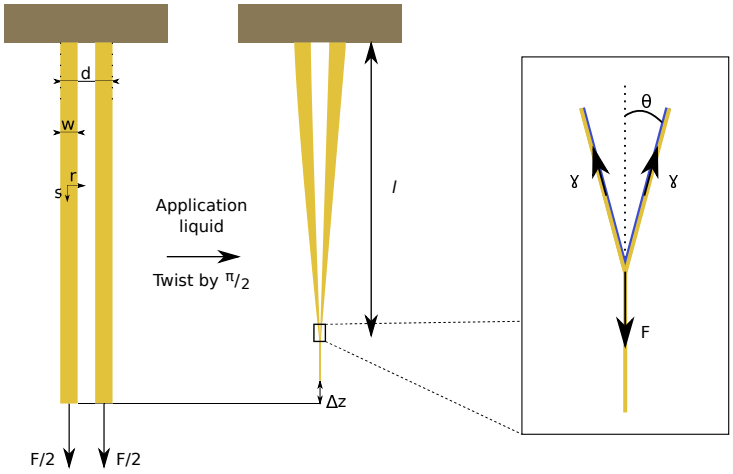

Figure 5.3 – Model parameters. w is the width of the ribbons, d the distance from one outer edge to the other. The total length of the ribbons is L. l represents the opening - non sticking part - after assembly, resulting in the opening angle θ.

The elasticity of the used BoPET films was determined to be $E_{\mathrm{BoPET}} = (4.6 \pm 0.5)\,\mathrm{GPa}$, at an estimated thickness $t = (13.5 \pm 1.4)\,\mu\mathrm{m}$ by means of three methods. In the first place we used tensile testing, which determines the value of Et. Next, we used elastocapillary testing which yields the value of Et^3. During this test two extremities of a band are brought together under the action of capillary forces, the size measurement of the formed loop yields Et^3 [24]. The same value was finally confirmed by flexural testing.

5.3 Theory

In this section we introduce a theoretical model used to predict the outcome of the assembly. Figure 5.3 shows the parameters used for modeling. We tackle the rather complex deformation by considering two simplified cases based on simple twist and lateral displacement, respectively.

5.3.1 Simple twist

We consider the simple case of a single ribbon twisted along a length l by an angle α. The main component of stress is along the longitudinal direction as

derived by Green [121], using dimensionless parameters:

$$\bar{\sigma}_{ss}(\bar{r}) = \frac{\bar{T}}{2} + \frac{\eta^2}{2}(\bar{r}^2 - 1/12) \tag{5.3.1}$$

with $\bar{\sigma} = \sigma/E$, $\bar{T}/2 = F/2Etw$ the normalized tension and $eta = \alpha w/l$ the twisting angle. $\bar{r} = r/w$ is the normalized transverse material coordinate. The subscripts ss indicate that the stress acts on a plane normal to the s axis and in the direction s (Cauchy stress tensor). There is also a transverse component of stress but of small magnitude with $\bar{\sigma}_{rr}(\bar{r}) \sim \eta^2 \bar{\sigma}_{ss}(\bar{r})$ and can therefore be neglected [130]. The resulting energy is:

$$U = \frac{1}{2} Ewlt \int_{-1/2}^{1/2} \bar{\sigma}_{ss}^2(\bar{r})\, \mathrm{d}\bar{r} \tag{5.3.2}$$

Before twisting the initial elastic energy stored in the ribbon due to the tension equals $1/4Etwl\bar{T}^2$. Integrating equation 5.3.2 and subtracting the initial energy gives the twist energy:

$$U_{tw} = \frac{1}{1440} Etwl\eta^4 = \frac{1}{1440} \frac{Etw^5}{l^3} \alpha^4 \tag{5.3.3}$$

5.3.2 Lateral displacement

We now consider the displacement and adhesion of two ribbons facing each other under the action of surface tension. The strips are separated by a distance d and are submitted to a load $F/2$. As long as F is strong enough, the work due to the tension is much bigger than the bending energy and the bending stiffness can be neglected. Therefore the ribbons form a Y shape as shown in Figure 5.3.

In terms of energies, as the two ribbons adhere the tension F works over a distance Δz while a liquid/air area is suppressed along a length $(L - l/\cos\theta)$:

$$U_{ld} = F\Delta z - 2\gamma_a w(L - \frac{l}{\cos\theta}) \tag{5.3.4}$$

with γ_a the adhesion surface energy, which may differ from γ_{liquid} when the wetting liquid evaporates as will be discussed in the results part. Since L is

constant we can forget the resulting term. Simple geometry gives:

$$l = \frac{d}{2\tan\theta} \tag{5.3.5}$$

$$\Delta z = l\left(\frac{1}{\cos\theta} - 1\right) = d\frac{1-\cos\theta}{2\sin\theta} \tag{5.3.6}$$

Thus equation 5.3.4 becomes:

$$U_{\mathrm{ld}} = Fd\frac{1-\cos\theta}{2\sin\theta} + \gamma_{\mathrm{a}} wd\frac{1}{\sin\theta} \tag{5.3.7}$$

5.3.3 Theoretical opening l

Two ribbons are twisted by an angle $\alpha = \pi/2$ in our case, leading to the twist energy:

$$U_{\mathrm{tw}} = \frac{2}{1440}Etw\left(\frac{\pi}{2}\right)^4\frac{w^4}{l^3} = \frac{\pi^4}{1440}Etwd\left(\frac{w}{d}\right)^4\sin^3\theta \tag{5.3.8}$$

Adding equation 5.3.7 to equation 5.3.8 gives the total energy of the system:

$$\begin{aligned} U_{\mathrm{total}} &= \frac{\pi^4}{1440}Etwd\left(\frac{w}{d}\right)^4\sin^3\theta + Fd\frac{1-\cos\theta}{2\sin\theta} + \gamma_{\mathrm{a}} wd\frac{1}{\sin\theta} \\ \frac{U_{\mathrm{total}}}{Etwd} &= \frac{\pi^4}{1440}\frac{\sin^3\theta}{\beta^4} + \frac{F}{Etw}\frac{1-\cos\theta}{2\sin\theta} + \frac{\gamma_{\mathrm{a}}}{Et}\frac{1}{\sin\theta} \end{aligned} \tag{5.3.9}$$

Where we find the normalized tension $\bar{T} = F/Etw$. Moreover, we introduced the non-dimensional distance $\beta = d/w \geqslant 2$. Minimizing the energy with respect to opening angle θ finally leads to:

$$\begin{aligned} \frac{\partial U_{\mathrm{total}}}{\partial\theta} = 0 \;\rightarrow\; & \frac{3\pi^4}{1440}\frac{\sin^2\theta\cos\theta}{\beta^4} + \bar{T}\frac{1-\cos\theta}{2\sin^2\theta} - \frac{\gamma_{\mathrm{a}}}{Et}\frac{\cos\theta}{\sin^2\theta} = 0 \\ & \frac{\pi^4}{240}\frac{(1-\cos^2\theta)^2\cos\theta}{\beta^4} + \bar{T}(1-\cos\theta) - \frac{2\gamma_{\mathrm{a}}}{Et}\cos\theta = 0 \end{aligned} \tag{5.3.10}$$

Equation 5.3.10 can be readily numerically solved for θ. The theoretical opening l is then obtained using equation 5.3.6.

During experiments we always observed a small angle, $\theta < 0.1$. A small angle approximation of equation 5.3.10 results in:

$$\frac{\pi^4}{240\beta^4}\theta^4 + \frac{\bar{T}}{2}\theta^2 - \frac{2\gamma_a}{Et} = 0 \tag{5.3.11}$$

Equation 5.3.11 is quadratic and has an analytical solution in θ^2.

$$\begin{cases} A = \dfrac{\pi^4}{240\beta^4} \\ B = \dfrac{\bar{T}}{2} \\ C = -\dfrac{2\gamma_a}{Et} \end{cases} \tag{5.3.12}$$

With an always positive discriminant:

$$\Delta = B^2 - 4AC = \frac{1}{4}\left(\bar{T^2} + \frac{2\pi^4\gamma_a}{15\beta^4 Et}\right) > 0 \tag{5.3.13}$$

Therefore equation 5.3.11 has only one positive root and we get:

$$\theta = \frac{2\beta^2}{\pi^2}\sqrt{15(2\sqrt{\Delta} - \bar{T})} \tag{5.3.14}$$

For reasonable parameters ($\beta = 2$, $\bar{T} = 4\times10^{-4}$, $\gamma_a = 72\,\mathrm{mN/m}$, $Et = 3\times10^4\,\mathrm{N\,m^{-1}}$) equation 5.3.14 is a good approximation of equation 5.3.10 with a relative error <0.1 % for $\theta < 0.1$.

5.3.4 Tension in micro-ribbons

With macro-meter ribbons the stress is constant and is set by the weights attached to the hook. There is no stress induced by deformation since the free extremities of the ribbons can move up and down. In the case of micro-experiments however, the ribbons are clamped and the deformation induces stress which adds to the residual stress $\sigma_{\text{r-SiRN}}$ already present in the thin layer, see part 5.2.1. The induced stress equals:

$$\sigma_{\text{induced}} = E_{\text{SiN}}\frac{2\Delta z}{L} = E_{\text{SiN}}\frac{d}{L}\frac{1-\cos\theta}{\sin\theta} \tag{5.3.15}$$

Both stresses are of the same order of magnitude, MPa, and they consequently both need to be taken in account. The tension $\bar{T}$ becomes a function of θ:

$$\bar{T} = \frac{2\sigma_{\text{r-SiN}}}{E_{\text{SiN}}} + \frac{2\sigma_{\text{induced}}}{E_{\text{SiN}}} = \frac{2\sigma_{\text{r-SiN}}}{E_{\text{SiN}}} + \frac{2d}{L}\frac{1-\cos\theta}{\sin\theta} \tag{5.3.16}$$

For this definition of $\bar{T}$ equation 5.3.10 cannot be numerically solved any-

more. When considering small angles, equation 5.3.11 becomes:

$$\frac{\pi^4}{240\beta^4}\theta^4 + \left(\frac{2\sigma_{\text{r-SiN}}}{E_{\text{SiN}}} + \frac{d}{L}\theta\right)\frac{\theta^2}{2} - \frac{2\gamma_a}{Et} = 0 \tag{5.3.17}$$

which has no direct analytical solution but can readily be numerically solved. When compared to equation 5.3.10, this small angle approximation shows a relative error $< 0.2\,\%$ as long as $\theta < 0.1$, which is always the case in our experiments.

5.3.5 Relevance of the model

It is interesting to compare the macro and micro ribbon assemblies. There aspects ratios are equivalent with $w/t \sim 10^2$. Moreover, the non-dimensional stress is comparable in both cases, with $\bar{T} \sim 10^{-3}$. The crucial parameters of the macro and micro-assemblies are in the same range, and results should therefore be comparable.

The theory described above is applicable to both scales, although for small tension the bending stiffness becomes significant. This occurs when the opening l becomes comparable to $\sqrt{d}(E_{\text{BoPET}}t^3/\gamma_{\text{oil}})^{1/4} = 0.15\sqrt{d}$. For macro-ribbons, we expect deviation from the model below $l = 1\,\text{cm}$ at $d = 4\,\text{mm}$. For micrometer ribbons, the limit shifts down to $\sqrt{d}(E_{\text{SiRN}}t^3/\gamma_{\text{a}})^{1/4} \sim 1\times10^{-2}\sqrt{d}$. This length is small compared to opening lengths that we observe experimentally, so bending stiffness can be neglected.

5.4 Results and discussions

5.4.1 Macroscopic experiments

The tension (stress) applied on the ribbons can easily be tuned using the macroscopic setup shown in Figure 5.1 as described in section 5.2.2. Figure 5.4 shows the opening length l as a function of applied stress $F/2wh$. We converted the total applied force to stress in each individual ribbon to enable comparison with the micro-ribbons (hence the factor $1/2$). We also assume that $\gamma_{\text{a}} = \gamma_{\text{oil}}$, since silicone oil barely evaporates and a liquid layer is always present. The opening is independent of the total length L. This result is in agreement with the model, equation 5.3.10. The best fit is achieved for the geometrical parameter $\beta = d/w = 2.05$, which is in agreement with the gap between ribbons induced by laser cutting, see part 5.2.2. This implies that the outer edges of

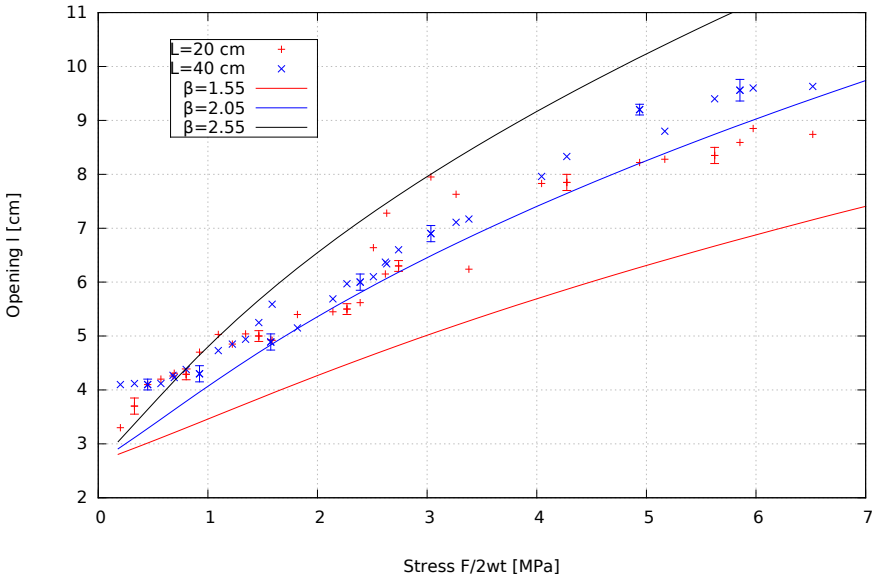

Figure 5.4 – Macroscopic experiment, assembly of identical pair of polyester ribbons The width w=(1.9 ± 0.1) mm and distance d=(3.9 ± 0.2) mm are defined by laser cutting. The constraint is applied by weights placed on a hook at one end, see Figure 5.1-(b). Within measurements errors, the length of the ribbons L does not have an impact on the assembly. Solid lines: theory for different geometrical parameters $\beta = d/w$ obtained using equation 5.3.10.

the ribbons must be taken as starting points for the displacement, as pictured in Figure 5.1 and 5.3. This result may seem counter-intuitive, since a ribbon is perfectly centered after twisting. On the other hand, the model should still be valid in the limit of an infinitely thin ribbon ($t \to 0$). In that case the twisting energy becomes zero and we can approximate the ribbons as wires. Quite naturally, one should take d from outer to outer edge, in order not to underestimate the displacement energy.

In Figure 5.4 we also observe that the model tends to underestimate the opening for small stresses. Like discussed in the theory section 5.3.5, for small tensions the bending stiffness can no longer be neglected for $l \simeq 1$ cm, which was indeed the case.

For very small tension the helicoid shape of ribbons turned into creased helicoid, which is consistent with observations from literature [129, 130]. When the twist is sufficiently large with respect to tension, stress becomes compressive in the longitudinal direction (equation 5.3.1) in a zone around

the centerline. Edges are then extended with respect to the centerline, which creates facets in the helicoid shape.

Figure 5.5 shows the opening l for different widths. In graph (a) we observe that for a same length and spacing the opening increases with width and increases with stress. In graph (b) the same data is normalized for easier comparison with the model. The data collapses on the $\beta = 2$ curve, which was also the case in Figure 5.4. Note that we use in this graph $\beta = 2$ instead of 2.05 since these ribbons were manually cut using a scalpel resulting in a negligible gap between them, see experimental section 5.2.2. For small tension the model again underestimates the opening when bending stiffness is no longer negligible. In the case of large w, the model seems to overestimate the opening for $\bar{T}$ <0.0001. When the tension is small the ribbons start to buckle and it is difficult to estimate the opening.

Figure 5.6 shows the opening versus the width at constant tension $\bar{T} = (1.05 \pm 0.15) \times 10^{-3}$. The data is identical to that of Figure 5.5. Since we used the same weights for our experiments and the tension depends on the cross sections of each ribbon, it varies slightly between widths. The opening l is linearly dependent with the width w, so the opening angle θ is constant (equation 5.3.6). The model fits well with the experimental data within measurement uncertainty. It seems that our simple model, that considers twist and displacement independently, adequately described the macro-assembly experiment.

5.4.2 Microscopic experiments

Pair of ribbons

Contrary to macro-experiments, the tension in the micro-ribbons cannot be manually applied. There is however tension induced by deformation and due to the deposition of SiRN, see part 5.3.4. This residual stress was measured using the wafer curvature method, see experimental section 5.2.1. A tensile stress of $\sigma_{\text{r-SiRN}} = (169 \pm 25)$MPa was measured in a layer deposited on the same day in the same LPCVD equipment as the wafers of the experiment, but in a different run.

Figure 5.7 shows an example of batch folding of micro-ribbons. This top view of a silicon trench, see Figure 5.2, illustrates the nearly linear dependence of the opening length l on the separation d between ribbons. This observation is confirmed in Figure 5.8 for two different thicknesses t. The

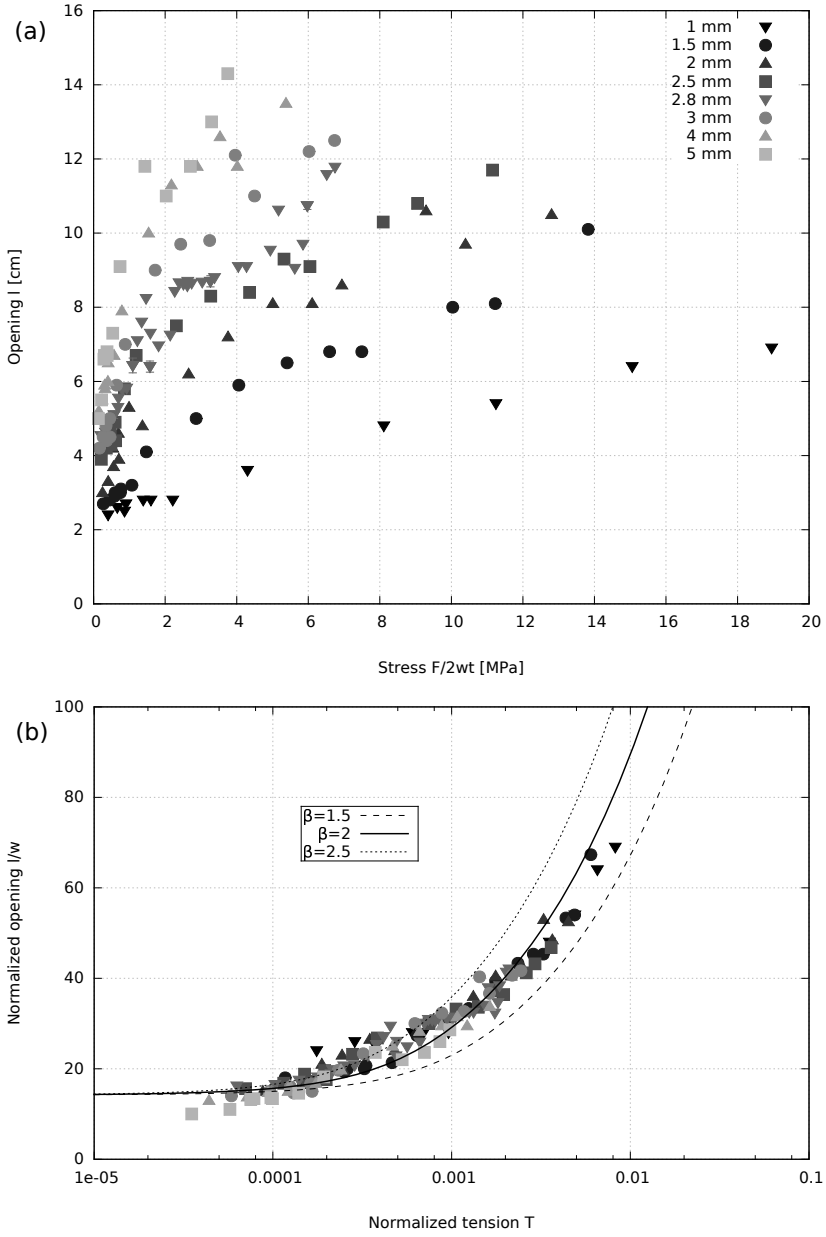

Figure 5.5 – Macroscopic experiment, assembly of pair of polyester ribbons with different widths w ($L = 40\,\text{cm}$, bands cut by cutter except for $w = 2.8\,\text{mm}$). The constraint is applied by weights placed on a hook at one end, see Figure 5.1-(b). (a): Raw data. On average, the opening increases with ribbon width. (b): Normalized values and comparison to theory, equation 5.3.10. The data collapses on the $\beta = 2$ theoretical curve.

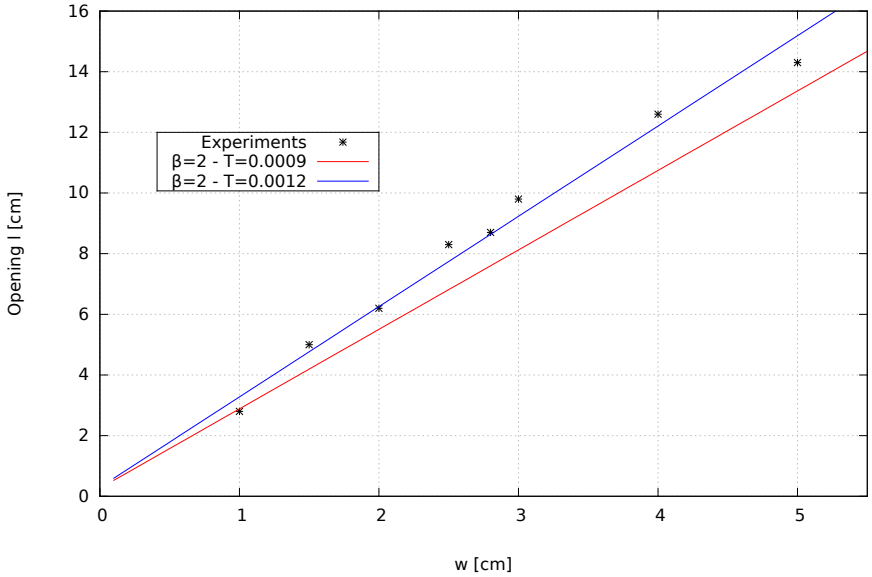

Figure 5.6 – Macroscopic experiment, assembly of pair of polyester ribbons with different widths w at nearly constant constraint $\bar{T} = (1.05 \pm 0.15) \times 10^{-3}$. The opening is linearly dependent with the width w. The solid lines show theoretical prediction for the two extrema of $\bar{T}$ obtained using equation 5.3.10. The data plotted here is the same as Figure 5.5. Because of different cross sections, the normalized tension is slightly different for every width.

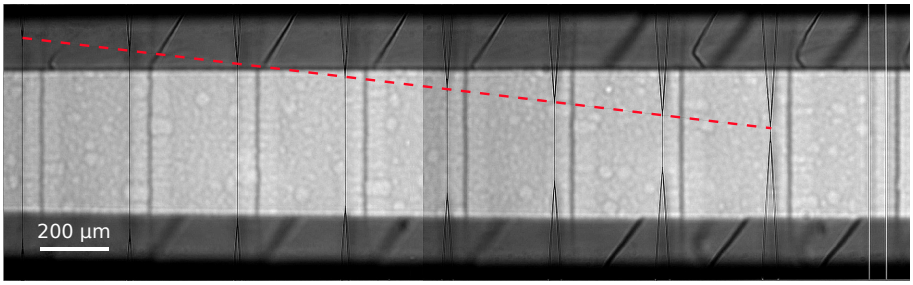

Figure 5.7 – Optical image of an array of $L = 800\,\mu m$ long pair of ribbons after assembly. Ribbons are $w = 5\,\mu m$ wide and $t = 107\,nm$ thick. The first pair (left hand-side) is $5\,\mu m$ apart ($d = 15\,\mu m$), and the separation increases by $5\,\mu m$ for every new group. The red dashed line connects the attachments points of the beams: the adhesion length approximately linearly decreases as the ribbons move further apart. The last pair of ribbons is too far apart to remain assembled.

opening l increases with t since the twisting energy is proportional to t, see equation 5.3.3. Comparison to our theoretical model in Figure 5.8 shows that the opening length can be estimated within 30 % error when assuming $\gamma_a = \gamma_{liquid} = 72\,mN\,m^{-1}$. The model does not represent the trends well. Our model does not capture the three-dimensional aspects of the assembly, especially for the induced stress, equation 5.3.4, that seems to be over-estimated here. Moreover the surface energy is likely to be different. Contrary to silicone oil in the case of macro-experiments, the water evaporates when the wafers are in open air. During experiments we observed that initially assembled pairs of ribbons reopened after drying, which is sign of two distinct adhesion energies during assembly and in the final state. The adhesion energy between the two SiRN beams is determined by a thin layer of water, always present on hydrophilic surface such as SiRN, in combination with debris remaining after the long etching procedure, see experimental part 5.2.1. These stiction conditions, known as liquid bridging and solid bridging, are knowingly hard to measure [131–133]. Further research is necessary to completely understand the impact of solid bridging on our assembly.

Figure 5.8 also shows the impact of the quality of water in the assembly. We see that stiffer pairs of ribbons remain assembled in the case of less clean DI rinsing water (conductivity $S = 157\,\mu S\,m^{-1}$), whereas they detach in millipore water ($S = 1.5\,\mu S\,m^{-1}$). This is consistent with an increase in stiction because of etching residues, as reported in literature [131–133].

For micro-ribbons the theory shows that stiffening due to deformation is significant. Therefore the theoretical opening length is a function of L, equation 5.3.17, as seen in Figure 5.9. The experiments seem to endorse this observation, although results from $t = 270\,nm$ are not conclusive. Moreover, the model underestimates the opening in the case of $t = 270\,nm$ while it overestimates for $t = 107\,nm$. We speculate that it is due to a different surface adhesion energy, γ_a, which can differ from one wafer to another. Uncertainties in thickness, stress and material properties are also sources of errors.

In the case of macro-ribbons the opening was proportional to the width, as was predicted by the model (Figure5.6). For micro-ribbons however, the induced stress increases with w since d depends on w. Therefore the opening l increases as well, as can be seen in the theoretical curve of Figure 5.10. The measurements seem to support the theoretical trend.

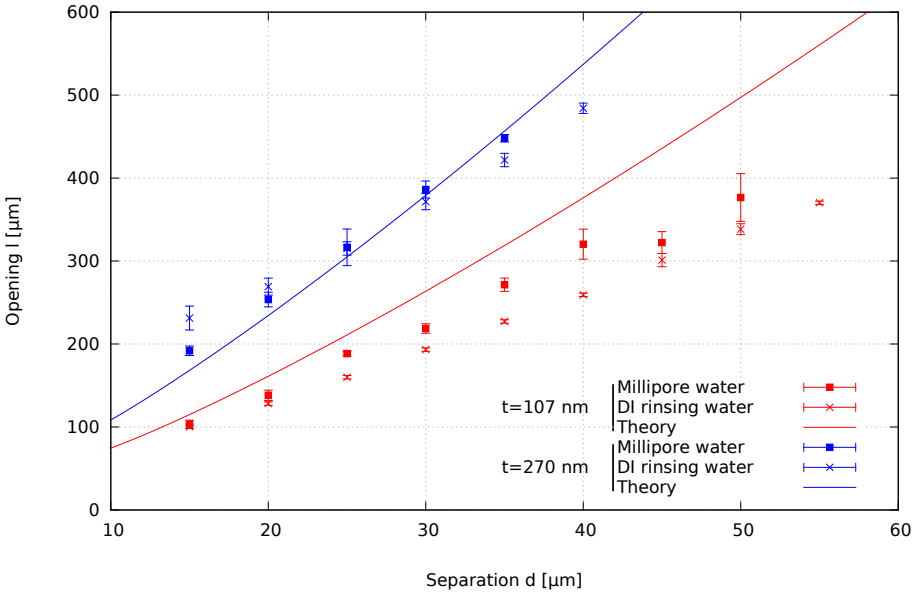

Figure 5.8 – Opening at the extremities versus separation of the ribbons. The length as well as the width of the ribbons are constant, $L = 1000\,\mu m$ and $w = 5\,\mu m$, respectively. Average values and standard deviation were calculated from measurements on SEM pictures from 5 identical set of structures present on the same wafer. One wafer was used for each thickness t. Theoretical lines are obtained using equation 5.3.17 with $\gamma_a = \gamma_{liquid} = 72\,mN\,m^{-1}$.

Freak show

Along with pair of ribbons, more complicated designs were tried out in an attempt to frustrate the folding of the ribbons. Figure 5.11 shows an example of two groups of six equally spaced ribbons. Interestingly, the beams do not attach by two, as observed with simple pairs, but seem to assemble in a random fashion. Overall, twisting does not seem to be a preferable configuration, since ribbons tend to overlap rather than rotate. Such a configuration with beams on top of each other or sticking along their sides was never observed with single pairs of ribbons. These complex configurations are probably due to the presence of two menisci on both sides of the beams during assembly.

We observe a similar behavior when ribbons are designed in a circular manner, as shown in Figure 5.12. The central plate is broken, either because of residual stress or bubble formation during anisotropic etching of silicon. Despite this, all ribbons overlap and the opening l is constant when ribbons assemble by two. Half of the wheel is intact in Figure 5.12-(b) and overlapping

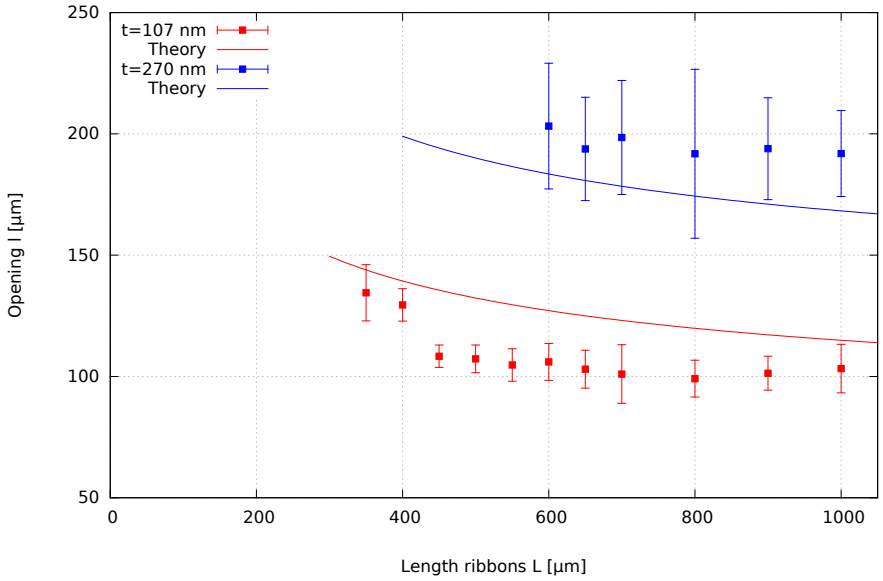

Figure 5.9 – Opening at the extremities versus length of the ribbons, assembly in millipore water. The width of the ribbons and the distance between them are constant, $w = 5\,\mu m$, $d = 15\,\mu m$. Average values and standard deviation were calculated from measurements on SEM pictures from 5 identical set of structures present on the same wafer. One wafer was used for each thicknesses. Theoretical lines are obtained using equation 5.3.17 with $\gamma_a = \gamma_{liquid} = 72\,mN\,m^{-1}$.

is random and nearly identical. This apparently random behavior could be used to generate unique signatures for MEMS devices.

Figure 5.13 shows examples of self-folding of ribbons with flaps. These flaps increase the adhesion surface, resulting in assembly of short ribbons that would not attach without the flaps, as shown for instance in Figure 5.13-(b). The flaps also avoid translation of the beams, resulting in a high twisting angle ($\sim 120°$ in Figure 5.13-(c)). This flap configuration is only one example of many design possibilities. Thickness, shape and number of flaps for instance can be modified. For application, we envision that channels or wires could be fabricated on top of the flaps, resulting in out of plane sensors or channel networks.

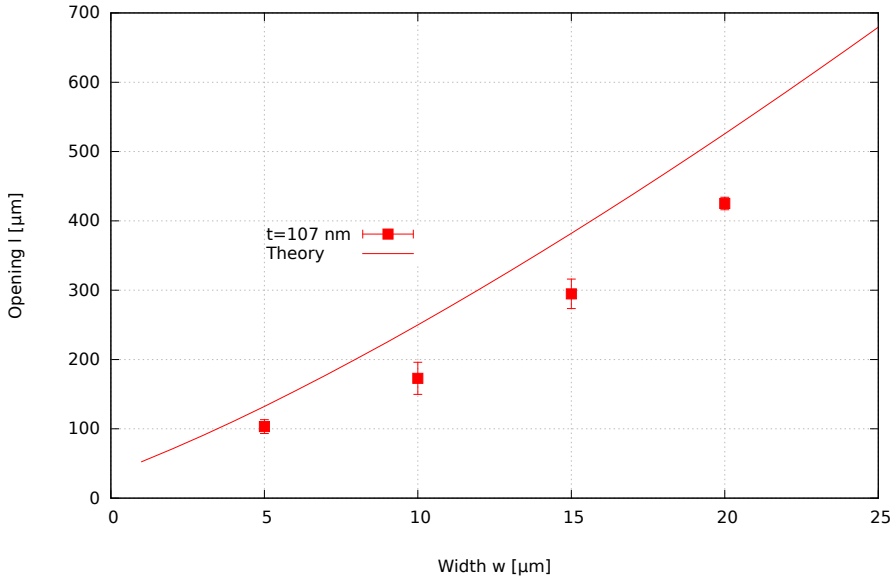

Figure 5.10 – Opening at the extremities versus width of the ribbons, after assembly in millipore water. The length is constant, $L = 1000\,\mu m$. The gap between the ribbons is $5\,\mu m$, therefore $d = 2w + 5\,\mu m$. Average values and standard deviation were calculated from measurements on SEM pictures from 5 identical set of structures present on the same wafer. Theoretical lines are obtained using equation 5.3.17 with $\gamma_a = \gamma_{liquid} = 72\,mN\,m^{-1}$.

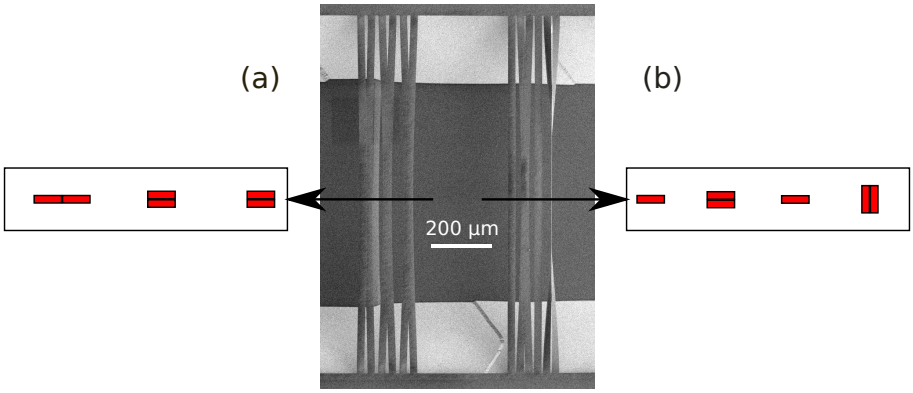

Figure 5.11 – Example of a group of 6 ribbons, width $w = 20\,\mu m$ and thickness $t = 107\,nm$. The ribbons are spaced by $d = 15\,\mu m$ in group (a) while spacing is $d = 20\,\mu m$ in group (b). Cross sections on both sides clarify the configurations. Ribbons assemble by two in group (a) but do not twist and simply stick on their sides or overlap. Assembly seems random in group (b) with one overlapping group, two unmoved ribbons and a twisted group.

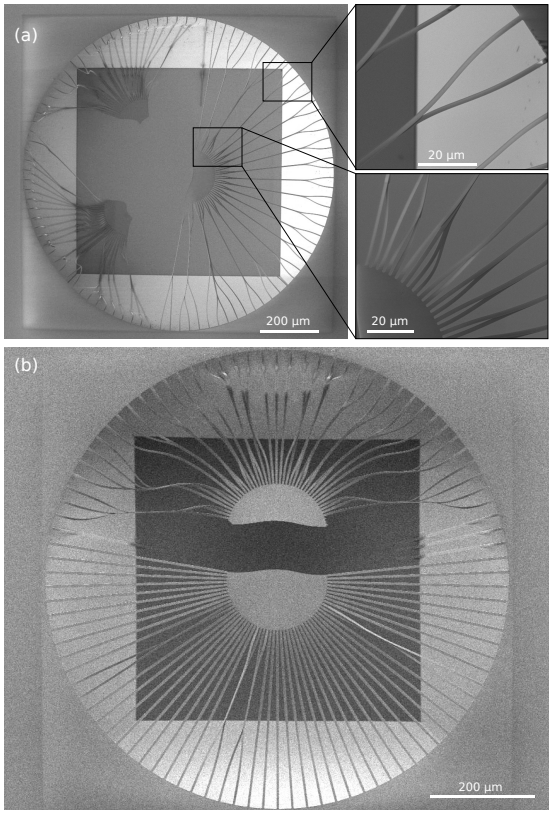

Figure 5.12 – Wheel configuration of thin ribbons, thickness $t = 270\,\text{nm}$. Despite the breaking of the wheels during etching, when two ribbons assemble the opening seems regular. Overlapping of the ribbons is preferred over twisting. Picture (b) shows a wheel with a random assembly of pairs of ribbons. A MEMS random generator structures could be designed this way.

5.5 Conclusion

We demonstrated capillary self-assembly of thin parallel ribbons on both the macroscopic and microscopic scale. Micro-ribbons made of silicon nitride are released wafer-scale from a silicon substrate by anisotropic wet etching. Under the action of surface tension, the two beams - which are anchored on both sides - twist, stretch and bend to finally form a highly symmetric and controllable three dimensional structure. The central parts of the beams rotate by 90° and stick along their smooth bottom sides.

The opening length - non sticking part - increases with the thickness of the beams. Since the beams are clamped on both sides, the deformation in-

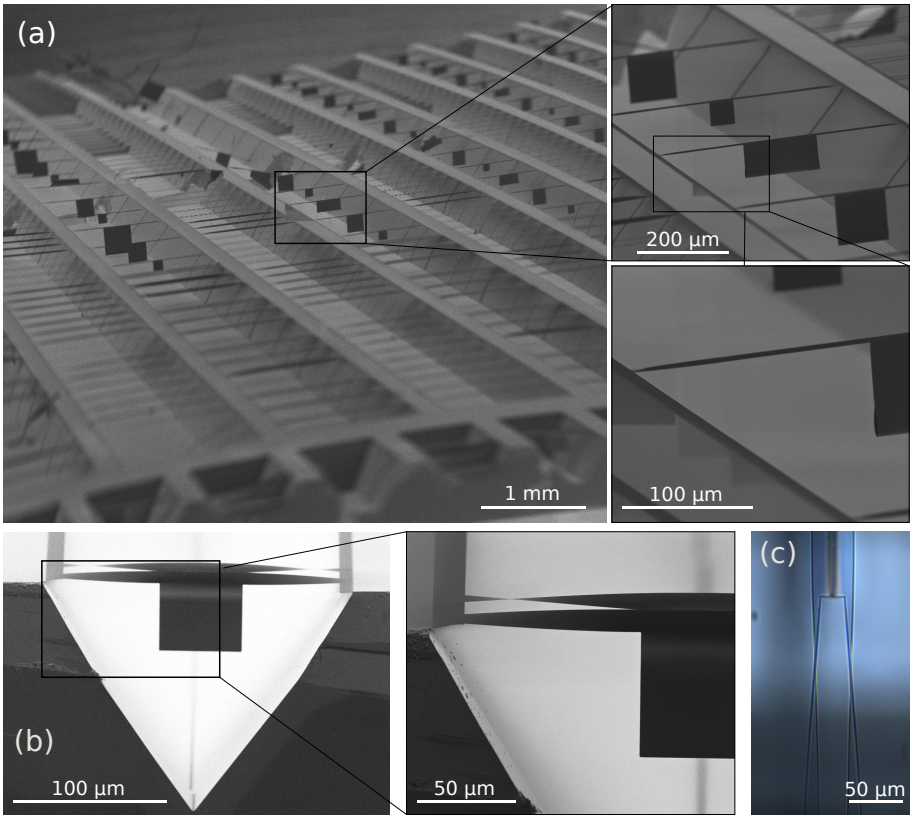

Figure 5.13 – Ribbons assembly with flaps on their sides. (a): Overview of a large amount of structures with close up of ribbons with integrated flaps. In this case the beams stick, as well as most of the flaps. Only the bottom parts of the flaps are opened. (b): Side view of a shorter similar structure. The wires are only L=200 µm and would not assemble without the flaps. (c): Optical microscope top view of the same structure. Only the edges of the flaps are in contact. Displacement of the beams is closed to null, while the twist is high.

duces a stress thats adds to the residual stress caused by the deposition process. Consequently, the opening length increases more than linearly with the separation between the beams, as well as with their width, and decreases with their length.

The quality of the water in which the micro-assembly takes place has little impact on the final opening length. The opening length of assembled pairs of ribbons is nearly identical using either millipore water that was changed every 24 h (conductivity $S = 1.5\,\mu S\,m^{-1}$) or rinsing DI water ($S = 157\,\mu S\,m^{-1}$). Stiffer sets of beams are found however to remain assembled after drying when using

dirtier water.

We checked these observations with a control experiment on the macro-scale, using several centimeters long polyester films wetted by silicone oil. In this configuration, the tension can be experimentally changed at their ends and is not increased by deformation. Our results show that the opening length now linearly increases with the tension, is independent of the length of the ribbons and linearly increases with their width.

A theoretical model for the opening length as a function of the width, separation, thickness and tension of the ribbons was developed by energy optimization. For macro assemblies the predicted opening length is in agreement with experimental values as long as the bending stiffness is small compare to the applied tension. In the micro-meter world, the model predicts the correct opening within 30 % when considering a surface energy between the two beams that equals the surface energy of pure water.

More complex structures yield more complex results. The assembly seems to be random when more than two ribbons are placed next to each others. Moreover overlapping of the wires instead of twisting is observed. When designed in a circular fashion, ribbons also randomly assemble while the opening is constant. Short wires that would normally not assemble can be twisted by designing flaps on their sides. It is possible to avoid lateral displacement of the wires, with the two flaps only adhering at their edges.

Our initial experiments demonstrate that elastocapillary twisting of micro-ribbons can be used to generate three-dimensional structures which cannot be fabricated by standard lithography techniques. We have only scratched the surface of the enormous design space, and expect that applications will be developed using twisting beams. Channels with out of plane outlets could be batch assembled this way for instance.

6

Conclusion and outlook

The work presented here is a humble contribution to the realm of self-folding. As introduced in **chapter 1** self-folding is a rather trending topic in which scientists draw inspirations on nature to develop new three-dimensional assembly strategies. Flowers, leaves, proteins and many more have the ability to fold or unfold triggered by diverse external stimuli. While examples of such three-dimensional fabrications abound in nature, we are bad at replicating them in our laboratories. Conventional micro and nano scale fabrication techniques are inherently two-dimensional and are inadequate to produce true three-dimensional sub-millimeter structures. Self-folding extends the precision of lithography techniques into the third dimension by combining well known top-down fabrication methods with the use of "weak" (compared to gravity at our scale) forces. We covered in the introduction most of the works on self-folding, from stress-based assembly to polymer thermal shrinking. Surface tension is a dominant force at the micro-scale and in consequence is one of the most used method for self-folding. In this thesis, we investigated the self-folding of micro-machined structures, whose final states depend on a balance between elastic and surface forces - the so-called elastocapillary folding - with an underlying interrogation in mind: can elastocapillary self-folding become a viable option for the fabrication of three-dimensional micro-machined objects?

Silicon nitride is a sturdy material and is hydrophilic, an ideal candidate for elastocapillary folding. Foldable origami-like patterns made of rigid plates connected to each others by flexible thin hinges can be fairly easily fabricated in silicon nitride. In **chapter 2** we demonstrated the controllable and repeatable actuation of silicon nitride micro-objects by means of through-wafer liquid application. As long as they remain wetted, structures can endure folding and reopening multiple times, up to 60 in a row in our experiments, without any signs of wear. The final folding angle is constant throughout the actuations, and can be accurately predicted by an energy minimization based model in the case of long two-dimensional extruded objects. Problems

arise when structures are allowed to dry in between folding. Residue from the fabrication process, hard to get rid off, aggregate on the hinges and stiffen the structures. Using resonance frequency measurements, the bending stiffness was found to increase by 50 % after the first drying. Folding becomes impossible after less than ten actuations and subsequent drying. This residue is obviously a problem since we do not know how to properly clean the structures once they are released from the substrate. Oxygen plasma was used to remove photoresist at the end of our fabrication process, but was unable to remove all the residue. Applications of such hydro-mechanical actuated micro-structures are therefore limited to situations in which objects remain wetted.

Through-wafer filling was initiated with the hope to batch fold objects. A sufficient high pressure needs to be applied to overcome pinning of the water meniscus at the edge of the tube and to wet the structure. This overpressure extends the fluidic setup and results in an overshoot of liquid. We could limit the excess liquid to a low (1.4 ± 0.4) nL by selecting rigid components for our fluidic setup (typical structures used for experiments contains around 200 nL). We however did not realize parallel folding of several structures at the time. By improving the way in which water is supplied, this should in principle be possible. Increasing the pressure by height difference instead of using a syringe should allow to apply a sufficiently high and lasting pressure to burst several tubes at a time. Alternatively, condensation or spraying of water are promising options to batch fold micro-structures and would be worth investigating.

In **chapter 3** we successfully demonstrated the assembly of similar structures as in chapter 2, but now with integrated bi-layer silicon nitride/Platinum conductive hinges. Objects were folded by manually depositing water on top of them. Many configurations were tried out to determine the best design of such metalized hinges. Only the length of the hinges have an impact on the fabrication yield, while the shape as well as the height of the transition between the hinges and the flaps show no influence. Short bi-layer hinges (length below 75 µm) were fabricated with a high yield of (72 ± 2) % and conductive hinges should be designed this way. The yield drops to (18 ± 2) % for long hinges (length above 100 µm). Stress mismatch between the layers provoke deformations of long hinges and resulted in interesting phenomena, such as buckling and bending of the thin plates. Only in rare cases these deformations cause breaking. The majority of the failures are attributed to burning of the top plat-

inum layer of the bi-layer hinges during the final oxygen plasma cleaning step. None of our folding experiments resulted in breaking of the conductive hinges, even in extreme cases when 10 µm long hinges (the shortest that could be designed) were bent to 180°. Resistivity of the metalized hinges is not affected by folding, and a current density as high as $j = (1.6 \pm 0.4) \times 10^6$ A/cm^2 was flown through them. This value is closed to reported values in literature at which electromigration was observed. Using this successful demonstration of conductive hinges, coupled with the hydro-mechanical actuation demonstrated in chapter 2, smart devices such as sensor/actuator array with electrical capabilities could be formed. Furthermore, our silicon nitride micro-objects are fully compatible with virtually any silicon based micro-fabrication techniques. Now that we have demonstrated that electrical wiring can be brought up to the folding elements, new applications can be envisioned such as sensors folded out of the wafer plane.

So far, the final assembled state of our structures has been determined by two flaps meeting during folding and adhering. Our final shapes are therefore limited by designs, and certain folding angles are simply impossible to obtain. In **chapter 4** we therefore introduced stop-programmable hinges. Starting from a simple micrometer-sized mask, accurate stop-programmable hinges were micro-machined in the three dimensions using nano-fabrication based on corner lithography. This fabrication method allows the accurate etching of material starting from any concave corners independently of their spatial orientation. It allows fabrication of well-defined rounded hinges with a flexible and a bonding part. We demonstrated the machining of such smart hinges that stop folding at $(70.6 \pm 0.1)°$ which in turn were used to fold three-dimensional micrometer sized tetrahedral structures. The feasibility of 90° stop-programmable hinges was also demonstrated. Since upright features are more difficult to realize, the fabrication was only partially successful, resulting in unbalanced hinges. This issue can however be easily solved in a new fabrication run. As long as the necessary molds can be obtained in silicon, the fabrication schemes described in chapter 4 are applicable to virtually any folding angle. Again, the fabrication of these smart hinges could be coupled with backside filling and electrical connection, hence increasing the complexity of potential applications. Moreover, the fabrication is wafer scale and allows the folding out of plane of several millimeter long plates with an extreme accuracy, which is knowingly hard to achieve with standard fabrication techniques.

The assembly in plane of thin parallel micro-ribbons that are released

wafer-scale from a silicon substrate by anisotropic wet etching was demonstrated in **chapter 5**. Under the action of water surface tension, the two beams - which are anchored on both sides - twist, stretch and bend to finally form a highly symmetric three dimensional structure. The central parts of the beams rotate by 90° and stick along their smooth bottom sides. The opening length - non sticking part - is found to be constant over the whole substrate. Stress induced by deformation adds to the residual stress in the beams. Consequently, the opening length increases more than linearly with the separation between the beams, as well as with their width, and decreases with their length. Control experiments were carried out on the macro-scale with polyester films wetted by silicone oil. Contrary to micro-ribbons, the tension in macro-ribbons can be tuned and there is no stress induced by deformation. Our results show that the opening length now linearly increases with the tension, is independent of the length of the ribbons and linearly increases with their width. An energy minimization model was developed which constantly predicts correct openings in the macro-world but does not represent the trends well for micro-experiments, probably because of over-estimated induced stress. We nevertheless demonstrated a fast, wafer scale and highly controllable fabrication and assembly of micro-ribbons. Freedom of design is less with twisting structures when compare to the folding of flaps, but the technique is batch and more controllable. Application wise, micro channels could for instance be fabricated on top of the ribbons and batch-assembled, resulting in a three-dimensional network of channels with possible mixing of liquid between them or out of plane outlets.

To summarize, the work presented in this thesis brings tools for successful applications of elastocapillary folded micro-machined structures. We demonstrated the out of plane folding of silicon nitride plates and proved that controllable actuation is possible. Moreover, electrical capabilities were successfully implemented in flaps and stop-programmable hinges can be fabricated. All these features combined should pave the way to complex applications. More research however is necessary, such as reliable batch folding and investigation on the residue present on structures at the end of the fabrication process. On the theoretical side, we developed a two-dimensional model that proved to be accurate in predicting folding angles of long two-dimensional like structures. Extending this approach to more complex three-dimensional structures would require to be able to determine the shape of complex liquid meniscus. Numerical tools are however available for this purpose and could be used to extend our theoretical knowledge.

Appendix

A

Stop-programmable hinges: process flow

In this appendix the complete process flows are given for stop-programmable hinges presented in **chapter 4**.

A.1 Process parameters - 70.6° stop-programmable hinges

A.1.1 Substrate selection

Step	Process	
1	**Substrate Silicon <110> P-type** *(#subs110)*	NL-CLR-Wafer Storage Cupboard Parameters: ★ Orientation: <110> ★ Diameter: 100 mm ★ Thickness: (380 ± 10) µm ★ Polished: Double side polished ★ Resistivity: 5 Ω cm to 10 Ω cm ★ Type: P

A.1.2 Making the molds

Step	Process	
2	**Standard cleaning HNO_3** *(#clean1001)*	NL-CR-WB14 HNO_3 (99 %) Selectiepur: MERCK HNO_3 (69 %) VLSI: MERCK • Beaker 1: fumic HNO_3 (99 %), 5 min • Beaker 2: fumic HNO_3 (99 %), 5 min • Quick Dump Rinse: < 0.1 µS

		• Beaker 3: boiling (95 °C) HNO_3 (69 %), 10 min • Quick Dump Rinse: < 0.1 µS • Spin drying
3	**LPCVD of SiRN (200-300 Mpa)** *(#film155)*	NL-CLR-Tempress LPCVD G4 Parameters: ★ Temp.: 850 °C ★ SiH_2Cl_2 flow: 150 sccm ★ NH_3 flow: 50 sccm ★ Pressure: 200 mTorr ★ Refractive index n=2.18 **Thickness:** ∼25 nm **Deposition time:** 4 min
		Hard mask for KOH etching.
4	**Ellipsometer measurement** *(#metro017)*	NL-CLR-Woolam M-2000 ellipsometer
5	**Standard lithography Olin 907-17** *(#lith1002)*	
	Dehydration bake	Spincoater • Hotplate: (120 °C): 5 min
	Priming (HMDS)	NL-CR / WB 21-22 • Spin program: 4 (4000 rpm, 30 s)
	Coating (OLIN 907-17)	Primus Spinner • Spin program: 4 (4000 rpm, 30 s, 1.7 µm) • Prebake (95 °C): 90 s

	Alignment & Exposure (Olin 907-17)	Electronic Vision Group 620 Mask Aligner • Hg-lamp: 12 mW/cm^2 • Exposure time: 4 s • Mask: **COR**
	Development (Olin 907-17)	Developer: OPD4262 • After exposure bake (120 ∘ C): 60 s • Time: 30 s in beaker 1 • Time: 15-30 s in beaker 2 • Quick Dump Rinse: < 0.1 µS • Spin drying
	Postbake (Olin 907-17)	NL-CLR-WB21 • Hotplate: (120 °C): 20 min
	Inspection by optical microscope	NL-CR / Nikon Microscope Dedicated microscope for lithography inspection
6	**RIE CHF_3/O_2 (Tetske)** *(#etch193)*	NL-CLR-Tetske Parameters: ★ Chamber: dirty ★ Electrode: Styros ★ Pressure: 10 mTorr ★ CHF_3 flow: 25 sccm ★ O_2 flow: 5 sccm ★ Power: 60 W ★ Etch rate: 35 nm/min **Etching time:** 1 min
7	**Stripping of Olin resist in HNO_3 (99%)** *(#lith116)*	NL-CLR-WB14 • Beaker 0: HNO_3 (99%)

		time: > 10 min or 100% removal of PR • Quick Dump Rinse: < 0.1 µS
8	**Etching in KOH standard** *(#etch138)*	NL-CR-WB17 • Use dedicated beaker 1 or 2 **Etching time:** 20 min • Rinsing in beaker 5 min in beaker 1 and beaker 2. Refresh and repeat several times. • Quick Dump Rinse **WB18**: < 0.1 µS
9	**Cleaning RCA 2 megasonic** *(#clean116)*	NL-CR-WB18 • Cleaning time: 15 min Mixture: HCL:H_2O_2 :H_2O (1:1:20) vol%. Start fill; bath is filled with H_2O and HCL, and heated. When temp. is 55 °C add the H_2O_2 by pressing [Continue]. • Quick Dump Rinse: < 0.1 µS
10	**Etching in HF 50%** *(#etch129)*	NL-CLR-WB15 Use dedicated beaker. • Etching process wafers: 10 s. • Quick Dump Rinse: < 0.1 µS
		Stripping of the hard mask.
11	**Standard cleaning HNO_3** *(#clean1001)*	NL-CR-WB14 HNO_3 (99 %) Selectiepur: MERCK HNO_3 (69 %) VLSI: MERCK

		• Beaker 1: fumic HNO_3 (99 %), 5 min • Beaker 2: fumic HNO_3 (99 %), 5 min • Quick Dump Rinse: < 0.1 µS • Beaker 3: boiling (95 °C) HNO_3 (69 %), 10 min • Quick Dump Rinse: < 0.1 µS • Spin drying
12	**Wet oxidation of silicon** @1150 °C *(#film114)*	NL-CLR- Furnace B2 Program WET1150 - parameters: ★ Temp.: 1150 °C ★ Gas: H_2O + N_2 (Bubbler) ★ N_2 flow: 2 liter/min ★ Ramp: 10 °C min^{-1} ★ Cooldown: 7.5 °C min^{-1} ★ Refractive index n=1.47 **Oxidation time:** 120 min. **Radius of curvature:** $R \simeq 1$ µm.
13	**Etching in HF 50%** *(#etch129)*	NL-CLR-WB15 Use dedicated beaker. • Etching process wafers: 2 min. • Quick Dump Rinse: < 0.1 µS

A.1.3 Corner lithography

Step	Process	
14	**Pre-furnace cleaning** *(#clean1202)*	NL-CR-WB 14 and 15 • Beaker 1: fumic HNO_3 (99 %), 5 min

		• Beaker 2: fumic HNO_3 (99 %), 5 min • Quick Dump Rinse: < 0.1 µS • Beaker 3: boiling (95 °C) HNO_3 (69 %), 10 min • Quick Dump Rinse: < 0.1 µS • Etching in HF 1% (metal free): 1 min • Quick Dump Rinse: < 0.1 µS • Spin drying
15	**LPCVD of SiRN (200-300 Mpa)** *(#film155)*	NL-CLR-Tempress LPCVD G4 Parameters: ★ Temp.: 850 °C ★ SiH_2Cl_2 flow: 150 sccm ★ NH_3 flow: 50 sccm ★ Pressure: 200 mTorr ★ Refractive index n=2.18 **Thickness:** 1 µm **Deposition time:** 120 min **Dummy:** 1
16	**Optical inspection of LPCVD layers** *(#metro013)*	NL-CR / Cold Light Source
17	**Ellipsometer measurement** *(#metro017)*	NL-CLR-Woolam M-2000 ellipsometer
18	**Pre-furnace cleaning** *(#clean1202)*	NL-CR-WB 14 and 15 • Beaker 1: fumic HNO_3 (99 %), 5 min • Beaker 2: fumic HNO_3 (99 %), 5 min • Quick Dump Rinse: < 0.1 µS • Beaker 3: boiling (95 °C) HNO_3 (69 %), 10 min • Quick Dump Rinse: < 0.1 µS • Etching in HF 1% (metal free): 1 min

		• Quick Dump Rinse: < 0.1 µS • Spin drying Optional step: wafers can directly go from one tube to the next.
19	**Micro Balance Measurement** *(#metro106)*	NL-CLR-Sartortius Micro Balance Use dummy wafer.
20	**LPCVD of Poly Silicon** *(#film105)*	NL-CLR-LPCVD F2 Program senspoly - parameters: ★ Temp.: 590 °C ★ SiH_4 flow: 50 sccm ★ Pressure: 250 mTorr ★ Deposition rate: ± 3.4 nm/min ★ Stress 30 MPa **Thickness:** ~150 nm **Deposition time:** 45 min **Dummy:** 1
21	**Micro Balance Measurement** *(#metro106)*	NL-CLR-Sartortius Micro Balance Use dummy wafer.
22	**Pre-furnace cleaning** *(#clean1202)*	NL-CR-WB 14 and 15 • Beaker 1: fumic HNO_3 (99 %), 5 min • Beaker 2: fumic HNO_3 (99 %), 5 min • Quick Dump Rinse: < 0.1 µS • Beaker 3: boiling (95 °C) HNO_3 (69 %), 10 min • Quick Dump Rinse: < 0.1 µS • Etching in HF 1% (metal free): 1 min • Quick Dump Rinse: < 0.1 µS • Spin drying Optional step: wafers can directly go from one tube to the next.

23	**LPCVD of SiRN (200-300 Mpa)** *(#film155)*	NL-CLR-Tempress LPCVD G4 Parameters: ★ Temp.: 850 °C ★ SiH_2Cl_2 flow: 150 sccm ★ NH_3 flow: 50 sccm ★ Pressure: 200 mTorr ★ Refractive index n=2.18 **Thickness:** ~150 nm **Deposition time:** 17 min **Dummies:** 1 between every 2 process wafers
24	**Optical inspection of LPCVD layers** *(#metro013)*	NL-CR / Cold Light Source
25	**Ellipsometer measurement** *(#metro017)*	NL-CLR-Woolam M-2000 ellipsometer
	Accurate measurements of all dummies at a pre-defined point.	
26	**Etching in HF 1% (metal free)** *(#etch127)*	NL-CLR-WB15 • Etching time: 1 min • Quick Dump Rinse: < 0.1 µS
	To remove native oxide on top of SiRN. Transport wafers in DI water.	
27	**Etching in H_3PO_4 Standard** @180 °C *(#etch153)*	NL-CLR-WB08 Use dedicated beaker with reflux lid for etching. • Use dummy to determine etch rate (about 4 nm min^{-1}). • Timed etching of top SiRN.

		The total etching time might differ from one wafer to another. The Poly Silicon layer is reached when the wafers become hydrophobic. Up to 0.1 over-etch. • Quick Dump Rinse: < 0.1 µS Transport wafers in DI water.
28	**Standard cleaning HNO_3** *(#clean1001)*	NL-CR-WB14 HNO_3 (99 %) Selectiepur: MERCK HNO_3 (69 %) VLSI: MERCK • Beaker 1: fumic HNO_3 (99 %), 5 min • Beaker 2: fumic HNO_3 (99 %), 5 min • Quick Dump Rinse: < 0.1 µS • Beaker 3: boiling (95 °C) HNO_3 (69 %), 10 min • Quick Dump Rinse: < 0.1 µS • Spin drying
29	**Wet oxidation of silicon** @900 °C *(#film115)*	NL-CLR- Furnace B2 Program WET900 - parameters: ★ Temp.: 900 °C ★ Gas: H_2O + N_2 (Bubbler) ★ N_2 flow: 2 liter/min ★ Ramp: 10 °C min^{-1} ★ Cooldown: 7.5 °C min^{-1} ★ Refractive index n=1.47 **Thickness:** <100> planes: ~50 nm, <111>: ~70 nm **Oxidation time:** 10 min **Dummies:** 1 for each orientations
30	**Ellipsometer measurement** *(#metro017)*	NL-CLR-Woolam M-2000 ellipsometer

31	**Etching in HF 1%** **(metal free)** *(#etch127)*	NL-CLR-WB15 • Etching time: 1 min • Quick Dump Rinse: < 0.1 µS
	To remove native oxide on top of SiRN wires. Transport wafers in DI water.	
32	**Etching in H_3PO_4** **Standard** @180 °C *(#etch153)*	NL-CLR-WB08 Use dedicated beaker with reflux lid for etching. • Removal of SiRN wires in corners: 15 min. • Quick Dump Rinse: < 0.1 µS
	Transport wafers in DI water.	
33	**Etching in TMAH 5 wt%** **Standard** @70 °C *(#etch148)*	NL-CLR-WB10 Use standard solution. • Use dummy to determine etch rate. • Etching process wafers.
	Tune etching time accordingly to desired retraction.	
		• Quick Dump Rinse: < 0.1 µS • Spin drying
34	**Standard cleaning HNO_3** *(#clean1001)*	NL-CR-WB14 HNO_3 (99 %) Selectiepur: MERCK HNO_3 (69 %) VLSI: MERCK • Beaker 1: fumic HNO_3 (99 %), 5 min • Beaker 2: fumic HNO_3 (99 %), 5 min • Quick Dump Rinse: < 0.1 µS • Beaker 3: boiling (95 °C) HNO_3 (69 %), 10 min • Quick Dump Rinse: < 0.1 µS

		• Spin drying
35	**Etching in HF 50%** *(#etch129)*	NL-CLR-WB15 Use dedicated beaker. • Use dummy to determine etch rate (~ 3.2 nm min^{-1}). • Etching process wafers. Tune etching time accordingly to thickness of bottom SiRN layer. Over-etching necessary to remove extra material in corners. • Quick Dump Rinse: < 0.1 µS
36	**Standard cleaning HNO_3** *(#clean1001)*	NL-CR-WB14 HNO_3 (99 %) Selectiepur: MERCK HNO_3 (69 %) VLSI: MERCK • Beaker 1: fumic HNO_3 (99 %), 5 min • Beaker 2: fumic HNO_3 (99 %), 5 min • Quick Dump Rinse: < 0.1 µS • Beaker 3: boiling (95 °C) HNO_3 (69 %), 10 min • Quick Dump Rinse: < 0.1 µS • Spin drying
37	**Wet oxidation of silicon** @900 °C *(#film115)*	NL-CLR- Furnace B2 Program WET900 - parameters: ★ Temp.: 900 °C ★ Gas: H_2O + N_2 (Bubbler) ★ N_2 flow: 2 liter/min ★ Ramp: 10 °C min^{-1} ★ Cooldown: 7.5 °C min^{-1} ★ Refractive index n=1.47 **Oxidation time:** long enough to consume all the Poly Silicon

38	**Etching in HF 50%** *(#etch129)*	NL-CLR-WB15 Use dedicated beaker. • Etching process wafers: 10 s. • Quick Dump Rinse: < 0.1 µS

A.1.4 Flat hinges

Step	Process	
39	**Lithography AZ 9260** *(#lith193)*	
	Priming HMDS	NL-CR-WB28 Lab-line Duo-vac-oven • Dehydration bake (150 °C, low pressure): 5 min • Vapor prime HMDS at (150 °C: 5 min • Let the wafers cool down to room temperature
	Coating (AZ 9260)	Primus Spinner • Spin program: 18 (10 s @ 300 rpm, 60 s @ 2400 rpm) • Prebake (110 °C): 165 s
	Alignment & Exposure (AZ 9260)	Electronic Vision Group 620 Mask Aligner • Hg-lamp: 12 mW/cm^2 • Exposure time: 3 times 10 s with 10 s delay • Mask: **FOLD**
	Development (AZ 9260)	Developer: OPD4262 • Time: 3 min 30 s in beaker 1 • Time: 3 min 30 s in beaker 2

		• Quick Dump Rinse: < 0.1 µS • Spin drying
	Inspection by optical microscope	NL-CR / Nikon Microscope Dedicated microscope for lithography inspection
40	**RIE CHF_3/O_2 (Tetske)** *(#etch193)*	NL-CLR-Tetske Parameters: ★ Chamber: dirty ★ Electrode: Styros ★ Pressure: 10 mTorr ★ CHF_3 flow: 25 sccm ★ O_2 flow: 5 sccm ★ Power: 60 W ★ Etch rate: 35 nm/min **Etching time:** 30 min
41	**Stripping of Olin resist in HNO_3 (99%)** *(#lith116)*	NL-CLR-WB14 • Beaker 0: HNO_3 (99%) time: > 10 min or 100% removal of PR • Quick Dump Rinse: < 0.1 µS
42	**Pre-furnace cleaning** *(#clean1202)*	NL-CR-WB 14 and 15 • Beaker 1: fumic HNO_3 (99 %), 5 min • Beaker 2: fumic HNO_3 (99 %), 5 min • Quick Dump Rinse: < 0.1 µS • Beaker 3: boiling (95 °C) HNO_3 (69 %), 10 min • Quick Dump Rinse: < 0.1 µS • Etching in HF 1% (metal free): 1 min • Quick Dump Rinse: < 0.1 µS • Spin drying

43	**LPCVD of SiRN (200-300 Mpa)** *(#film155)*	NL-CLR-Tempress LPCVD G4 Parameters: ★ Temp.: 850 °C ★ SiH_2Cl_2 flow: 150 sccm ★ NH_3 flow: 50 sccm ★ Pressure: 200 mTorr ★ Refractive index n=2.18 **Thickness:** 120 nm **Deposition time:** 12 min **Dummies:** 1 every two process wafers
44	**Optical inspection of LPCVD layers** *(#metro013)*	NL-CR / Cold Light Source
45	**Ellipsometer measurement** *(#metro017)*	NL-CLR-Woolam M-2000 ellipsometer

A.1.5 Patterning the foldable structures

Step	Process	
46	**Pre-furnace cleaning** *(#clean1202)*	NL-CR-WB 14 and 15 • Beaker 1: fumic HNO_3 (99 %), 5 min • Beaker 2: fumic HNO_3 (99 %), 5 min • Quick Dump Rinse: < 0.1 µS • Beaker 3: boiling (95 °C) HNO_3 (69 %), 10 min • Quick Dump Rinse: < 0.1 µS • Etching in HF 1% (metal free): 1 min • Quick Dump Rinse: < 0.1 µS • Spin drying

47	**Lithography AZ 9260** *(#lith193)*	
	Priming HMDS	NL-CR-WB28 Lab-line Duo-vac-oven • Dehydration bake (150 °C, low pressure): 5 min • Vapor prime HMDS at (150 °C: 5 min • Let the wafers cool down to room temperature
	Coating (AZ 9260)	Primus Spinner • Spin program: 18 (10 s @ 300 rpm, 60 s @ 2400 rpm) • Prebake (110 °C): 165 s
	Alignment & Exposure (AZ 9260)	Electronic Vision Group 620 Mask Aligner • Hg-lamp: 12 mW/cm^2 • Exposure time: 3 times 10 s with 10 s delay • Mask: **GEOM**
	Development (AZ 9260)	Developer: OPD4262 • Time: 3 min 30 s in beaker 1 • Time: 3 min 30 s in beaker 2 • Quick Dump Rinse: < 0.1 µS • Spin drying
	Inspection by optical microscope	NL-CR / Nikon Microscope Dedicated microscope for lithography inspection
48	**RIE CHF_3/O_2 (Tetske)** *(#etch193)*	NL-CLR-Tetske Parameters: ★ Chamber: dirty ★ Electrode: Styros ★ Pressure: 10 mTorr

- ★ CHF_3 flow: 25 sccm
- ★ O_2 flow: 5 sccm
- ★ Power: 60 W
- ★ Etch rate: 35 nm/min

Etching time: 35 min

A.1.6 Release of the structures

Step	Process	
49	**RIE of silicon semi-isotropic** *(Custom recipe)*	NL-CLR-Adixen AMS 100 SE • Native oxide removal Recipe *"Roberts", (#etch174)* **Etching time:** 10 s • Ignition step Parameters: ★ Temp.: 20 °C ★ SF_6 flow: 200 sscm ★ RF power: 2000 W ★ LF power: 0 W ★ APC position: 80 % **Etching time:** 10 s • Silicon etching Parameters: ★ Temp.: 20 °C ★ SF_6 flow: 200 sscm ★ RF power: 2000 W ★ LF power: 0 W ★ APC position: 15 % ★ Substrate height: 200 mm

		Etching time: ~200 min
50	**Stripping of resist in O_2 plasma** *(#lith117)*	NL-CLR- Tepla 300E Parameters: ★ Barrel Etcher (2.45 GHz) ★ Pressure: 1.2 mbar ★ O_2 flow: 200 sccm ★ Power: 500 W **Stripping time:** 2 times 60 min

A.2 Process parameters - 90° stop-programmable hinges

A.2.1 Substrate selection

Step	Process	
1	**Substrate Silicon <100> OSP N-type** *(#subs109)*	NL-CLR-Wafer Storage Cupboard Parameters: ★ Orientation: <100> ★ Diameter: 100 mm ★ Thickness: (381 ± 15) µm ★ Polished: Single side polished ★ Resistivity: 1 Ω cm to 10 Ω cm ★ Type: N

A.2.2 Making the molds

Step	Process	
2	**Standard cleaning HNO_3** *(#clean1001)*	NL-CR-WB14 HNO_3 (99 %) Selectiepur: MERCK HNO_3 (69 %) VLSI: MERCK • Beaker 1: fumic HNO_3 (99 %), 5 min • Beaker 2: fumic HNO_3 (99 %), 5 min • Quick Dump Rinse: < 0.1 µS • Beaker 3: boiling (95 °C) HNO_3 (69 %), 10 min • Quick Dump Rinse: < 0.1 µS • Spin drying
3	**Standard lithography Olin 907-17** *(#lith1002)*	
	Dehydration bake	Spincoater • Hotplate: (120 °C): 5 min
	Priming (HMDS)	NL-CR / WB 21-22 • Spin program: 4 (4000 rpm, 30 s)
	Coating (OLIN 907-17)	Primus Spinner • Spin program: 4 (4000 rpm, 30 s, 1.7 µm) • Prebake (95 °C): 90 s
	Alignment & Exposure (Olin 907-17)	Electronic Vision Group 620 Mask Aligner • Hg-lamp: 12 mW/cm^2 • Exposure time: 4 s • Mask: **COR**
	Development (Olin 907-17)	Developer: OPD4262 • After exposure bake (120 ∘ C): 60 s

		• Time: 30 s in beaker 1 • Time: 15-30 s in beaker 2 • Quick Dump Rinse: < 0.1 µS • Spin drying
	Postbake **(Olin 907-17)**	NL-CLR-WB21 • Hotplate: (120 °C): 20 min
	Inspection by **optical microscope**	NL-CR / Nikon Microscope Dedicated microscope for lithography inspection
4	**Etching BHF (1:7)** **SiO_2** *(#etch124)*	NL-CR-WB15 • Use standard solution: 1 min. • Quick Dump Rinse: < 0.1 µS
	Native oxide etching. Directly go to the next step.	
5	**DRIE $SF_6/0_2$ cryogenic** *(Custom recipe)*	NL-CLR-Adixen AMS 100 SE Parameters: ★ Temp.: −110 °C ★ SF_6 flow: 200 sscm ★ O_2 flow: 15 sscm ★ Pressure: 1.6×10^{-2} mbar ★ RF power: 1000 W ★ LF power: 20 W ★ On/Off time: 25/75 ms **Etching time:** 2 min **Etching depth:** ∼ 10 µm
	Run the recipe first with a dummy and check cross-section.	
6	**Stripping of Olin resist** **in HNO_3 (99%)**	NL-CLR-WB14

	(#lith116)	• Beaker 0: HNO_3 (99%) time: > 10 min or 100% removal of PR • Quick Dump Rinse: < 0.1 µS
7	**Standard cleaning HNO_3** *(#clean1001)*	NL-CR-WB14 HNO_3 (99 %) Selectiepur: MERCK HNO_3 (69 %) VLSI: MERCK • Beaker 1: fumic HNO_3 (99 %), 5 min • Beaker 2: fumic HNO_3 (99 %), 5 min • Quick Dump Rinse: < 0.1 µS • Beaker 3: boiling (95 °C) HNO_3 (69 %), 10 min • Quick Dump Rinse: < 0.1 µS • Spin drying
	Only if next step is necessary.	
8	**Wet oxidation of silicon @**1150 °C *(#film114)*	NL-CLR- Furnace B2 Program WET1150 - parameters: ★ Temp.: 1150 °C ★ Gas: H_2O + N_2 (Bubbler) ★ N_2 flow: 2 liter/min ★ Ramp: 10 °C min^{-1} ★ Cooldown: 7.5 °C min^{-1} ★ Refractive index n=1.47 **Oxidation time:** Depends on desired *R*.
Only if the mold is not round enough to respect the design criterion, equation 4.2.2.		

A.2.3 Corner lithography

Step	Process	
9	**Pre-furnace cleaning** *(#clean1202)*	NL-CR-WB 14 and 15 • Beaker 1: fumic HNO_3 (99 %), 5 min • Beaker 2: fumic HNO_3 (99 %), 5 min • Quick Dump Rinse: < 0.1 µS • Beaker 3: boiling (95 °C) HNO_3 (69 %), 10 min • Quick Dump Rinse: < 0.1 µS • Etching in HF 1% (metal free): 1 min • Quick Dump Rinse: < 0.1 µS • Spin drying
10	**LPCVD of SiRN (200-300 Mpa)** *(#film155)*	NL-CLR-Tempress LPCVD G4 Parameters: ★ Temp.: 850 °C ★ SiH_2Cl_2 flow: 150 sccm ★ NH_3 flow: 50 sccm ★ Pressure: 200 mTorr ★ Refractive index n=2.18 **Thickness:** 1 µm **Deposition time:** 120 min **Dummy:** 1
11	**Optical inspection of LPCVD layers** *(#metro013)*	NL-CR / Cold Light Source
12	**Ellipsometer measurement** *(#metro017)*	NL-CLR-Woolam M-2000 ellipsometer
13	**Pre-furnace cleaning** *(#clean1202)*	NL-CR-WB 14 and 15 • Beaker 1: fumic HNO_3 (99 %), 5 min • Beaker 2: fumic HNO_3 (99 %), 5 min

		• Quick Dump Rinse: < 0.1 µS • Beaker 3: boiling (95 °C) HNO_3 (69 %), 10 min • Quick Dump Rinse: < 0.1 µS • Etching in HF 1% (metal free): 1 min • Quick Dump Rinse: < 0.1 µS • Spin drying

Optional step: wafers can directly go from one tube to the next.

14	**Micro Balance Measurement** *(#metro106)*	NL-CLR-Sartortius Micro Balance Use dummy wafer
15	**LPCVD of Poly Silicon** *(#film105)*	NL-CLR-LPCVD F2 Program senspoly - parameters: ★ Temp.: 590 °C ★ SiH_4 flow: 50 sccm ★ Pressure: 250 mTorr ★ Deposition rate: ± 3.4 nm/min ★ Stress 30 MPa **Thickness:** ∼150 nm **Deposition time:** 45 min **Dummy:** 1
16	**Micro Balance Measurement** *(#metro106)*	NL-CLR-Sartortius Micro Balance Use dummy wafer
17	**Pre-furnace cleaning** *(#clean1202)*	NL-CR-WB 14 and 15 • Beaker 1: fumic HNO_3 (99 %), 5 min • Beaker 2: fumic HNO_3 (99 %), 5 min • Quick Dump Rinse: < 0.1 µS • Beaker 3: boiling (95 °C) HNO_3 (69 %), 10 min • Quick Dump Rinse: < 0.1 µS • Etching in HF 1% (metal free): 1 min • Quick Dump Rinse: < 0.1 µS

		• Spin drying
		Optional step: wafers can directly go from one tube to the next.
18	**LPCVD of SiRN (200-300 Mpa)** *(#film155)*	NL-CLR-Tempress LPCVD G4 Parameters: ★ Temp.: 850 °C ★ SiH_2Cl_2 flow: 150 sccm ★ NH_3 flow: 50 sccm ★ Pressure: 200 mTorr ★ Refractive index n=2.18 **Thickness:** ~150 nm **Deposition time:** 17 min **Dummies:** 1 between every 2 process wafers
19	**Optical inspection of LPCVD layers** *(#metro013)*	NL-CR / Cold Light Source
20	**Ellipsometer measurement** *(#metro017)*	NL-CLR-Woolam M-2000 ellipsometer
		Accurate measurements of all dummies at a pre-defined point.
21	**Etching in HF 1% (metal free)** *(#etch127)*	NL-CLR-WB15 • Etching time: 1 min • Quick Dump Rinse: < 0.1 µS
		To remove native oxide on top of SiRN. Transport wafers in DI water.
22	**Etching in H_3PO_4 Standard** @180 °C	NL-CLR-WB08 Use dedicated beaker with reflux lid for etching.

	(#etch153)	• Use dummy to determine etch rate (about 4 nm min^{-1}). • Timed etching of top SiRN. The total etching time might differ from one wafer to another. The Poly Silicon layer is reached when the wafers become hydrophobic. Up to 0.4 over-etch. • Quick Dump Rinse: < 0.1 µS Transport wafers in DI water.
23	**Standard cleaning HNO_3** *(#clean1001)*	NL-CR-WB14 HNO_3 (99 %) Selectiepur: MERCK HNO_3 (69 %) VLSI: MERCK • Beaker 1: fumic HNO_3 (99 %), 5 min • Beaker 2: fumic HNO_3 (99 %), 5 min • Quick Dump Rinse: < 0.1 µS • Beaker 3: boiling (95 °C) HNO_3 (69 %), 10 min • Quick Dump Rinse: < 0.1 µS • Spin drying
24	**Wet oxidation of silicon @**900 °C *(#film115)*	NL-CLR- Furnace B2 Program WET900 - parameters: ★ Temp.: 900 °C ★ Gas: H_2O + N_2 (Bubbler) ★ N_2 flow: 2 liter/min ★ Ramp: 10 °C min^{-1} ★ Cooldown: 7.5 °C min^{-1} ★ Refractive index n=1.47 **Thickness:** <100> planes: ∼50 nm, <111>: ∼70 nm **Oxidation time:** 10 min **Dummies:** 1 for each orientations

25	**Ellipsometer measurement** *(#metro017)*	NL-CLR-Woolam M-2000 ellipsometer
26	**Etching in HF 1% (metal free)** *(#etch127)*	NL-CLR-WB15 • Etching time: 1 min • Quick Dump Rinse: < 0.1 µS
	To remove native oxide on top of SiRN wires. Transport wafers in DI water.	
27	**Etching in H_3PO_4 Standard** @180 °C *(#etch153)*	NL-CLR-WB08 Use dedicated beaker with reflux lid for etching. • Removal of SiRN wires in corners: 15 min. • Quick Dump Rinse: < 0.1 µS
	Transport wafers in DI water.	
28	**Etching in TMAH 5 wt% Standard** @70 °C *(#etch148)*	NL-CLR-WB10 Use standard solution. • Use dummy to determine etch rate. • Etching process wafers.
	Tune etching time accordingly to desired retraction.	
		• Quick Dump Rinse: < 0.1 µS • Spin drying

A.2.4 Patterning the molds

Step	Process	
29	**Standard cleaning HNO_3** *(#clean1001)*	NL-CR-WB14 HNO_3 (99 %) Selectiepur: MERCK HNO_3 (69 %) VLSI: MERCK • Beaker 1: fumic HNO_3 (99 %), 5 min • Beaker 2: fumic HNO_3 (99 %), 5 min • Quick Dump Rinse: < 0.1 µS • Beaker 3: boiling (95 °C) HNO_3 (69 %), 10 min • Quick Dump Rinse: < 0.1 µS • Spin drying
30	**Etching in 50%** *(#etch129)*	NL-CLR-WB15 Use dedicated beaker. • Etching process wafers: 10 s. • Quick Dump Rinse: < 0.1 µS Stripping of SiO_2 layer.
31	**Standard cleaning HNO_3** *(#clean1001)*	NL-CR-WB14 HNO_3 (99 %) Selectiepur: MERCK HNO_3 (69 %) VLSI: MERCK • Beaker 1: fumic HNO_3 (99 %), 5 min • Beaker 2: fumic HNO_3 (99 %), 5 min • Quick Dump Rinse: < 0.1 µS • Beaker 3: boiling (95 °C) HNO_3 (69 %), 10 min • Quick Dump Rinse: < 0.1 µS • Spin drying
32	**Wet oxidation of silicon @**800 °C *(#film142)*	NL-CLR- Furnace B2 Program WET900 - parameters: ★ Temp.: 900 °C ★ Gas: H_2O + N_2 (Bubbler) ★ N_2 flow: 2 liter/min

★ Ramp: 10 °C min^{-1}
★ Cooldown: 7.5 °C min^{-1}
★ Refractive index n=1.47

Thickness: ~5 nm
Oxidation time: ~5 min

No need to start a program, just load the wafers.

---

33 **Lithography AZ 9260**
(#lith193)

Priming HMDS	NL-CR-WB28 Lab-line Duo-vac-oven • Dehydration bake (150 °C, low pressure): 5 min • Vapor prime HMDS at (150 °C: 5 min • Let the wafers cool down to room temperature
Coating (AZ 9260)	Primus Spinner • Spin program: 18 (10 s @ 300 rpm, 60 s @ 2400 rpm) • Prebake (110 °C): 165 s
Alignment & Exposure (AZ 9260)	Electronic Vision Group 620 Mask Aligner • Hg-lamp: 12 mW/cm^2 • Exposure time: 3 times 10 s with 10 s delay • Mask: **GEOM**
Development (AZ 9260)	Developer: OPD4262 • Time: 3 min 30 s in beaker 1 • Time: 3 min 30 s in beaker 2 • Quick Dump Rinse: < 0.1 µS • Spin drying

	Inspection by optical microscope	NL-CR / Nikon Microscope Dedicated microscope for lithography inspection
34	**Etching BHF (1:7) SiO_2** *(#etch124)*	NL-CR-WB15 • Use standard solution: 30 s The wafers should turn hydrophobic where there is no photoresist. • Quick Dump Rinse: < 0.1 µS
35	**Stripping of Olin resist in HNO_3 (99%)** *(#lith116)*	NL-CLR-WB14 • Beaker 0: HNO_3 (99%) time: > 10 min or 100% removal of PR • Quick Dump Rinse: < 0.1 µS
36	**Etching in TMAH 5 wt% Standard @**70 °C *(#etch148)*	NL-CLR-WB10 Use standard solution. • Use dummy to determine etch rate. • Etching process wafers. Tune etching time accordingly to the thickness of Poly Silicon. The wafers should turn hydrophilic where there is no masking layer. • Quick Dump Rinse: < 0.1 µS
37	**Standard cleaning HNO_3** *(#clean1001)*	NL-CR-WB14 HNO_3 (99 %) Selectiepur: MERCK HNO_3 (69 %) VLSI: MERCK • Beaker 1: fumic HNO_3 (99 %), 5 min • Beaker 2: fumic HNO_3 (99 %), 5 min • Quick Dump Rinse: < 0.1 µS

		• Beaker 3: boiling (95 °C) HNO_3 (69 %), 10 min • Quick Dump Rinse: < 0.1 µS • Spin drying
38	**Etching in 50%** *(#etch129)*	NL-CLR-WB15 Use dedicated beaker. • Use dummy to determine etch rate (∼ 3.2 nm min^{-1}). • Etching process wafers. Tune etching time accordingly to thickness of bottom SiRN layer. Over-etching necessary to remove extra material in corners. • Quick Dump Rinse: < 0.1 µS
39	**Pre-furnace cleaning** *(#clean1202)*	NL-CR-WB 14 and 15 • Beaker 1: fumic HNO_3 (99 %), 5 min • Beaker 2: fumic HNO_3 (99 %), 5 min • Quick Dump Rinse: < 0.1 µS • Beaker 3: boiling (95 °C) HNO_3 (69 %), 10 min • Quick Dump Rinse: < 0.1 µS • Etching in HF 1% (metal free): 1 min • Quick Dump Rinse: < 0.1 µS • Spin drying
40	**Wet oxidation of silicon** @900 °C *(#film115)*	NL-CLR- Furnace B2 Program WET900 - parameters: ★ Temp.: 900 °C ★ Gas: H_2O + N_2 (Bubbler) ★ N_2 flow: 2 liter/min ★ Ramp: 10 °C min^{-1} ★ Cooldown: 7.5 °C min^{-1} ★ Refractive index n=1.47

		Oxidation time: long enough to consume all the Poly Silicon
41	**Etching in HF 50%** *(#etch129)*	NL-CLR-WB15 Use dedicated beaker. • Etching process wafers: 10 s. • Quick Dump Rinse: < 0.1 µS
42	**Pre-furnace cleaning** *(#clean1202)*	NL-CR-WB 14 and 15 • Beaker 1: fumic HNO_3 (99 %), 5 min • Beaker 2: fumic HNO_3 (99 %), 5 min • Quick Dump Rinse: < 0.1 µS • Beaker 3: boiling (95 °C) HNO_3 (69 %), 10 min • Quick Dump Rinse: < 0.1 µS • Etching in HF 1% (metal free): 1 min • Quick Dump Rinse: < 0.1 µS • Spin drying
43	**LPCVD of SiRN (200-300 Mpa)** *(#film155)*	NL-CLR-Tempress LPCVD G4 Parameters: ★ Temp.: 850 °C ★ SiH_2Cl_2 flow: 150 sccm ★ NH_3 flow: 50 sccm ★ Pressure: 200 mTorr ★ Refractive index n=2.18 **Thickness:** 120 nm **Deposition time:** 12 min **Dummies:** 1 between every 2 process wafers
44	**Optical inspection of LPCVD layers** *(#metro013)*	NL-CR / Cold Light Source

45	**Ellipsometer measurement** *(#metro017)*	NL-CLR-Woolam M-2000 ellipsometer

Accurate measurements of the hinges thickness on all dummies.

46	**Pre-furnace cleaning** *(#clean1202)*	NL-CR-WB 14 and 15 • Beaker 1: fumic HNO_3 (99 %), 5 min • Beaker 2: fumic HNO_3 (99 %), 5 min • Quick Dump Rinse: < 0.1 µS • Beaker 3: boiling (95 °C) HNO_3 (69 %), 10 min • Quick Dump Rinse: < 0.1 µS • Etching in HF 1% (metal free): 1 min • Quick Dump Rinse: < 0.1 µS • Spin drying

Optional step: wafers can directly go from one tube to the next.

47	**Micro Balance Measurement** *(#metro106)*	NL-CLR-Sartortius Micro Balance Use dummy wafer.
48	**LPCVD of Poly Silicon** *(#film105)*	NL-CLR-LPCVD F2 Program senspoly - parameters: ★ Temp.: 590 °C ★ SiH_4 flow: 50 sccm ★ Pressure: 250 mTorr ★ Deposition rate: ± 3.4 nm/min ★ Stress 30 MPa **Thickness:** ~100 nm **Deposition time:** 30 min **Dummy:** 1
49	**Micro Balance Measurement**	NL-CLR-Sartortius Micro Balance

	(#metro106)	Use dummy wafer.
50	**Wet oxidation of silicon @**800 °C *(#film142)*	NL-CLR- Furnace B2 Program WET900 - parameters: ★ Temp.: 900 °C ★ Gas: $H_2O + N_2$ (Bubbler) ★ N_2 flow: 2 liter/min ★ Ramp: 10 °C min^{-1} ★ Cooldown: 7.5 °C min^{-1} ★ Refractive index n=1.47 **Thickness:** ∼5 nm **Oxidation time:** ∼5 min
	No need to start a program, just load the wafers.	
51	**Lithography AZ 9260** *(#lith193)*	
	Priming HMDS	NL-CR-WB28 Lab-line Duo-vac-oven • Dehydration bake (150 °C, low pressure): 5 min • Vapor prime HMDS at (150 °C: 5 min • Let the wafers cool down to room temperature
	Coating (AZ 9260)	Primus Spinner • Spin program: 18 (10 s @ 300 rpm, 60 s @ 2400 rpm) • Prebake (110 °C): 165 s
	Alignment & Exposure (AZ 9260)	Electronic Vision Group 620 Mask Aligner • Hg-lamp: 12 mW/cm^2 • Exposure time: 3 times 10 s with 10 s delay

		• Mask: **GEOM**
	Development (AZ 9260)	Developer: OPD4262 • Time: 3 min 30 s in beaker 1 • Time: 3 min 30 s in beaker 2 • Quick Dump Rinse: < 0.1 µS • Spin drying
	Inspection by optical microscope	NL-CR / Nikon Microscope Dedicated microscope for lithography inspection
52	**Etching BHF (1:7) SiO_2** *(#etch124)*	NL-CR-WB15 • Use standard solution: 30 s
	The wafers should turn hydrophobic where there is no photoresist.	
		• Quick Dump Rinse: < 0.1 µS
53	**Stripping of Olin resist in HNO_3 (99%)** *(#lith116)*	NL-CLR-WB14 • Beaker 0: HNO_3 (99%) time: > 10 min or 100% removal of PR
		• Quick Dump Rinse: < 0.1 µS
54	**Etching in TMAH 5 wt% Standard** @70 °C *(#etch148)*	NL-CLR-WB10 Use standard solution.
		• Use dummy to determine etch rate. • Etching process wafers (∼ 1 min).
	Tune etching time accordingly to the thickness of Poly Silicon.	
		• Quick Dump Rinse: < 0.1 µS

55	**Etching in HF 50%** *(#etch129)*	NL-CLR-WB15 Use dedicated beaker. • Use dummy to determine etch rate (~ 3.2 nm min^{-1}). • Etching process wafers. Tune etching time accordingly to thickness of thin SiRN layer. Over-etching necessary to remove extra material in corners. • Quick Dump Rinse: < 0.1 µS
56	**Pre-furnace cleaning** *(#clean1202)*	NL-CR-WB 14 and 15 • Beaker 1: fumic HNO_3 (99 %), 5 min • Beaker 2: fumic HNO_3 (99 %), 5 min • Quick Dump Rinse: < 0.1 µS • Beaker 3: boiling (95 °C) HNO_3 (69 %), 10 min • Quick Dump Rinse: < 0.1 µS • Etching in HF 1% (metal free): 1 min • Quick Dump Rinse: < 0.1 µS • Spin drying
57	**Wet oxidation of silicon** @900 °C *(#film115)*	NL-CLR- Furnace B2 Program WET900 - parameters: ★ Temp.: 900 °C ★ Gas: H_2O + N_2 (Bubbler) ★ N_2 flow: 2 liter/min ★ Ramp: 10 °C min^{-1} ★ Cooldown: 7.5 °C min^{-1} ★ Refractive index n=1.47 **Oxidation time:** long enough to consume all the Poly Silicon

58	**Etching in HF 50%** *(#etch129)*	NL-CLR-WB15 Use dedicated beaker. • Etching process wafers: 10 s. • Quick Dump Rinse: < 0.1 µS

A.2.5 Release of the structures

Step	Process	
59	**Pre-furnace cleaning** *(#clean1202)*	NL-CR-WB 14 and 15 • Beaker 1: fumic HNO_3 (99 %), 5 min • Beaker 2: fumic HNO_3 (99 %), 5 min • Quick Dump Rinse: < 0.1 µS • Beaker 3: boiling (95 °C) HNO_3 (69 %), 10 min • Quick Dump Rinse: < 0.1 µS • Etching in HF 1% (metal free): 1 min • Quick Dump Rinse: < 0.1 µS • Spin drying
60	**Lithography AZ 9260** *(#lith193)*	
	Priming HMDS	NL-CR-WB28 Lab-line Duo-vac-oven • Dehydration bake (150 °C, low pressure): 5 min • Vapor prime HMDS at (150 °C: 5 min • Let the wafers cool down to room temperature
	Coating (AZ 9260)	Primus Spinner • Spin program: 18 (10 s @ 300 rpm, 60 s @ 2400 rpm)

		• Prebake (110 °C): 165 s
	Alignment & Exposure **(AZ 9260)**	Electronic Vision Group 620 Mask Aligner • Hg-lamp: 12 mW/cm^2 • Exposure time: 3 times 10 s with 10 s delay • Mask: **GEOM**
	Development **(AZ 9260)**	Developer: OPD4262 • Time: 3 min 30 s in beaker 1 • Time: 3 min 30 s in beaker 2 • Quick Dump Rinse: < 0.1 µS • Spin drying
	Inspection by optical microscope	NL-CR / Nikon Microscope Dedicated microscope for lithography inspection
61	**RIE of silicon semi-isotropic** *(Custom recipe)*	NL-CLR-Adixen AMS 100 SE • Native oxide removal Recipe *"Roberts", (#etch174)* **Etching time:** 10 s • Ignition step Parameters: ★ Temp.: 20 °C ★ SF_6 flow: 200 sscm ★ RF power: 2000 W ★ LF power: 0 W ★ APC position: 80 % **Etching time:** 10 s • Silicon etching

		Parameters: ★ Temp.: 20 °C ★ SF_6 flow: 200 sscm ★ RF power: 2000 W ★ LF power: 0 W ★ APC position: 15 % ★ Substrate height: 200 mm **Etching time:** ~200 min
62	**Stripping of resist in O_2 plasma** *(#lith117)*	NL-CLR- Tepla 300E Parameters: ★ Barrel Etcher (2.45 GHz) ★ Pressure: 1.2 mbar ★ O_2 flow: 200 sccm ★ Power: 500 W **Stripping time:** 2 times 60 min

Bibliography

[1] I. S. company.
Http://www.tanomi.com/limited/html/00048.html - accessed September 2014.

[2] R. Fu, J. Luo, A. Flewitt and W. Milne.
Smart microgrippers for bioMEMS applications.
Elsevier, 2012.

[3] X. Wei, Q. Chen, Y. Liu and L. Peng.
Cutting and sharpening carbon nanotubes using a carbon nanotube 'nanoknife'.
Nanotechnology, 18 (18): 185503, 2007.

[4] M. J. Madou.
Fundamentals of Microfabrication.
CRC Press, New York, 1997.

[5] T. G. Leong, A. M. Zarafshar and D. H. Gracias.
Three-Dimensional Fabrication at Small Size Scales.
Small, 6 (7): 792–806, 2010.

[6] S. A. Wilson, R. P. Jourdain, Q. Zhang, R. A. Dorey, C. R. Bowen, M. Willander, Q. U. Wahab, M. Willander, S. M. Al-hilli, O. Nur, E. Quandt, C. Johansson, E. Pagounis, M. Kohl, J. Matovic, B. Samel, W. van der Wijngaart, E. W. Jager, D. Carlsson, Z. Djinovic, M. Wegener, C. Moldovan, R. Iosub, E. Abad, M. Wendlandt, C. Rusu and K. Persson.
New materials for micro-scale sensors and actuators: An engineering review.
Materials Science and Engineering: R: Reports, 56 (1–6): 1–129, 2007.

[7] V. Saile.
Introduction: LIGA and Its Applications, 1–10.
Wiley-VCH Verlag GmbH & Co. KGaA, 2009.

[8] A. M. Greiner, M. Jäckel, A. C. Scheiwe, D. R. Stamow, T. J. Autenrieth, J. Lahann, C. M. Franz and M. Bastmeyer.
Multifunctional polymer scaffolds with adjustable pore size andchemoattractant gradients for studying cell matrix invasion.
Biomaterials, 35 (2): 611 – 619, 2014.

[9] S. Hengsbach and A. D. Lantada.
Direct laser writing of auxetic structures: present capabilities and challenges.
Smart Materials and Structures, 23 (8): 085033, 2014.

[10] K. Sun, T.-S. Wei, B. Y. Ahn, J. Y. Seo, S. J. Dillon and J. A. Lewis.
3D Printing of Interdigitated Li-Ion Microbattery Architectures.
Advanced Materials, 25 (33): 4539–4543, 2013.

[11] L. E. Bertassoni, M. Cecconi, V. Manoharan, M. Nikkhah, J. Hjortnaes, A. L. Cristino, G. Barabaschi, D. Demarchi, M. R. Dokmeci, Y. Yang and A. Khademhosseini.
Hydrogel bioprinted microchannel networks for vascularization of tissue engineering constructs.
Lab on a Chip, 14: 2202–2211, 2014.

[12] C. Shin.
State-of-the-art silicon device miniaturization technology and its challenges.
IEICE Electronics Express, 11 (10), 2014.

[13] J. ya Igaki, K. Kanda, Y. Haruyama, M. Ishida, Y. Ochiai, J. ichi Fujita, T. Kaito and S. Matsui.
Comparison of FIB-CVD and EB-CVD growth characteristics.
Microelectronic Engineering, 83 (4-9): 1225 – 1228, 2006.

[14] H. Yu, B. Li and X. Zhang.
Flexible fabrication of three-dimensional multi-layered microstructures using a scanning laser system.
Sensors and Actuators A: Physical, 125 (2): 553 – 564, 2006.

[15] K. Stebe, E. Lewandowski and M. Ghosh.
Oriented assembly of metamaterials.
Science, 325 (5937): 159–160, 2009.

[16] H. Gradis¡ar and R. Jerala.
Self-assembled bionanostructures: Proteins following the lead of DNA nanostructures.
Journal of Nanobiotechnology, 12 (1), 2014.

[17] K. F. Harsh, V. M. Bright and Y. Lee.
Solder self-assembly for three-dimensional microelectromechanical systems.
Sensors and Actuators A: Physical, 77 (3): 237–244, 1999.

[18] M.-F. Wang, T. Maleki and B. Ziaie.
A self-assembled 3D microelectrode array.
Journal of Micromechanics and Microengineering, 20 (3): 035013, 2010.

[19] J. Luo, R. Huang, J. He, Y. Fu, A. Flewitt, S. Spearing, N. Fleck and W. Milne.
Modelling and fabrication of low operation temperature microcages with a polymer/metal/DLC trilayer structure.
Sensors and Actuators A: Physical, 132 (1): 346–353, 2006.

[20] A. Azam, K. Laflin, M. Jamal, R. Fernandes and D. Gracias.
Self-folding micropatterned polymeric containers.
Biomedical Microdevices, 13: 51–58, 2011.

[21] C. L. Randall, E. Gultepe and D. H. Gracias.
Self-folding devices and materials for biomedical applications.
Trends in Biotechnology, 30 (3): 138–146, 2011.

[22] V. B. Shenoy and D. H. Gracias.
Self-folding thin-film materials: From nanopolyhedra to graphene origami.
MRS Bulletin, 37: 847–854, 2012.

[23] L. Ionov.
Bioinspired Microorigami by Self-Folding Polymer Films.
Macromolecular Chemistry and Physics, 214 (11): 1178–1183, 2013.

[24] C. Py, P. Reverdy, L. Doppler, J. Bico, B. Roman and C. N. Baroud.
Capillary origami: Spontaneous wrapping of a droplet with an elastic sheet.
Physics Review Letters, 98 (15): 156103, 2007.

[25] P. Green, R. Syms and E. Yeatman.
Demonstration of three-dimensional microstructure self-assembly.
Microelectromechanical Systems, Journal of, 4 (4): 170–176, 1995.

[26] D. Gracias, V. Kavthekar, J. Love, K. Paul and G. Whitesides.
Fabrication of Micrometer-Scale, Patterned Polyhedra by Self-Assembly.
Advanced Materials, 14 (3): 235–238, 2002.

[27] J.-H. Cho, M. D. Keung, N. Verellen, L. Lagae, V. V. Moshchalkov, P. Van Dorpe and D. H. Gracias.
Nanoscale Origami for 3D Optics.
Small, 7 (14): 1943–1948, 2011.

[28] E. A. Peraza-Hernandez, D. J. Hartl, R. J. M. Jr and D. C. Lagoudas.
Origami-inspired active structures: a synthesis and review.
Smart Materials and Structures, 23 (9): 094001, 2014.

[29] S. A. Zirbel, R. J. Lang, M. W. Thomson, D. A. Sigel, P. E. Walkemeyer, B. P. Trease and L. L. Magleby, Spencer P. AU Howell.
Accommodating Thickness in Origami-Based Deployable Arrays.
Journal of Mechanical Design, 135 (11): 111005, 2013.

[30] S. Felton, M. Tolley, E. Demaine, D. Rus and R. Wood.
A method for building self-folding machines.
Science, 345 (6197): 644–646, 2014.

[31] S. M. Felton, M. T. Tolley, B. Shin, C. D. Onal, E. D. Demaine, D. Rus and R. J. Wood.
Self-folding with shape memory composites.
Soft Matter, 9: 7688–7694, 2013.

[32] R. Gagler, A. Bugacov, B. E. Koel and P. M. Will.
Voxels: volume-enclosing microstructures.
Journal of Micromechanics and Microengineering, 18 (5): 055025, 2008.

[33] R. Syms and E. Yeatman.
Self-assembly of three-dimensional microstructures using rotation by surface tension forces.
Electronics Letters, 29 (8): 662–664, 1993.

[34] R. Syms.
Surface tension powered self-assembly of 3-D micro-optomechanical structures.
Microelectromechanical Systems, Journal of, 8 (4): 448–455, 1999.

[35] R. Syms.
Self-assembled 3-D silicon microscanners with self-assembled electrostatic drives.
Photonics Technology Letters, IEEE, 12 (11): 1519–1521, 2000.

[36] R. J. Linderman, P. E. Kladitis and V. M. Bright.
Development of the micro rotary fan.
Sensors and Actuators A: Physical, 95 (2-3): 135–142, 2002.

[37] Y. Hong and R. Syms.
Stability of surface tension self-assembled 3D MOEMS.
Sensors and Actuators A: Physical, 127 (2): 381–391, 2006.

[38] T. G. Leong, P. A. Lester, T. L. Koh, E. K. Call and D. H. Gracias.
Surface Tension-Driven Self-Folding Polyhedra.
Langmuir, 23 (17): 8747–8751, 2007.

[39] J. H. Cho and D. H. Gracias.
Self-Assembly of lithographically patterned nanoparticles.
Nano Letters, 9 (12): 4049–4052, 2009.

[40] R. Syms.
Equilibrium of hinged and hingeless structures rotated using surface tension forces.
Microelectromechanical Systems, Journal of, 4 (4): 177–184, 1995.

[41] R. Syms, E. M. Yeatman, V. M. Bright and G. M. Whitesides.
Surface tension-powered self-assembly of microstructures - The state-of-the-art.
Microelectromechanical Systems, Journal of, 12 (4): 387–417, 2003.

[42] W. J. Arora, A. J. Nichol, H. I. Smith and G. Barbastathis.
Membrane folding to achieve three-dimensional nanostructures: Nanopatterned silicon nitride folded with stressed chromium hinges.
Applied Physics Letters, 88 (5): 1–3, 2006.

[43] P. Tyagi, N. Bassik, T. Leong, J.-H. Cho, B. Benson and D. Gracias.
Self-Assembly Based on Chromium/Copper Bilayers.
Microelectromechanical Systems, Journal of, 18 (4): 784–791, 2009.

[44] J. Chen, Z. Fan, J. Zou, J. Engel and C. Liu.
Two-dimensional micromachined flow sensor array for fluid mechanics studies.
Journal of Aerospace Engineering, 16 (2): 85–97, 2003.

[45] A. J. Nichol, P. S. Stellman, W. J. Arora and G. Barbastathis.
Two-step magnetic self-alignment of folded membranes for 3D nanomanufacturing.
Microelectronic Engineering, 84 (5-8): 1168–1171, 2007.

[46] B. Roman and J. Bico.
Elasto-capillarity: deforming an elastic structure with a liquid droplet.
Journal of Physics: Condensed Matter, 22 (49): 493101, 2010.

[47] J.-L. Liu and X.-Q. Feng.
On elastocapillarity: A review.
Acta Mechanica Sinica, 28: 928–940, 2012.

[48] C. Py, P. Reverdy, L. Doppler, J. Bico, B. Roman and C. N. Baroud.
Capillarity induced folding of elastic sheets.
The European Physical Journal - Special Topics, 166: 67–71, 2009.

[49] X. Guo, H. Li, B. Y. Ahn, E. B. Duoss, K. J. Hsia, J. A. Lewis and R. G. Nuzzo.
Two- and three-dimensional folding of thin film single-crystalline silicon for photovoltaic power applications.
Proceedings of the National Academy of Sciences, 106 (48): 20149–20154, 2009.

[50] H. Li, X. Guo, R. G. Nuzzo and K. J. Hsia.
Capillary induced self-assembly of thin foils into 3D structures.
Journal of the Mechanics and Physics of Solids, 58 (12): 2033–2042, 2010.

[51] A. Antkowiak, B. Audoly, C. Josserand, S. Neukirch and M. Rivetti.
Instant fabrication and selection of folded structures using drop impact.
Proceedings of the National Academy of Sciences, 108 (26): 10400–10404, 2011.

[52] N. R. Geraldi, F. F. Ouali, R. H. Morris, G. McHale and M. I. Newton.
Capillary origami and superhydrophobic membrane surfaces.
Applied Physics Letters, 102 (21): 214104, 2013.

[53] J. W. van Honschoten, T. Berenschot, J. W. Ondarçuhu, R. G. P. Sanders, J. Sundaram, M. Elwenspoek and N. R. Tas.
Elastocapillary fabrication of three-dimensional microstructures.
Applied Physics Letters, 97: 0141031–0141033, 2010.

[54] J. van Honschoten, A. Legrain, J. Berenschot, L. Abelmann and N. Tas.
Micro-assembly of three dimensional tetrahedra by capillary forces.
In: *Micro Electro Mechanical Systems (MEMS), 2011 IEEE 24th International Conference on*, 288–291. 2011.

[55] M. Pineirua, J. Bico and B. Roman.
Capillary origami controlled by an electric field.
Soft Matter, 6: 4491–4496, 2010.

[56] Z. Wang, F.-C. Wang and Y.-P. Zhao.
Tap dance of a water droplet.
Royal Society of London Proceedings Series A, 468: 2485–2495, 2012.

[57] L. D. Landau, A. M. Kosevich and E. M. Lifshitz.
Theory of Elasticity.
Butterworth-Heinemann, 1986.

[58] B. Bhushan.
Handbook of Nanotechnology, 3rd ed.
Springer, 2010.

[59] Lobontiu.
Dynamics of Microelectromechanical Systems.
Springer, 2010.

[60] H. Cho, H.-Y. Kim, J. Y. Kang and T. S. Kim.
How the capillary burst microvalve works.
Journal of Colloid and Interface Science, 306 (2): 379–385, 2007.

[61] J. M. Chen, C.-Y. Chen and C.-H. Liu.
Pressure Barrier in an Axisymmetric Capillary Microchannel with Sudden Expansion.
Japanese Journal of Applied Physics, 47 (3): 1683–1689, 2008.

[62] M. Boncheva, D. Bruzewicz and G. Whitesides.
Millimeter-scale self-assembly and its applications.
Pure and Applied Chemistry, 75 (5): 621–630, 2003.

[63] J.-R. Park, D. Choi, D. Gracias, T. Leong, N. Presser, G. Stupian, M. Leung and Y. Kim.
Fabrication and characterization of RF nanoantenna on a nanoliter-scale 3D microcontainer.
Nanotechnology, 22 (45), 2011.

[64] A. Legrain, T. G. Janson, J. W. Berenschot, L. Abelmann and N. R. Tas.
Controllable elastocapillary folding of three-dimensional micro-objects by through-wafer filling.
Journal of Applied Physics, 115 (21): 214905, 2014.

[65] C.-W. Chang and W. Hsu.
Three-dimensional micro assembly of a hinged nickel micro device by magnetic lifting and micro resistance welding.
Journal of Micromechanics and Microengineering, 19 (10), 2009.

[66] F. Iker, N. André, T. Pardoen and J.-P. Raskin.
Three-dimensional self-assembled sensors in thin-film SOI technology.
Microelectromechanical Systems, Journal of, 15 (6): 1687–1697, 2006.

[67] N. André, B. Rue, G. Scheen, D. Flandre, L. A. Francis and J.-P. Raskin.
Out-of-plane MEMS-based mechanical airflow sensor co-integrated in {SOI} {CMOS} technology.
Sensors and Actuators A: Physical, 206 (0): 67 – 74, 2014.

[68] G. Stoney.
The tension of metallic films deposited by electrolysis.
Proc. R. Soc. Lond. A, 82 (553): 172–175, 1909.

[69] G. A. Salvatore, N. Münzenrieder, T. Kinkeldei, L. Petti, C. Zysset, I. Strebel, L. Büthe and G. Tröster.

Wafer-scale design of lightweight and transparent electronics that wraps around hairs.
Nature communications, 5, 2014.

[70] K. Fukuda, Y. Takeda, Y. Yoshimura, R. Shiwaku, L. Tran, T. Sekine, M. Mizukami, D. Kumaki and S. Tokito.
Fully-printed high-performance organic thin-film transistors and circuitry on one-micron-thick polymer films.
Nature Communications, 5, 2014.

[71] M. Kaltenbrunner, M. S. White, E. D. Głowacki, T. Sekitani, T. Someya, N. S. Sariciftci and S. Bauer.
Ultrathin and lightweight organic solar cells with high flexibility.
Nature communications, 3: 770, 2012.

[72] M. S. White, M. Kaltenbrunner, E. D. Głowacki, K. Gutnichenko, G. Kettlgruber, I. Graz, S. Aazou, C. Ulbricht, D. A. Egbe, M. C. Miron *et al.*
Ultrathin, highly flexible and stretchable PLEDs.
Nature Photonics, 7 (10): 811–816, 2013.

[73] D.-H. Kim, J.-H. Ahn, W. M. Choi, H.-S. Kim, T.-H. Kim, J. Song, Y. Y. Huang, Z. Liu, C. Lu and J. A. Rogers.
Stretchable and foldable silicon integrated circuits.
Science, 320 (5875): 507–511, 2008.

[74] T. Sekitani, U. Zschieschang, H. Klauk and T. Someya.
Flexible organic transistors and circuits with extreme bending stability.
Nature materials, 9 (12): 1015–1022, 2010.

[75] M. Avrekh, O. Monteiro and I. Brown.
Electrical resistivity of vacuum-arc-deposited platinum thin films.
Applied Surface Science, 158 (3): 217–222, 2000.

[76] M. Salvadori, A. Vaz, R. Farias and M. Cattani.
Measurement of electrical resistivity of nanostructured platinum thin films and quantum mechanical estimates.
Journal of Metastable and Nanocrystalline Materials, 20-21: 775–780, 2004.

[77] S. Kumar, M. Alam, Z. Connell and M. Haque.
Electromigration stress induced deformation mechanisms in free-standing platinum thin films.
Scripta Materialia, 65 (4): 277–280, 2011.

[78] M. Rudneva, B. Gao, F. Prins, Q. Xu, H. Van Der Zant and H. Zandbergen.
In situ transmission electron microscopy imaging of electromigration in platinum nanowires.
Microscopy and Microanalysis, 19 (SUPPL. 5): 43–48, 2013.

[79] R. Tiggelaar, R. Sanders, A. Groenland and J. Gardeniers.
Stability of thin platinum films implemented in high-temperature microdevices.
Sensors and Actuators, *A: Physical*, 152 (1): 39–47, 2009.

[80] S. Firebaugh, K. Jensen and M. Schmidt.
Investigation of high-temperature degradation of platinum thin films with an in situ resistance measurement apparatus.
Microelectromechanical Systems, Journal of, 7 (1): 128–135, 1998.

[81] C. Alépée.
Technologies for High-temperature Silicon Microreactors.
Series in microsystems. Hartung-Gorre, 2001.

[82] G. M. Whitesides and B. Grzybowski.
Self-assembly at all scales.
Science, 295 (5564): 2418–2421, 2002.

[83] K. Ariga, J. P. Hill, M. V. Lee, A. Vinu, R. Charvet and S. Acharya.
Challenges and breakthroughs in recent research on self-assembly.
Science and Technology of Advanced Materials, 9 (1): 014109, 2008.

[84] M. Mastrangeli, S. Abbasi, C. Varel, C. van Hoof, J. P. Celis and K. F. Böhringer.
Self-assembly from milli- to nanoscales: methods and applications.
Journal of Micromechanics and Microengineering, 19: 1–37, 2009.

[85] S. T. Brittain, O. J. A. Schneller, H. Wu, S. Whitesides and G. M. Whitesides.
Microorigami: Fabrication of small, three-dimensional, metallic structures.
The Journal of Physical Chemistry B, 105 (2): 347–350, 2001.

[86] V. Kaajakari and A. Lal.
Thermokinetic actuation for batch assembly of microscale hinged structures.
Microelectromechanical Systems, Journal of, 12 (4): 425–432, 2003.

[87] Y.-W. Lu and C.-J. Kim.
Microhand for biological applications.
Applied Physics Letters, 89 (16): 164101, 2006.

[88] J. Guan, H. He, D. J. Hansford and L. J. Lee.
Self-Folding of Three-Dimensional Hydrogel Microstructures.
The Journal of Physical Chemistry B, 109 (49): 23134–23137, 2005.

[89] S. J. Kim, H. I. Kim, S. J. Park, I. Y. Kim, S. H. Lee, T. S. Lee and S. I. Kim.
Behavior in electric fields of smart hydrogels with potential application as bio-inspired actuators.
Smart Materials and Structures, 14 (4): 511, 2005.

[90] G. Stoychev, N. Puretskiy and L. Ionov.
Self-folding all-polymer thermoresponsive microcapsules.
Soft Matter, 7 (7): 3277–3279, 2011.

[91] L. Ionov.
Soft microorigami: self-folding polymer films.
Soft Matter, 7: 6786–6791, 2011.

[92] Y. Liu, J. K. Boyles, J. Genzer and M. D. Dickey.
Self-folding of polymer sheets using local light absorption.
Soft Matter, 8: 1764–1769, 2012.

[93] O. G. Schmidt and K. Eberl.
Nanotechnology: Thin solid films roll up into nanotubes.
Nature, 410 (6825): 168–168, 2001.

[94] C. Chua, D. Fork, K. Van Schuylenbergh and J.-P. Lu.
Out-of-plane high-Q inductors on low-resistance silicon.
Microelectromechanical Systems, Journal of, 12 (6): 989–995, 2003.

[95] T. G. Leong, B. R. Benson, E. K. Call and D. H. Gracias.
Thin Film Stress Driven Self-Folding of Microstructured Containers.
Small, 4 (10): 1605–1609, 2008.

[96] J.-H. Cho, T. James and D. H. Gracias.
Curving Nanostructures Using Extrinsic Stress.
Advanced Materials, 22 (21): 2320–2324, 2010.

[97] J. Judy and R. Muller.
Magnetically actuated, addressable microstructures.
Microelectromechanical Systems, Journal of, 6 (3): 249–256, 1997.

[98] M. Boncheva, S. A. Andreev, L. Mahadevan, A. Winkleman, D. R. Reichman, M. G. Prentiss, S. Whitesides and G. M. Whitesides.
Magnetic self-assembly of three-dimensional surfaces from planar sheets.
Proceedings of the National Academy of Sciences, 102 (11): 3924–3929, 2005.

[99] E. Iwase and I. Shimoyama.
A design method for out-of-plane structures by multi-step magnetic self-assembly.
Sensors and Actuators A: Physical, 127 (2): 310–315, 2006.

[100] A. J. Nichol, W. J. Arora and G. Barbastathis.
Thin membrane self-alignment using nanomagnets for three-dimensional nanomanufacturing.
Journal of Vacuum Science & Technology B, 24 (6): 3128–3132, 2006.

[101] D. J. Filipiak, A. Azam, T. G. Leong and D. H. Gracias.
Hierarchical self-assembly of complex polyhedral microcontainers.
Journal of Micromechanics and Microengineering, 19 (7): 075012, 2009.

[102] E. Sarajlic, J. W. Berenschot, G. J. M. Krijnen and M. C. Elwenspoek.
Fabrication of 3D nanowire frames by conventional micromachining technology.
In: *13th Int. Conf. on Solid-State Sensors, Actuators and Microsystems, Digest of Technical Papers (TRANSDUCERS '05)*, volume 1, 27–30. Seoul, South Korea, 2005.

[103] E. Berenschot, N. R. Tas, H. V. Jansen and M. Elwenspoek.
3D-Nanomachining using Corner Lithography.
In: *3rd IEEE Int. Conf. on Nano/Micro Engineered and Molecular Systems (NEMS 2008)*, 729–732. Sanya, 2008.

[104] X. Yu, H. Zhang, J. K. Oliverio and P. V. Braun.
Template-Assisted Three-Dimensional Nanolithography via Geometrically Irreversible Processing.
Nano Letters, 9 (12): 4424–4427, 2009.

[105] E. J. W. Berenschot, N. Burouni, B. Schurink, J. W. van Honschoten, R. G. P. Sanders, R. Truckenmuller, H. V. Jansen, M. C. Elwenspoek, A. A. van Apeldoorn and N. R. Tas.
3D Nanofabrication of Fluidic Components by Corner Lithography.
Small, 8 (24): 3823–3831, 2012.

[106] N. Burouni, E. Berenschot, M. Elwenspoek, E. Sarajlic, P. Leussink, H. Jansen and N. Tas.
Wafer-scale fabrication of nanoapertures using corner lithography.
Nanotechnology, 24 (28): 285303, 2013.

[107] E. J. W. Berenschot, H. V. Jansen and N. R. Tas.
Fabrication of 3D fractal structures using nanoscale anisotropic etching of single crystalline silicon.
Journal of Micromechanics and Microengineering, 23 (5): 055024, 2013.

[108] G. Sinclair and M. Kondo.
On the stress concentration at sharp re-entrant corners in plates.
International Journal of Mechanical Sciences, 26 (9-10): 477 – 487, 1984.

[109] W. Pilkey and D. Pilkey.
Peterson's Stress Concentration Factors.
Wiley, 2008.

[110] G. Kim, A. Kovalgin, J. Holleman and J. Brugger.
Replication molds having nanometer-scale shape control fabricated by means of oxidation and etching.
Journal of Nanoscience and Nanotechnology, 2 (1): 55–9, 2002.

[111] T. Shankoff, T. Sheng, S. Haszko, R. Marcus and T. Smith.
Bird's beak configuration and elimination of gate oxide thinning produced during selective oxidation.
Journal of the Electrochemical Society, 127 (1): 216–222, 1980.

[112] H. V. Jansen, M. J. De Boer, S. Unnikrishnan, M. C. Louwerse and M. C. Elwenspoek.
Black silicon method X: a review on high speed and selective plasma etching of silicon with profile control: an in-depth comparison between Bosch and cryostat DRIE processes as a roadmap to next generation equipment.
Journal of Micromechanics and Microengineering, 19 (3): 033001, 2009.

[113] D. L. Blair and A. Kudrolli.
Geometry of Crumpled Paper.
Physics Review Letters, 94: 166107, 2005.

[114] H. Porada and E. Bouougri.
Wrinkle structures-a critical review.
Earth-Science Reviews, 81 (3-4): 199–215, 2007.

[115] S. Deboeuf, E. Katzav, A. Boudaoud, D. Bonn and M. Adda-Bedia.
Comparative Study of Crumpling and Folding of Thin Sheets.
Physical Review Lett., 110: 104301, 2013.

[116] E. Bayart, A. Boudaoud and M. Adda-Bedia.
Tuning the ordered states of folded rods by isotropic confinement.
Physical Review E, 89: 012407, 2014.

[117] J. A. Rogers, T. Someya and Y. Huang.
Materials and Mechanics for Stretchable Electronics.
Science, 327 (5973): 1603–1607, 2010.

[118] Q. Li and X. M. Tao.
Three-dimensionally deformable, highly stretchable, permeable, durable and washable fabric circuit boards.
Proceedings of the Royal Society A: Mathematical, Physical and Engineering Science, 470 (2171), 2014.

[119] S. Dmitriev, J. Baimova, A. Savin and Y. Kivshar.
Ultimate strength, ripples, sound velocities, and density of phonon states of strained graphene.
Computational Materials Science, 53 (1): 194–203, 2012.

[120] E. Korznikova and S. Dmitriev.
Moving wrinklon in graphene nanoribbons.
Journal of Physics D: Applied Physics, 47 (34), 2014.

[121] A. E. Green.
The Elastic Stability of a Thin Twisted Strip. II.
Proceedings of the Royal Society of London. Series A, Mathematical and Physical Sciences, 161 (905): 197–220, 1937.

[122] D. J. Crispino and R. C. Benson.
Stability of twisted orthotropic plates.
International Journal of Mechanical Sciences, 28 (6): 371 – 379, 1986.

[123] C. Coman and A. Bassom.
An asymptotic description of the elastic instability of twisted thin elastic plates.
Acta Mechanica, 200 (1-2): 59–68, 2008.

[124] E. M. Mockensturm.
The Elastic Stability of Twisted Plates.
Journal of Applied Mechanics, 68 (4): 561–567, 2000.

[125] S. Cranford and M. J. Buehler.
Twisted and coiled ultralong multilayer graphene ribbons.
Modelling and Simulation in Materials Science and Engineering, 19 (5): 054003, 2011.

[126] O. O. Kit, T. Tallinen, L. Mahadevan, J. Timonen and P. Koskinen.
Twisting graphene nanoribbons into carbon nanotubes.
Physical Review B, 85: 085428, 2012.

[127] S. Armon, H. Aharoni, M. Moshe and E. Sharon.
Shape selection in chiral ribbons: from seed pods to supramolecular assemblies.
Soft Matter, 10: 2733–2740, 2014.

[128] A. P. Korte, E. L. Starostin and G. H. M. van der Heijden.
Triangular buckling patterns of twisted inextensible strips.
Proceedings of the Royal Society A: Mathematical, Physical and Engineering Science, 467 (2125): 285–303, 2011.

[129] J. Chopin and A. Kudrolli.
Helicoids, Wrinkles, and Loops in Twisted Ribbons.
Physical Review Letters, 111: 174302, 2013.

[130] J. Chopin, V. Démery and B. Davidovitch.
Roadmap to the morphological instabilities of a stretched twisted ribbon.
ArXiv e-prints, 2014.

[131] R. L. Alley, G. J. Cuan, R. Howe and K. Komvopoulos.
The effect of release-etch processing on surface microstructure stiction.
In: *Solid-State Sensor and Actuator Workshop, 1992. 5th Technical Digest., IEEE*, 202–207. 1992.

[132] C. Mastrangelo and C. Hsu.
Mechanical stability and adhesion of microstructures under capillary forces. I. Basic theory.
Microelectromechanical Systems, Journal of, 2 (1): 33–43, 1993.

[133] C. Mastrangelo and C. Hsu.
Mechanical stability and adhesion of microstructures under capillary forces. II. Experiments.
Microelectromechanical Systems, Journal of, 2 (1): 44–55, 1993.

Publications

Journal articles

[1] A. Legrain, T. G. Janson, J. W. Berenschot, L. Abelmann and N. R. Tas.
Controllable elastocapillary folding of three-dimensional micro-objects by through-wafer filling.
Journal of Applied Physics, 115 (21): 214905, 2014.

Submitted

[1] A. Legrain, J. W. Berenschot, N. R. Tas and L. Abelmann.
Capillary origami of micro-machined micro-objects: bi-layer conductive hinges.
ArXiv e-prints, 2014.

[2] A. Legrain, J. W. Berenschot, N. R. Tas and L. Abelmann.
Elastocapillary folding using stop-programmable hinges fabricated by 3D micro-machining.
ArXiv e-prints, 2014.

Conference contributions

[1] J. W. van Honschoten, A. Legrain, J. W. Berenschot, L. Abelmann and N. R. Tas.
Micro-assembly of three dimensional tetrahedra by capillary forces.
In *24th IEEE International Conference on Micro Electro Mechanical Systems, MEMS 2011, Cancun, Mexico*, pages 288–291, USA, January 2011. IEEE Robotics and Automation Society.

[2] A. Legrain, J. W. Berenschot, R. G. P. Sanders, K. Ma, N. R. Tas and L. Abelmann.
Elastocapillary folding of three dimensional micro-structures using water pumped through the wafer via a silicon nitride tube.
In *Proceedings of the 22nd Micromechanics and Microsystems Technology Europe Workshop, Tonsberg, Norway*, pages 250–253, Norway, 2011. Department of micro and nano systems technology, Vestfold University College.

[3] A. Legrain, T. G. Janson, J. W. Berenschot, G. J. M. Krijnen L. Abelmann, and N. R. Tas.
Controllable elastocapillary folding of silicon nitride 3D structures by through-wafer filling.
In *8th Annual IEEE International Conference on Nano/Micro Engineered and Molecular Systems, IEEE NEMS 2013, Suzhou, China*, number CFP13NME-ART, pages 538–541. IEEE, 2013.

[4] A. Legrain, O. Pjetri, J. W. Berenschot, G. J. M. Krijnen and L. Abelmann.

Design and preliminary fabrication of an elastocapillary folded out-of-plane microflown sensor.
In *Proceedings of the 24th Micromechanics and Microsystems Technology Europe Workshop, Espoo, Finland*, Finland, 2013. Aalto University.

Acknowledgments

My time in TST group and the resulting work presented in this thesis would have never been possible without Joost W. van Honschoten. He was the kind guy that took the time to introduce a student from an obscure French university to a field I had barely any knowledge in, and eased my way into Twente talking French to me when my English was as good as it is when going out of University in France - that is, pretty bad. I only knew him during the half year I spent in Enschede for my master thesis, but I can say without a doubt that he was a great man. We miss you.

Miko Elwenspoek was at this time the head of the group, and I would like to thank him for accepting my application as a Master intern. Without your approval my life would have been much different. Later on, funding my PhD years had not been straightforward, and I would like to thank the people that trusted my abilities to successfully complete my thesis and found ways to finance my stay in Holland. Gijs, Remco and Leon, thank you. I would also like to thank the members of my graduation committee - Prof. Jurriaan Schmitz, Prof. Jan C.T. Eijkel, Prof. Fred van Keulen and Dr. José Bico - who kindly accepted to evaluate my thesis. I highly appreciated the help from Chris Sanders who corrected my texts despite how puzzled he must had been with all this scientific jargon.

Of course there is no successful PhD without proper supervising. I enjoyed a lot working with Prof. Leon Abelmann. If there is one surviving tip to give in academic is that having fun is crucial, and that is Leon's leitmotiv. I had my ups and down during these few years but you were always available to cheer me up and make me looking and moving forward. Thank you. Dr. Niels Tas only recently became assistant promotor, but it was a logical consequence of his precious help. I have appreciated the fun and learning discussions we have had, and was glad to contribute to the huge pile of paper sheets on your desk, sometimes by printing and handing you several times the same document. Erwin Berenschot, you are not entitled to be one of my supervisors, but it feels like you would have the rights to be. I cannot thank you enough for your patient help in the cleanroom and always cheerful discussions out of it,

around a beer or not.

Remco Sanders, you also contributed a lot to my work. You were always available to help me with my experiments and to suggest improvements with a smile. I did not always understand the jokes you said in dutch, but I am convinced they were funny. Kees Ma, you helped me out in the cleanroom a countless amount of times and made the waiting time during processing much less boring. Even outside of the nanolab building you were always eager to help. My former car battery remembers. I will also remember the delightful Chinese food I had the privilege to share with your family. In research groups not enough credits go to the secretaries that make the whole thing more or less standing up and moving forward. Susan, you are probably the happiest person I have ever met and you are the best at communicating it. You formed with Karen the best pair of secretaries in science history. Listening to your loud laughs during difficult mornings was priceless. Satie, thank you for your kindness and help with my diploma.

A huge thanks to other people of TST that used to make it such a nice place to work in. In my office, Joel and his cleanest desk was there to remain me that I should clean mine sometimes. Leon W. is still working on self-assembling his macroscopic mock up that I broke. Laurens the equation guy that makes me feel bad about my mathematical skills. Özlem and her feminine presence, unfortunately too rare in TST. Pele and his love of bugs. You were all nice to me, thank you. Hadi, Olti, my smoking buddies, it was a pleasure. Robert, Harmen, Jarno, Jeroen, Rolf, Maarten, Kodai, Narges, it was nice to share the PhD struggles with you. Henri, Gijs, Remco and Miko, I sometimes needed your help and you were always willing to give it to me. Thijs, Martin, Meint and Henk, thanks for your skilled assistance with technical stuff.

I spent quite a long time in the cleanroom and I would like to thank the staff for their help: Marion, Samantha, Gerard, Peter, Rene, Robert, Hans, Eddy, Ton, Mark, Ite-Jan, Rene, Hans, Huib and Chris, I hope I was not too annoying to you.

Thank you also to the people with whom I had fun outside of work who will recognize themselves here. Doing a PhD is hard, and it is necessary to evacuate the pressure one way or another. Thanks to flatmates, basketball teammates, climbing buddies, pub quiz and drinking mates... You will always be welcome wherever I land up next.

Enfin, j'aimerais remercier mes amis et ma famille pour leurs inconditionnels soutiens. Vous êtes nombreux à vous avoir demandé, et à toujours se

demander, ce que je pouvais bien faire pendant tout ce temps passé “en haut”. Malgré cela je pouvais toujours compter sur vous et je savais que rien n’aurait changé au moment de vous revoir. Un grand merci à mes parents bien entendu, qui ont supporté mes humeurs changeantes pendant les quelques mois qu’a demandé l’écriture de cette thèse. Vous êtes des personnes exceptionnelles et je ne peux qu’admirer la manière avec laquelle vous avez vécu et continuez de vivre.